Laboratory Rock Strength Measurements of Saturated Carbonates: Implications for the Grosmont Formation

by

Tyson Richard Epp

A thesis submitted in partial fulfillment of the requirements for the degree of

Master of Science

in

Geophysics

Department of Physics
University of Alberta

Abstract

The Devonian Grosmont formation, located in Alberta, contains vast resources totaling approximately 405 billion barrels of crude bitumen-in-place. The highly viscous bitumen is by definition less than 10° API gravity, remaining immobile at Grosmont formation in-situ temperatures. In the oil and gas industry, rock mechanics knowledge is fundamental to overcoming reservoir development and production problems. This is especially true for unconventional reservoirs, such as the Grosmont formation that employs advanced enhanced oil recovery techniques.

A robust geomechanical model requires the integration of static and dynamic rock strength measurements. This study focuses on laboratory-based strength measurements of carbonate rocks saturated with highly viscous material. An attempt was made at defining Grosmont formation geomechanical properties but, due to core paucity and characteristic fractures, a restricted number of Brazilian tensile strength tests were completed. From these tests, a limited profile of tensile splitting strengths was developed for the Grosmont formation reservoir subunits ranging from 4.3 MPa to 11.4 MPa. Additional core and subsequent testing is essential to meet the ultimate goal of properly defining the Grosmont formation's geomechanical properties.

To further study viscous fluid effects, Indiana limestone saturated with paraffin wax was introduced as a Grosmont formation analogue. Although this comparison is imperfect, the practically solid state of paraffin wax at room temperature mimics bitumen at in-situ temperatures. A comprehensive series of 39 compressive and 20 tensile strength tests were performed on Indiana limestone. The peak strengths of wax-saturated and dry samples, determined through compressive testing, are nearly identical. However, subtle variations in elastic moduli and failure mode exist. Brazilian tensile testing results show systematically increased tensile splitting strengths in wax-saturated samples.

Acknowledgments

Thank you to Dr. Doug Schmitt for his guidance during this work. I have learned so much from him and sincerely appreciate his approachability, sense of humor, and infectious passion for geophysics. Thanks to Randy Kofman, Xiwei Chen, Nam Ong, and Tariq Mohammed for assistance in the laboratory. It was a fun few years being part of the Experimental Geophysics Group, I consider you all friends.

Thank you to Laricina Energy Ltd. and OSUM Oil Sands Corporation for project sponsorship.

To my wife Jarret, your love, support, encouragement, sacrifice, and hard work during this period will forever motivate me; thank you. To my parents, thank you for your unwavering support, always pushing me to do my best, and encouraging academics; looks like it may have worked. Above all, to God be the glory.

Table of Contents

1. Introduction 1
- 1.1 Introduction 1
- 1.2 Thesis Organization 3
- 1.3 Presentations and Publications 5

2. Geology and Sample Characterization 6
- 2.1 Introduction 6
- 2.2 Grosmont Formation 6
- 2.3 Indiana limestone 16
- 2.4 Thin Sections 17
- 2.5 Scanning Electron Microscope (SEM) 18
- 2.6 Helium Pycnometer 18
- 2.7 Mercury Intrusion Porosimetry 20
- 2.8 Summary 21

3. Rock Mechanics Considerations 22
- 3.1 Introduction 22
- 3.2 Stress in the Earth’s Crust 22
- 3.3 Laboratory Strength Tests 25
- 3.4 Rock Deformation and Failure 26
  - 3.4.1 Stress and Strain in Laboratory Tests 27
  - 3.4.2 Role of Confining Pressure 30
  - 3.4.3 Rock Failure in Compression 31
  - 3.4.4 Pore Pressure Effects 34
  - 3.4.5 Tensile Failure 35
- 3.5 Summary 36

4. Laboratory Experiments 37
- 4.1 Compressive Strength Tests 37
  - 4.1.1 Sample Preparation 37
  - 4.1.2 Strain Gauges 42
  - 4.1.3 Experimental Apparatus 46

4.1.4 Procedure 49
4.2 Tensile Strength Tests 50
4.2.1 Sample Preparation 50
4.2.2 Experimental Apparatus 51
4.2.3 Procedure 52
4.3 System Calibration 53
5. Indiana Limestone Geomechanical Testing Results 54
5.1 Introduction 54
5.2 Experimental Description 57
5.2.1 Sample Material 57
5.2.2 Sample Preparation 59
5.2.3 Experimental Procedures 60
5.3 Experimental Results and Discussion 63
5.3.1 Mechanical Data 63
5.3.2 Compressive Strength Data 63
5.3.3 Elastic Properties 71
5.3.4 Microscopic Observations 73
5.3.5 Tensile Strength Data 77
5.4 Conclusions 80
6. Grosmont Formation Brazilian Tensile Strength Results 81
6.1 Introduction 81
6.2 Brazilian Tests 81
6.3 Conclusions 84
7. Conclusion 85
7.1 Conclusion 85
7.2 Future Work 87
References 859
Appendix A 85

List of Tables

Table 1 Grosmont Fm. porosity and saturation........ 15

Table 2 ASTM 4543 sample preparation tolerances........ 37

Table 3 Compressive strength data........ 67

Table 4 Linear regression parameters from strength data........ 69

Table 5 Grosmont formation core sample specifications........ 81

List of Figures

Figure 1.1 Location of the Grosmont formation and other bitumen saturated formations in Alberta 1

Figure 1.2 a) Core photo from well 100-1-27-85-19W4 near the top of the Grosmont D subunit (343.6-346.2m). b) Samples of Indiana limestone prepared for mechanical testing.. 2

Figure 2.1 Grosmont formation bitumen pay thickness outline, modified from Alberta Energy Regulator [2015] 7

Figure 2.2 Stratigraphy of northern Alberta region modified from Buschkuehle et al. [2007] 8

Figure 2.3 Well logs from well 100-1-27-85-19W4 9

Figure 2.4 Core photos of GMC from well 100-1-27-85-19W4 (379.4 - 387.26 m) 12

Figure 2.5 FMI log images through the GMC from well 100-1-27-8519W4 13

Figure 2.6 Core photo of GMD from well 100-1-27-85-19W4 (363.9 - 367.89 m) 14

Figure 2.7 FMI log images through the GMD from well 100-1-27-8519W4 15

Figure 2.8 SEM image of untested Indiana limestone 18

Figure 2.9 Helium pycnometer schematic 19

Figure 3.1 a) Complete stress tensor components acting on an infinitesimal cube of material in the XYZ coordinate system. b) Principal stresses acting on the cube after rotation to coordinate system X'Y'Z'. 23

Figure 3.2 Diagram of faults with principal stress states from Anderson classification. 25

Figure 3.3 Diagrams of laboratory strength tests performed in this study 26

Figure 3.4 a) deformation of ideal material from applied normal stress, b) deformation of ideal material from applied shear stress, and c) deformation of rock sample in UCS testing... 27

Figure 3.5 Axial stress-strain curve typical of data collected in the laboratory during UCS testing........... 29

Figure 3.6 Stress-strain curves for various confining pressures 30

Figure 3.7 a) Stresses developed on a shear failure plane in a core sample under triaxial stress. b) Diagram of Mohr envelope fit to a series of triaxial tests. c) Diagram of the linearized Mohr-Coulomb failure criterion 32

Figure 3.8 Example of ultimate strength data from a series of triaxial tests on dry Indiana limestone 33

Figure 4.1 Top view of one raw block of Indiana Limestone used for rock strength experiments 38

Figure 4.2 Image of the diamond rock saw used to cut Indiana limestone blocks 38

Figure 4.3 Photo of the drill press and example of a thin walled drill bit used to cut core samples 39

Figure 4.4 Photo of the surface grinder used to machine the ends of the cored specimens 40

Figure 4.5 Photo of the apparatus used for determining the flatness of the cylindrical end surfaces...... 41

Figure 4.6 Schematic of strain gauge. 43

Figure 4.7 Diagram of a Wheatstone bridge circuit........ 44

Figure 4.8 Photo of prepared samples with strain gauges attached........ 46

Figure 4.9 Photo of uniaxial compressive strength experimental set-up........ 47

Figure 4.10 A) Photo of triaxial compressive strength experimental set-up. B) Schematic of Hoek cell... 47

Figure 4.11 Photo of prepared Grosmont formation (sample A1) Brazilian disk test specimen. A) Pre-testing. B) Post-testing........ 51

Figure 4.12 Schematic A) and photo B) of Brazilian tensile strength laboratory testing set-up........ 52

Figure 4.13 Axial stress-strain curve of aluminum sample and fitted data to estimate Young's Modulus. 53

Figure 5.1: Top: A thin section from dry sample with pore space highlight by blue epoxy 58

Figure 5.2 A) Image of triaxial strength test laboratory set-up, the same load frame was used for all experiments. B) Schematic of Hoek Cell........ 61

Figure 5.3 A) Schematic of the stresses acting on a core sample under compression and resulting failure plane. σ_1 and σ_3 indicate the maximum and minimum principal stresses respectively, σ_n is the normal stress to the failure plane, τ is the shear stress, and β is the angle between σ_n and σ_1. B) Schematic of Brazilian tensile strength tests. P_a denotes the applied pressure and the typical failure plane through the sample is drawn........ 63

Figure 5.4 Axial stress vs axial (positive strain) and lateral (negative strain) strain curves for dry samples 64

Figure 5.5 Axial stress vs axial (positive strain) and lateral (negative strain) strain curves for wax-saturated samples........ 65

Figure 5.6 Photos of samples after triaxial testing........ 66

Figure 5.7 Peak strength of dry and wax-saturated Indiana Limestone samples as a function of confining pressure........ 68

Figure 5.8 Upper: Mohr-Coulomb failure criterion for all measured dry samples. Lower: Mohr-Coulomb failure criterion for all measured wax-saturated samples........ 70

Figure 5.9 Example of Young's Modulus and Poisson's Ratio determination 72

Figure 5.10 Elastic properties of tested samples........ 73

Figure 5.11 Thin sections prepared from deformed samples 76

Figure 5.12 Magnified thin sections 77

Figure 5.13 Plot of the splitting tensile strength for each sample 78

Figure 5.14 Stress-strain curves for 4 Brazilian tensile tests 79

Figure 6.1 Sample photos post-BTS testing........ 82

Figure 6.2 Brazilian tensile splitting strength of Grosmont formation samples........ 83

1. Introduction

1.1 Introduction

This thesis is motivated by an interest in the geomechanical properties of the Grosmont formation and is part of a larger effort to characterize its rock properties. The Grosmont formation is a large bitumen bearing carbonate reservoir located in Alberta approximately 300 km north of Edmonton (Fig. 1.1). The Alberta Energy Regulator (AER) estimates approximately 405 billion barrels of crude bitumen-in-place, accounting for 22% of Alberta's crude bitumen.

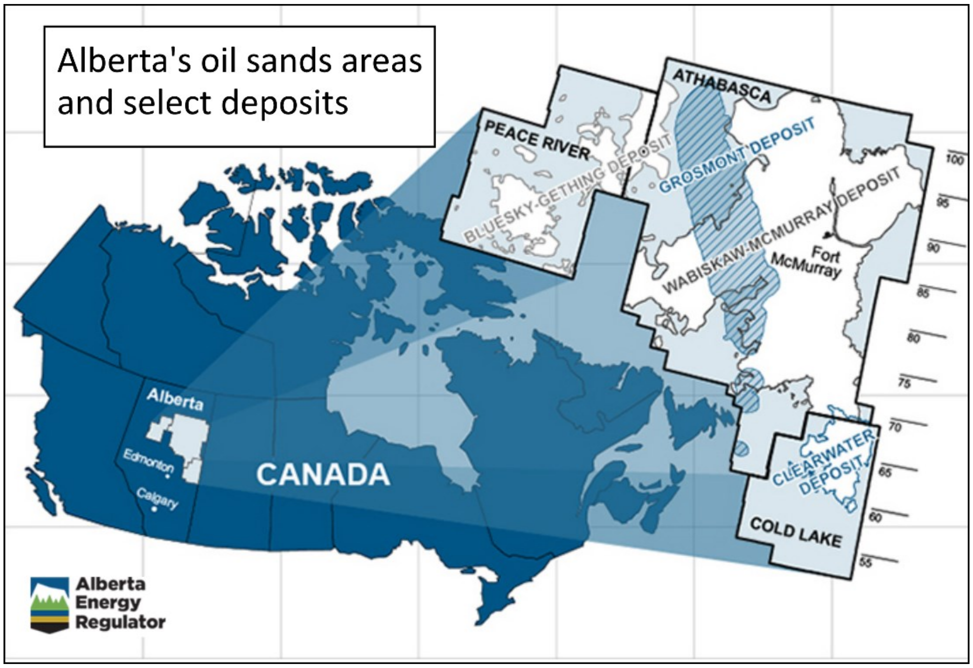

Figure 1.1 Location of the Grosmont formation and other bitumen saturated formations in Alberta. Figure is modified from the AER's ST98: Alberta's Energy Reserves and Supply/Demand Outlook. Reproduced with permission through the AER's copyright and disclaimer policy on non-commercial and educational reproduction (*http://aer.ca/copyright-disclaimer*).

The Grosmont formation is highly fractured and karsted, leading to an eminently porous but complicated heterogeneous reservoir. The bitumen is highly viscous with reported API gravity values ranging from 7-9°, rendering it practically solid at in situ temperatures of ~12°C [*MacNeil*, 2015]. The quasi-solid nature of the bitumen requires the application of thermal recovery techniques, like those commercially proven in the neighboring, and in some places overlying Athabasca oil sands. There are many complexities in enhanced oil recovery using thermal techniques as external pressure, heat and chemical processes are introduced into the reservoir via steam [*Butler*, 1994]. Thermal recovery methods have been applied to the Grosmont formation in two major time periods: 1) through the 1970's and 1980's and 2) in the late 2000's through 2015 [*Mohebati et al.*, 2014]. The latter period attempted to take advantage of technological innovations, such as horizontal drilling, improved seismic data quality, and learnings from successes in the Athabasca oil sands [*Mohebati et al.*, 2014; *Yang et al.*, 2014; *Putnam et al.*, 2016]. Given the vast size of the resource, it is assumed there will be future production endeavors in the Grosmont formation.

The bitumen-in-place recovery efficiency is dependent on proper reservoir characterization. Part of characterizing a reservoir is the determination of its mechanical properties. It is essential to have rock strength knowledge for engineering and production purposes. The risk of wellbore failure and the worst case of a steam release [*Hein and Fairgrieve*, 2013] or bitumen emulsion flow to surface event are mitigated with knowledge of geomechanical properties [*Schultz*, 2016]. On the other hand, injection of steam at pressures sufficient to fracture the reservoir result in significant increases in porosity and permeability, improving recovery factors [*Chalaturnyk and Li*, 2004; *Collins*, 2005; *Yuan et al.*, 2011].

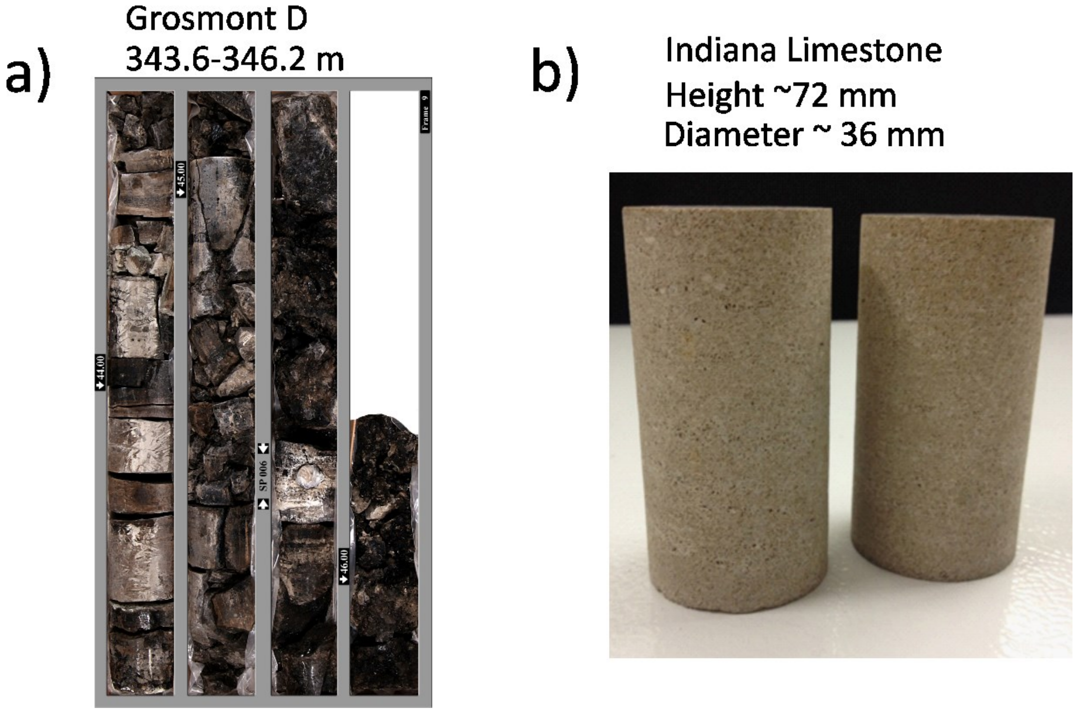

Figure 1.2 a) Core photo from well 100-1-27-85-19W4 near the top of the Grosmont D subunit (343.6-346.2m). b) Samples of Indiana limestone prepared for mechanical testing.

The fractured and heterogeneous constitution of the Grosmont formation (Fig. 1.2a) make conducting a meaningful geomechancial testing project challenging at best. Standard size compressive strength testing samples are difficult to obtain because of fractures, especially in zones of greatest bitumen saturation. Some of the cores are literally held together by bitumen, and crumble upon extraction. Often, the most competent cores are tested, and this can provide an upper bound on formation strength; but the failure strength remains untested in weaker zones of high porosity and saturation. Cores from multiple wells are needed to properly test the strength of the many facies contained within the Grosmont formation.

Another problem with geomechanical testing is its destructive nature. When performed in conjuction with other rock physics tests, mechanical testing is left for last. The rock physics tests, such as ultrasonic wave propagation [*Ong et al.*, 2016; *Rabbani et al.*, 2017], require machining of the core sample to dimensions such that a strong signal is resolved. This does not always align with the requirements of geomechanical testing specifications.

For these reasons, only tensile strength testing of the Grosmont formation was completed in this study. Although obtaining compressive strength measurements is ideal, the tensile strength of the Grosmont formation is relevant. Morin [2017] found drilling induced tensile fractures in more than 90% of image logs analyzed through the Grosmont formation. These observed fractures are related to rock failure under tension as in situ stresses are concentrated around the borehole wall. As such, having knowledge of the tensile strength of the intact Grosmont dolomites assists in constraint of stress magnitudes as deduced from borehole drilling induced tensile fractures.

To understand broader geomechanical implications of a viscoelastic material filling the pore space of a carbonate rock, experiments on Indiana limestone (Fig 1.2b) saturated with paraffin wax were conducted in this study. Indiana limestone and paraffin wax are imperfect substitutes for the Grosmont formation and bitumen, but shared similarities exist. Both are porous carbonate rocks, and like in situ bitumen, paraffin wax is solid at room temperature. A series of compressional (unconfined compressive strength (UCS) and triaxial) and tensile (Brazilian tensile strength) strength measurements were performed on both dry and wax-saturated Indiana limestone. The investigation of failure processes in these rocks can provide analogous insights into the mechanical failure of the Grosmont formation and other heavy oil reservoirs.

1.2 Thesis Organization

Chapter 2 contains an overview of the Grosmont formation geology and introduction of Indiana limestone. An emphasis is placed on zones of core availability within the Grosmont formation; specifically, the Grosmont C and Grosmont D reservoir units. Karstification and pervasive fracturing are controlling factors of reservoir quality in the Grosmont formation, creating increased bitumen-filled porosity and permeability. A brief review of Indiana limestone is presented with a comparison to the Grosmont formation rocks. Sample characterization techniques are also discussed and include helium pycnometry, mercury porosimetry, thin sections, and scanning electron microscope.

Chapter 3 provides background rock mechanics information relevant to the study. Since we are considering a rock formation buried at depth, a review of stress in the Earth's crust and faulting regimes is necessary. Then, the focus shifts to laboratory-based geomechanical experiments, where test types used in this study, and other common tests are reviewed. The theory of stress and strain, rock failure under compression and tension, criteria describing failure, and pore pressure effects are all presented in relation to the experiments performed in this study.

Chapter 4 outlines the process followed to prepare samples for mechanical testing from large blocks of Indiana limestone. All sample preparations and mechanical measurements were completed by the author, including implementation of the Hoek cell used in triaxial testing. The specifications are given for laboratory equipment employed in UCS, triaxial and Brazilian tensile testing. The workings of foil strain gauges and data collection are reviewed. Finally, the procedures of each mechanical test type are explicitly detailed.

The thesis is organized around Chapter 5, containing the Indiana limestone geomechanical measurements, which is a version of a manuscript in preparation for submission to a peer reviewed journal. The preceding chapters provide detailed information on geological aspects, rock mechanics theory, sample preparation, and testing procedures. As a result, some material of Chapter 5 may appear redundant, but it is impossible to avoid. A total of 59 Indiana limestone samples were mechanically tested under dry and saturated conditions. The measured compressional peak strengths are nearly identical, but subtle changes in elastic moduli and failure mode are observed. Tensile strength values show a discrepancy between dry and saturated testing conditions.

Chapter 6 incorporates the Grosmont formation Brazilian tensile strength testing results. This is a relatively short chapter because core limitations prevented extensive testing. The eight valid tests completed provide a range of tensile splitting strengths (4.3 - 11.4 MPa) for samples from the Grosmont C and D subunits. An apparent variation in strength within samples, dependant on orientation of stress with respect to rock fabric, was noted. This suggests strength anisotropy effects, but more testing is essential to confirm this and develop a Grosmont formation strength profile.

The thesis concludes with Chapter 7, where a summary of findings and commentary on the direction of future work is found.

The sample specifications are listed in the table of Appendix A. It is intended that the collected data also be published in a community accessible database.

1.3 Presentations and Publications

So far, this research has been presented at the Geoconvention conference (2016,2017) in Calgary Alberta. In 2016, most of the material presented was work by Morin on Grosmont stress and fracture characterization using image log data. The introduction of laboratory measurements and future integration with image logging constraints was also presented. In 2017, the presented material was focused on the methods and results from dry and wax-saturated Indiana limestone testing. The abstracts are shown below:

Morin, M.L. Fracture and Stress Characterization in the Grosmont. Geoconvention 2016.

Epp, T., Schmitt, D. R., Gray, K., & Nycz, J. Geomechanical Strength of a Porous Carbonate Saturated with a Highly Viscous Fluid: Implications for Production from the Grosmont Formation. Geoconvention 2017.

The Geoconvention 2016 presentation was presented by the author but composed by Morin. Some additional material related to laboratory testing was added to the presentation by the author.

An abstract has also been submitted for inclusion in the proceedings of the American Rock Mechanics Association's 52nd US Rock Mechanics/Geomechanics Symposium in 2018. It is titled: Geomechanical Properties of a Porous Carbonate Saturated with a Highly Viscous Fluid from Laboratory Testing.

The paper of chapter 5 will likely be submitted to a rock mechanics focused journal such as the Journal of Rock Mechanics and Geotechnical Engineering.

2. Geology and Sample Characterization

2.1 Introduction

This chapter provides an overview of the geology and character of the rocks under investigation in this study. A detailed description of Indiana limestone is presented in Chapter 5, and therefore, to avoid redundancy, only a brief review is found in this chapter. Numerous geological descriptions of the Grosmont formation have already been published, and a summary of this knowledge that motivates the present work is provided. Sample characterization techniques completed on both the Grosmont formation and Indiana limestone samples are reviewed. A brief discussion comparing the two mechanically tested rocks and substitution of paraffin wax for bitumen is also included in this chapter.

2.2 Grosmont Formation

The carbonate Upper Devonian-aged Grosmont formation is located entirely in Alberta approximately 300km north of Edmonton, or 100km west of Ft. McMurray (Fig. 2.1). It is part of the greater Western Canadian Sedimentary Basin (WCSB), and is known to contain bitumen, like the more well-known Athabasca oil sands located to the east and overlying parts of the Grosmont formation. The Grosmont formation is analogous to the modern Bahama banks platform [*Machel et al.*, 2012a; *Ardakani et al.*, 2014]. The eastern edge of the bitumen-bearing carbonates of the Grosmont formation subcrops beneath the Athabasca oil sands deposits, the western and southern margins are delineated by facies changes, and the northern extent is poorly characterized due to drilling restrictions in Wood Buffalo National Park [*Buschkuehle et al.*, 2007].

The Grosmont formation was first defined by Belyea [1952]. Much of the subsequent work was concentrated around pilot projects attempting commercial bitumen production (1980's and 2007-2015). Recent geological work on the Grosmont formation can be found in Buschkuehle et al. [2007], Hopkins et al. [2010], Machel et al. [2012b], Putnam et al. [2016] and Barrett [2016]. Recent geophysical investigations of the Grosmont formation have also been undertaken [*Bown*, 2011; *Ardakani et al.*, 2014; *Russel-Houston and Gray*, 2014; *Ardakani and Schmitt*, 2016, 2017]. Publications on the current pilot project, jointly operated by Laracina Energy and OSUM oil sands, have focused on engineering and production aspects [*Mohebati et al.*, 2014; *Yang et al.*, 2014], geology and geophysics [*Russel-Houston and Gray*, 2014; *Putnam et al.*, 2016], and petrophysics [*MacNeil*, 2015]. This pilot project has also motivated several academic studies including in situ stress analysis from image logs [*Morin*, 2017], and acoustic wave speed from ultrasonic experiments [*Ong et al.*, 2016; *Rabbani et al.*, 2017].

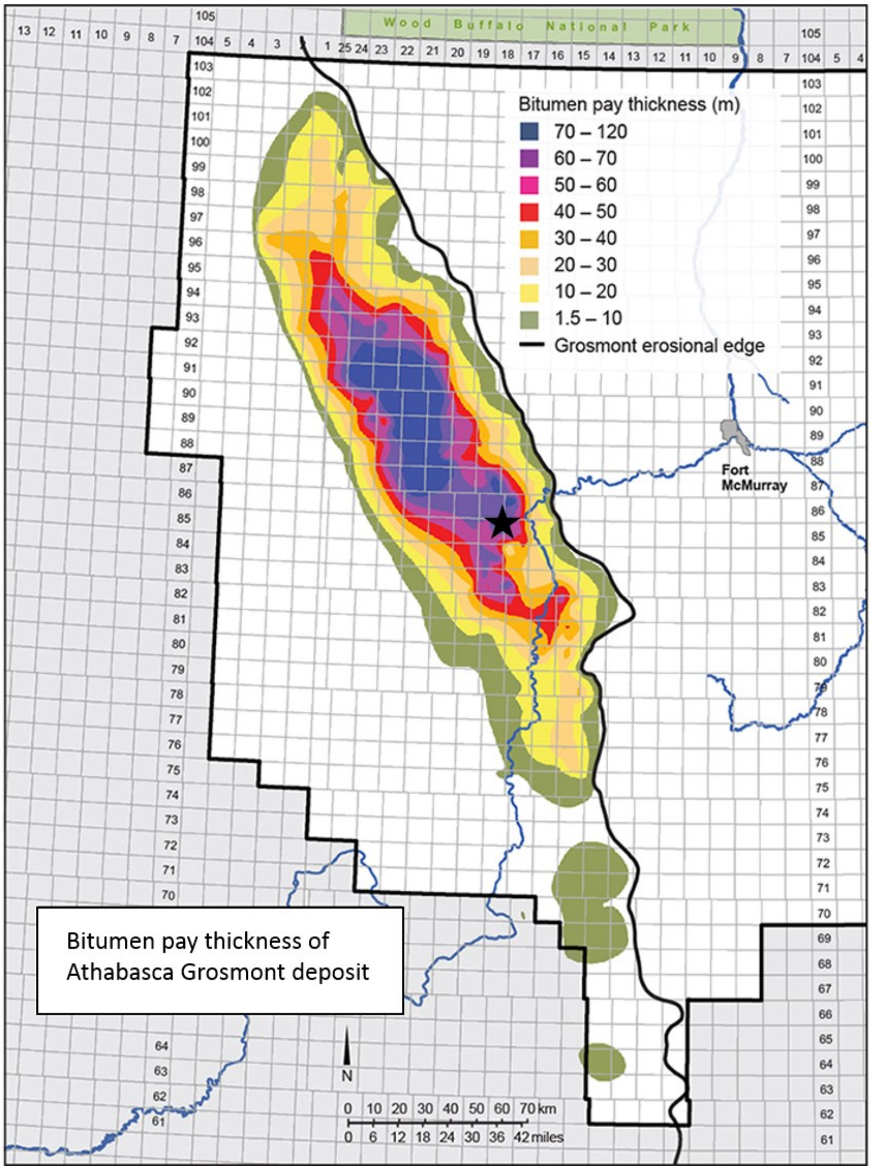

Figure 2.1 Grosmont formation bitumen pay thickness outline, modified from Alberta Energy Regulator [2015], with the approximate location of the Saleski pilot project (star). Reproduced with permission through the AER's copyright and disclaimer policy on noncommercial and educational reproduction (*http://aer.ca/copyright-disclaimer*).

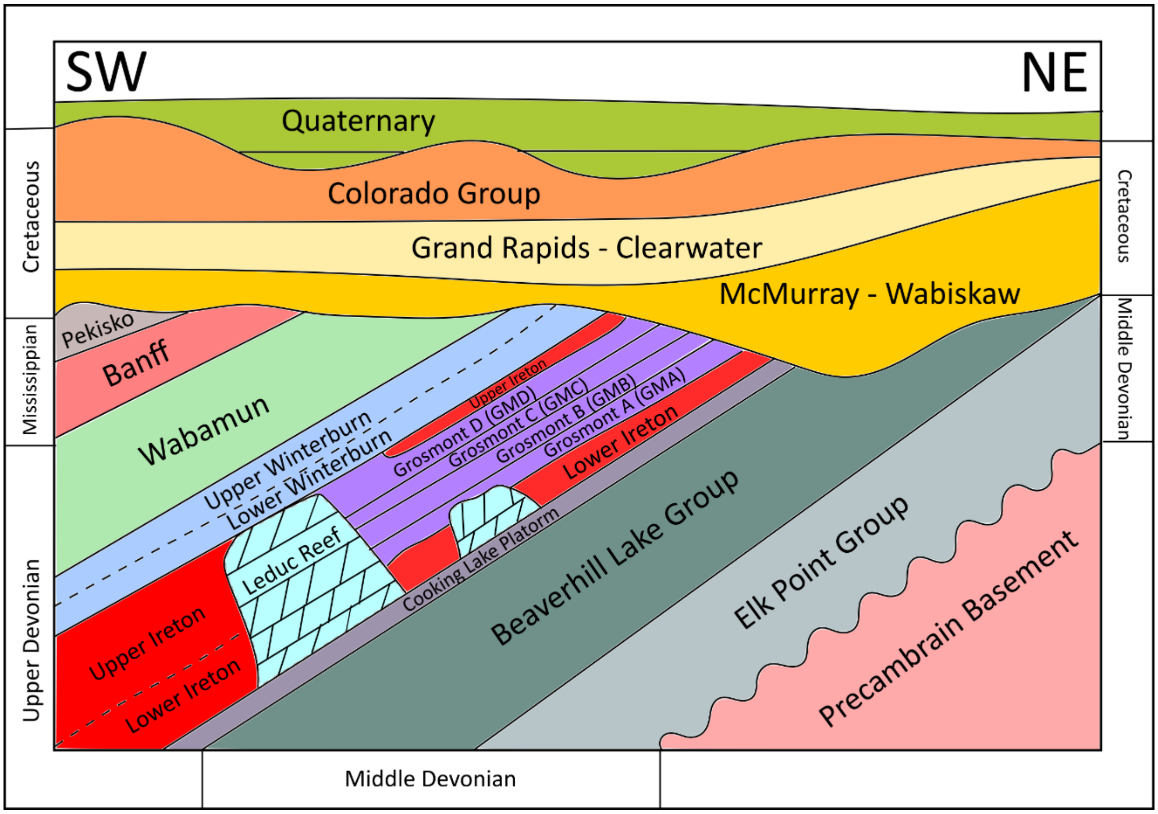

Figure 2.2 Stratigraphy of northern Alberta region modified from Buschkuehle et al. [2007].

The Grosmont formation is overlain by the Lower Winterburn group underlain by the Lower Ireton formation (Fig. 2.2). The Grosmont formation is subdivided into four units noted by Harrison [1982] as lower Grosmont (LG), Grosmont 1 (G1), Grosmont 2 (G2), and Grosmont 3 (G3), in ascending order. Recent literature uses the nomenclature Grosmont A (GMA), B (GMB), C (GMC), D (GMD) in place of LG, G1, G2, and G3, which is what will be used here. Each of the four units (GMA, GMB, GMC, and GMD) represent a shallowing up sequence [*Cutler*, 1983]. Three regionally extensive depositions of argillaceous material ("shale breaks" [*Harrison*, 1982]), distinctive on gamma-ray logs (Fig 2.3), mark the separation of the Grosmont formation into these four units. The shales were deposited during brief flooding or transgressional events at the beginning of each cycle [*Machel et al.*, 2012b]. Mercury-injection capillary pressure measurements, presented by Luo et al., [1994], suggest that these marls (shale breaks) will act as steam barriers during enhanced oil recovery processes, unless the shale is naturally fractured, or injection pressures exceed the rock strength. Bitumen can be found in all four Grosmont units, but the major reservoirs, where most bitumen is concentrated, are the GMC and GMD [*Mohebati et al.*, 2014].

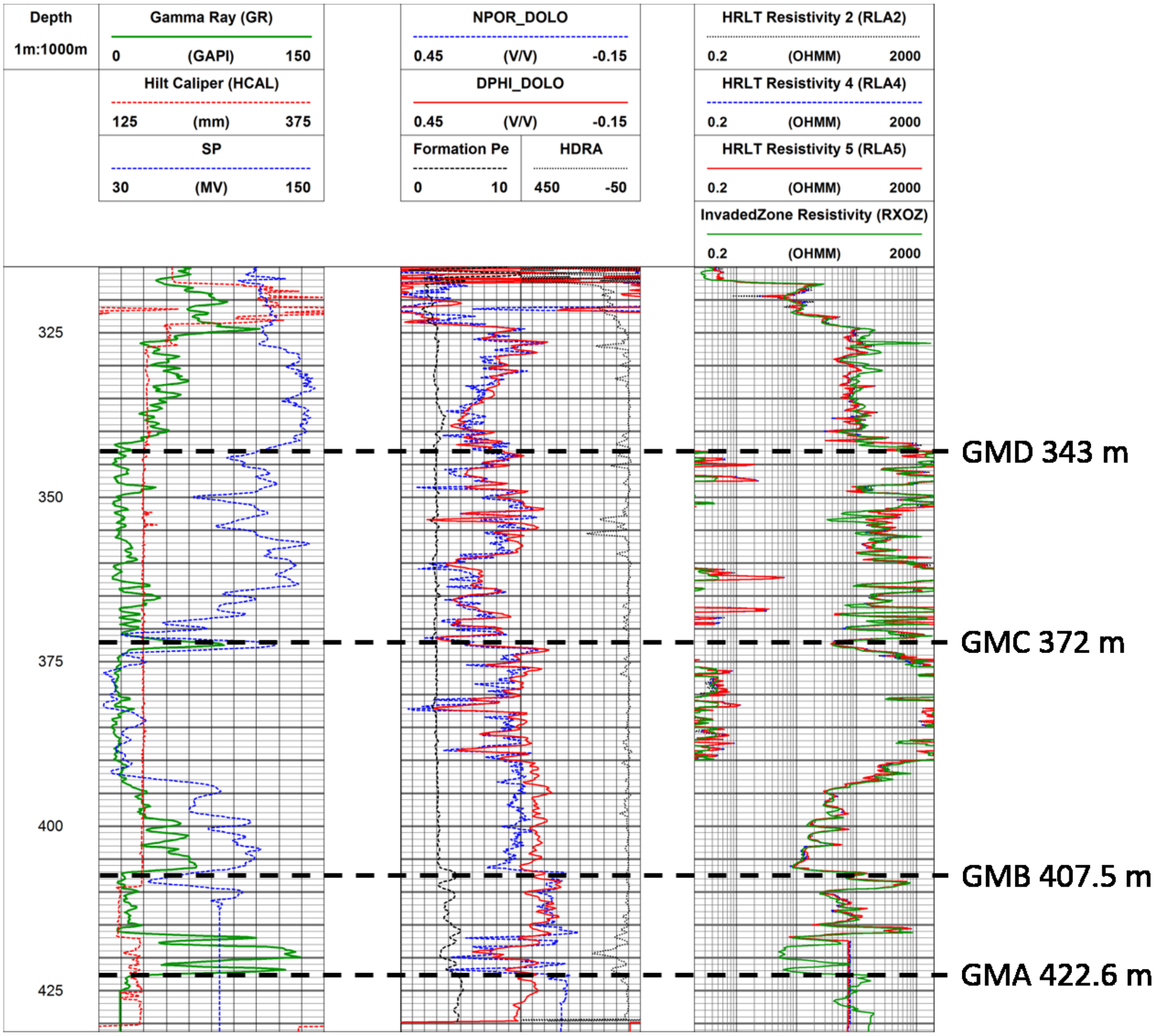

Figure 2.3 Well logs from well 100-1-27-85-19W4. High gamma ray signature marks the shale breaks separating the Grosmont formation into four members. The resistivity logs are notably high in the GMD and GMC indicating high bitumen saturation.

The main geological processes related to reservoir quality in the Grosmont formation are dolomitization, uplift and erosion, and karstification [*Barrett et al.*, 2008]. The karst topography was formed by dissolution of Grosmont formation rocks exposed to surface water. Karst features (vuggy dolostones, stratiform breccia, sinkholes) have been identified on the local scale [*Bown*, 2011; *Ardakani et al.*, 2014], regional scale using 3D seismic imaging [*Russel-Houston and Gray*, 2014] and from well log interpretation [*Dembicki and Machel*, 1996]. Salt dissolution along with tectonic processes are mostly responsible for the intense fracture network within the Grosmont formation [*Machel et al.*, 2012a]. While the heterogeneity of the reservoir poses challenges, the fracture network increases permeability, enabling steam to penetrate the reservoir and decrease the bitumen viscosity [*Yang et al.*, 2014]. The fracture network assists in overcoming the compositional differences within the Grosmont formation, making it a relatively homogenous reservoir at the regional scale [*Putnam et al.*, 2016]. Bedding features and fabric are evident in some Grosmont formation core samples and may indicate an inherent anisotropy. Morin [2017] logged natural fractures in Formation Microimager (FMI) logs and found a preferred North-South orientation of natural fracture strike; indicating there also is some structural anisotropy present.

From a reservoir perspective, the GMA and GMB members have generally economically unattractive porosity values (<10% for limestone) [*Theriault*, 1988] compared with the karsted and fractured GMC and GMD. The GMA transitions from limestone in the southeast to dolostone and shale in the northwest, influenced by subsidence thickening of the formation toward the northwest [*Hopkins et al.*, 2010]. The GMB similarly thickens and changes facies to the northwest, starting with stacked shale to calcareous nodular dolostones that eventually thin and shift to argillaceous dolostones [*Hopkins et al.*, 2010]. Regions of good porosity are present within the dolomitized zones of the GMA and GMB (up to 30%), but are too thin for current production techniques [*Theriault*, 1988].

The GMC ranges from ~32-40 m in thickness, and receives well-deserved attention for its reservoir properties. Well pairs drilled into the GMC have yielded the best production rates in recent pilot project operations [*Yang et al.*, 2014]. In the Saleski area, the GMC is often partitioned into additional units or facies based on distinct features and reservoir properties. The main reservoir, in the middle of the GMC, is flanked by high gamma-ray emitting argillaceous facies. The lower non-reservoir facies grades from argillaceous mudstone containing nodular limestone to lower clay content dolomudstone with small vugs [*Putnam et al.*, 2016]. The middle GMC (reservoir) can be subdivided into 3 additional facies, from oldest to youngest: 1) vuggy dolostones, 2) dolofudge, and 3) non-vuggy dolostones [*MacNeil*, 2015]. The bottom reservoir unit (Fig. 2.4 bottom photo) contains ample bitumen-saturated vugs (0.5-2.0 cm) and fractures creating a connected permeable network that, MacNeil [2015] emphasizes, has low surface area to volume ratio, positively affecting recovery. Moving upward, the vugs size (0.1-0.5 cm) and fracture intensity decreases [*Mohebati et al.*, 2014]. The “dolofudge” unit (after MacNeil [2015]) is thin (≤ 2 m), highly porous, bitumen-saturated unconsolidated dolomite. Non-vuggy laminated and wavy-laminated dolomudstone along with breccia confine the dolofudge. Above the dolofudge facies sits a clean (low gamma-ray), vuggy (≤ 0.5 cm) dolomudstone [*Mohebati et al.*, 2014]. The final unit, marking the top of the GMC and contact with GMD, is the thin (≤ 1 m) argillaceous facies often referenced as the “C-D marl”.

Average values for porosity and bitumen saturation for the GMC and GMD [*Mohebati et al.*, 2014] are shown in Table 1. The core samples made available to the Experimental Geophysics Group for rock physics and strength testing were recovered from the GMC and GMD reservoir units in the Saleski region. Three of the four Grosmont formation samples tested were from well 100-1-27-85-19W4 (UTM Zone 12 Northing 6251511 m, Easting 382333m). Core photos and FMI logs (Fig. 2.4-2.7) through the GMC and GMD, provide greater insight into structural features from this well. The FMI (from Schlumberger) is a wireline tool containing four pads, each with 48 buttons, pressed against the borehole wall. A current is sent from lower electrodes, through the borehole wall, to an upper electrode. Each button measures a microresistivity, from which an image is produced. The measured microresistivities are sensitive to physical properties of the formation composing the borehole wall and fluid or gas occupying the pore space.

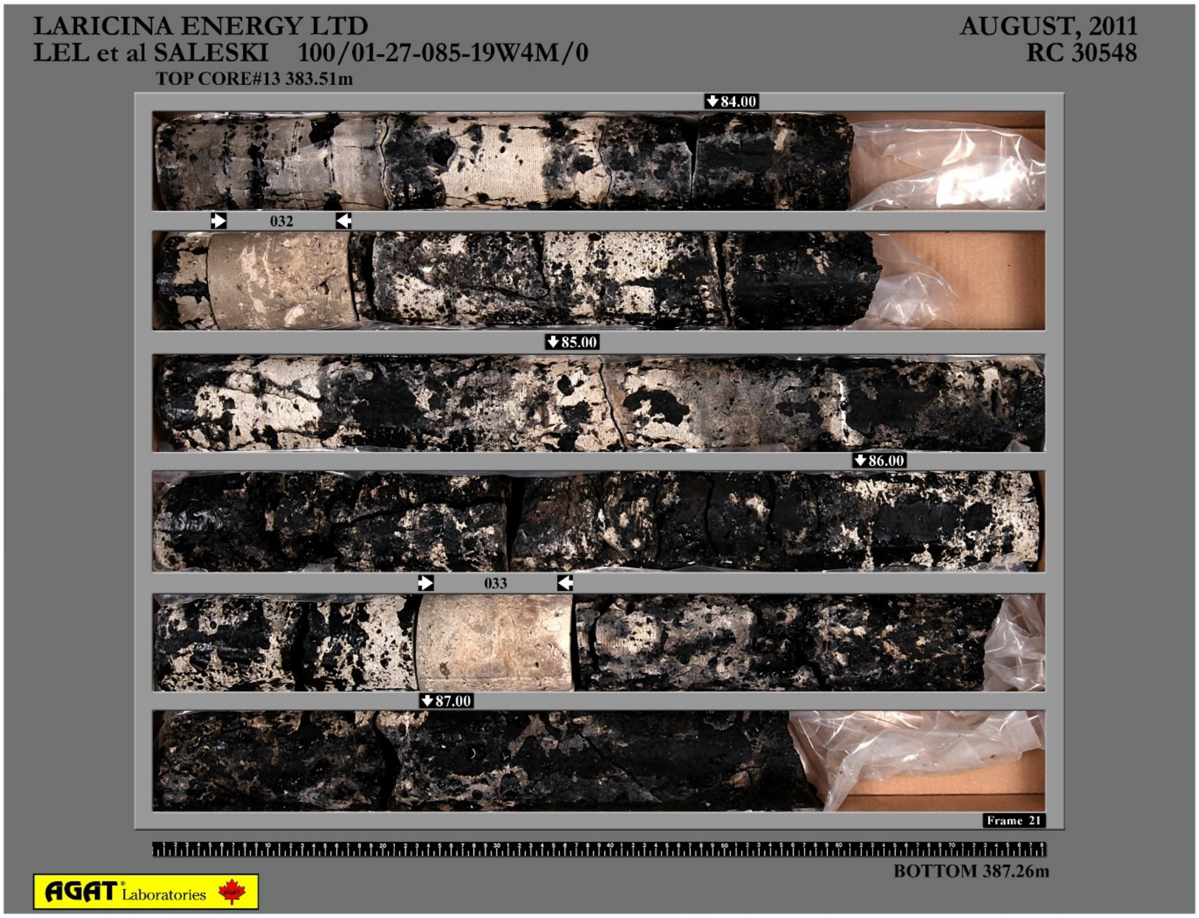

Figure 2.4 Core photos of GMC from well 100-1-27-85-19W4 (379.4 - 387.26 m). Upper photo (379.4-383.51 m): The top section (from 379.4 m to 382.4 m) is dolomite with vuggy porosity and bitumen (black) filled fractures. From 382.4-383.4 m, there are intervals of large porosity (>30%), making the dolomite hard to visualize due to the overwhelming presence of bitumen (Well Report). Bottom photo (383.51-387.26 m): The dominant structural features in this section of core are vuggy bitumen filled pores and natural fractures.

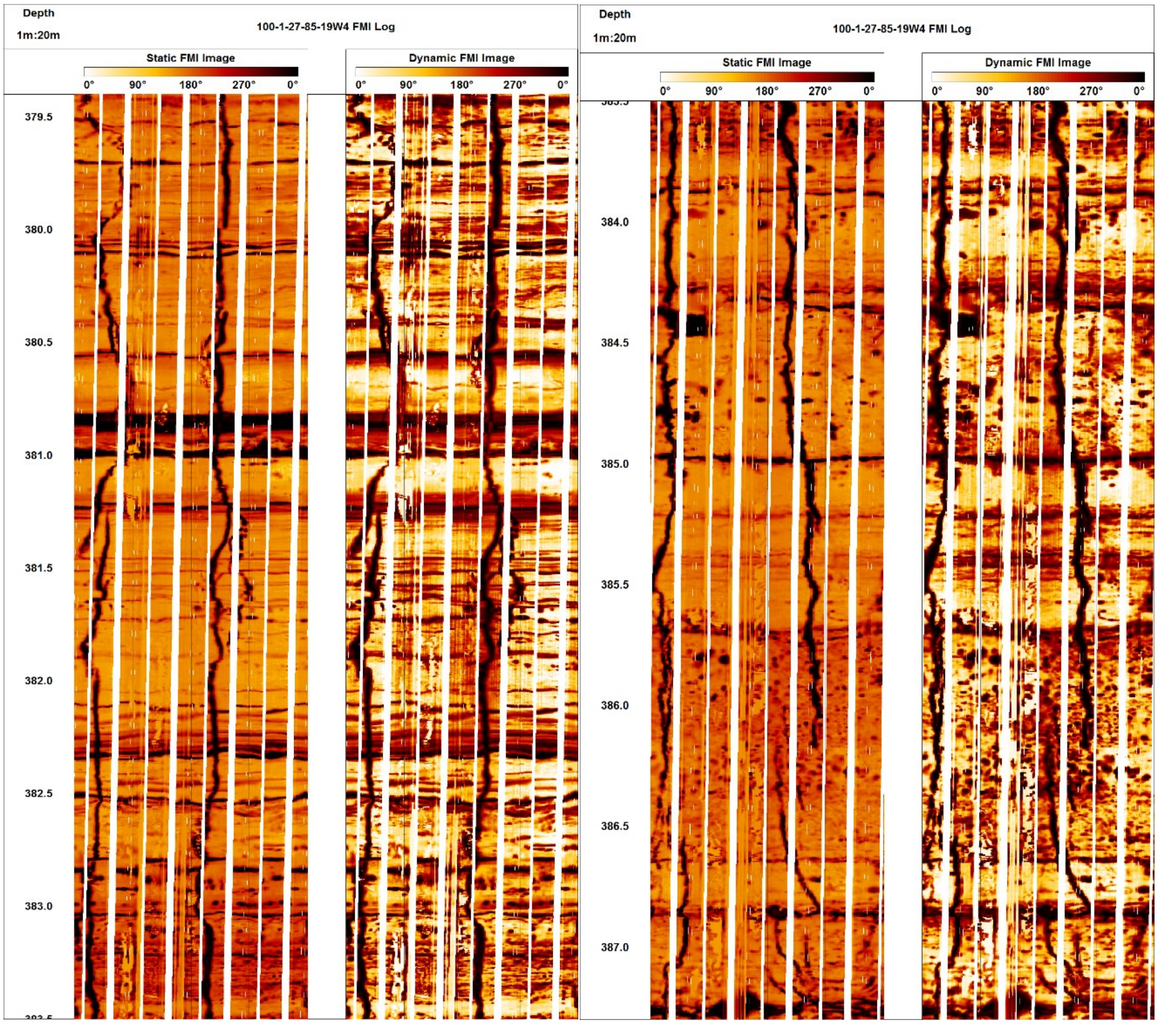

Figure 2.5 FMI log images through the GMC from well 100-1-27-8519W4. Both static and dynamic processing of the FMI logs are shown. The left and right FMI logs coincide with the top and bottom core photos in Fig. 2.4 respectively. Prominent drilling induced tensile fractures are present in the image logs as resistive vertical lines approximately 180° apart.

Although wells drilled into the GMD have been less productive to date, it still warrants attention as a thick (~30m) bitumen saturated reservoir. The GMD is typically divided into three subunits: lower, middle and upper. The lower unit is characterized by highly porous stratiform karst breccia that is mappable with inverted seismic volumes because of a strong acoustic impedance contrast (low density) [*Russel-Houston and Gray*, 2014]. A matrix of bitumen and dolomite crystals supports breccia clasts [*Mohebati et al.*, 2014]. The middle and upper units, separated by a thin marl, contain both vuggy and non-vuggy dolostones that are usually fractured [*MacNeil*, 2015].

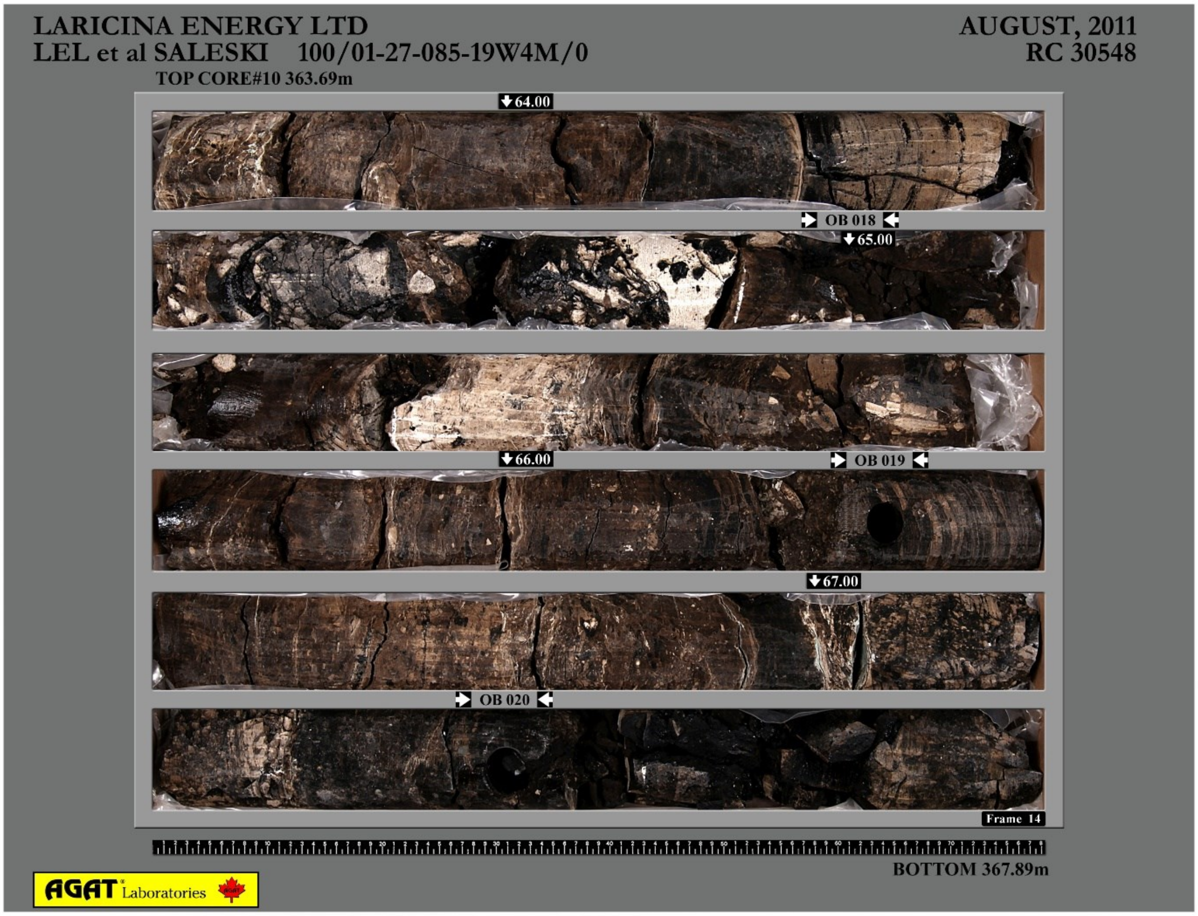

Figure 2.6 Core photo of GMD from well 100-1-27-85-19W4 (363.9 - 367.89 m). The lower brecciated subunit is shown, with bitumen oozing from vugs and fractures.

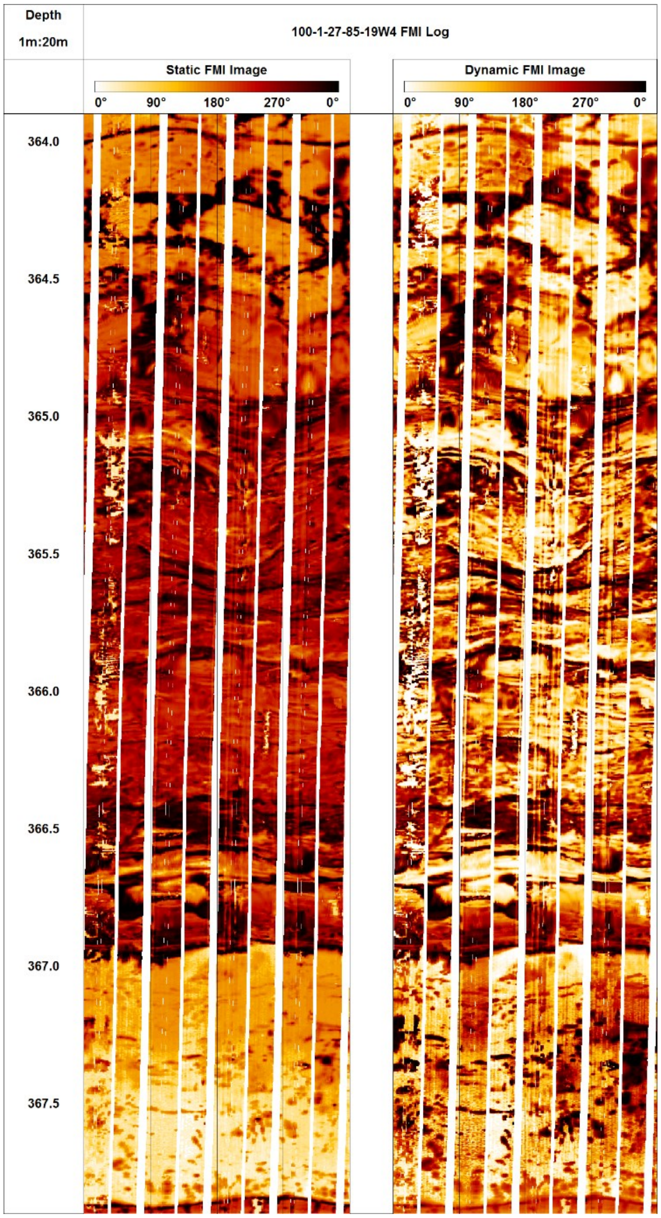

Figure 2.7 FMI log images through the GMD from well 100-1-27-8519W4 with same extents as core photos in Fig. 2.6. Dolostones transition from vuggy near the bottom of the log (~367.5m) to non-vuggy and fractured (~366m) in the middle, and lastly, brecciated at the top (~364.5m) of the shown section.

Table 1 Grosmont Fm. porosity and saturation

Unit	Porosity	Oil Saturation
Upper D	0.25	0.82
Middle D	0.18	0.65
Lower D	0.30	0.80
C-D Marl	0.15	0.60
Upper C	0.16	0.75

Middle C	0.32	0.82
Mid C Small Vugs	0.18	0.80
Mid C Large Vugs	0.14	0.65
Volume Weighted Average		
Grosmont C	0.25	0.75
Grosmont D	0.18	0.75
Grosmont C+D	0.22	0.75

The core photos (Fig. 2.4 and 2.6), image logs (Fig. 2.5 and 2.7) and geological description of the GMC and GMD reservoir facies provide insight into the difficulties associated with constructing a mechanical testing program. Most of the cored reservoir is highly fractured, preventing core samples from meeting the standard 2:1 length to diameter ratio for compressional strength testing. Other parts of the reservoir, such as the dolofudge facies, are unconsolidated and reduced to powder upon bitumen extraction. Both competent and weak zones need to be tested to build a robust strength profile of the Grosmont formation.

2.3 Indiana limestone

As noted, the extensive heterogeneity together with limited amounts of Grosmont core did not allow for extensive geomechanical testing and led to the selection of a more readily available proxy material. Although not a perfect analog, we selected Indiana limestone for our measurements.

The Mississippian aged Indiana limestone is comprised of fossil clasts bonded together by calcite cement. It is nearly monomineralic, composed of >97% calcite, and is absent of discernable bedding planes and structural features. These properties make it simple, and therefore popular, in the sample preparation and mechanical testing context. Indiana limestone samples were characterized using a variety of techniques including thin section (2.4), scanning electron microscope (SEM) (2.5), helium pycnometry (2.6) and mercury porosimetry (2.7). The prepared samples had an average porosity of 15.7% and bulk density of 2.26 g/cm^3. Individual sample specifications are listed in the table of Appendix A. These samples were cored from three blocks obtained commercially (from Kocurek Industries). Details of sample preparation are found in Chapter 4. Further details of Indiana limestone including thin section analysis are found in the paper of Chapter 5.

The principal disparities between GMC/GMD rocks and Indiana limestone include the: 1) fractured nature, 2) dolomitization, and 3) saturation constituents. The core photos and image logs (Fig. 2.4-2.7) provide evidence of the Grosmont formation's fractured nature. Uncompressed Indiana limestone samples were imaged with thin sections and SEM; and in stark contrast to the Grosmont formation, fractures are virtually absent. Indiana limestone is composed of greater than 97% calcite, while the Grosmont formation has been dolomitized. Mogi [1971a] performed rock strength tests using a true-triaxial system on both a limestone and dolomite and found that dolomite strength was more sensitive than limestone to effects of confining pressure (σ_2 and σ_3). Studies have shown that higher dolomite content results in greater rock strength [*Cleven*, 2008; *Kushnir et al.*, 2015].

Indiana limestone was ultimately chosen as the rock for the mechanical experiments of this study because it is an isotropic, readily available carbonate rock, and contains porosity values on the order of the Grosmont formation rocks. The Indiana limestone does have comparable average porosity (15.7%) to some parts of the Grosmont formation as shown in Table 1. There are also parts of the Grosmont formation (i.e. GMA) that contain limestone, and these sections are expected to behave closer to Indiana limestone. However, the GMA is not of primary importance in reservoir terms and so this relationship is likely not practically meaningful. The Grosmont formation and Indiana limestone are not interchangeable, but the goal of this study is to determine the strength effects of a viscoelastic material occupying pore space of a carbonate rock and paraffin wax saturated Indiana limestone meets this criterion.

The pore space in the Grosmont formation is saturated with a combination of ~6-9 API bitumen and gas. The Indiana limestone samples, used in experiments described later, are saturated with paraffin wax. Both bitumen and wax are practically solid at the temperatures in question, but of course are compositionally different. It is not known precisely how the more complicated hydrocarbon structure of the bitumen or combination with gas would affect the compressional or tensile strength of these rocks. However, it is known that the chemistry of pore fluid has a considerable influence on Indiana limestone strength [*Lisabeth and Zhu*, 2015]. In the literature paraffin wax has been used to build tectonic models [*Mancktelow*, 1988; *Brune and Ellis*, 1997; *Rossetti et al.*, 1999], but discussion of its physical properties is quite limited. An investigative program aimed at characterizing the physical properties of paraffin wax and bitumen is needed to fully realize the differences between the materials, and is outside the scope of this study.

2.4 Thin Sections

Samples were first impregnated with blue dye epoxy to highlight pore space and bond compressed samples that failed by shear fracture. Thin sections were prepared and scanned with a Nikon CoolScan 5000 ED (4000 dpi resolution) under plane and polarized light. Analysis and interpretation of thin sections is covered in the paper of Chapter 5.

2.5 Scanning Electron Microscope (SEM)

A SEM directs a beam of electrons at the sample surface. The electrons interact with the sample and an image of the topography, providing compositional information, is captured. The Zeiss EVO LS15 EP SEM has a resolution of approximately 100 nm. An image of undeformed Indiana limestone is shown below (Fig. 2.8). The collected images are used to investigate surface texture and features observed in thin section, including microcracks and pore structure, at a much finer scale. Samples for SEM imaging were prepared from dry Indiana limestone only, because paraffin wax could outgas and potentially damage the instrument.

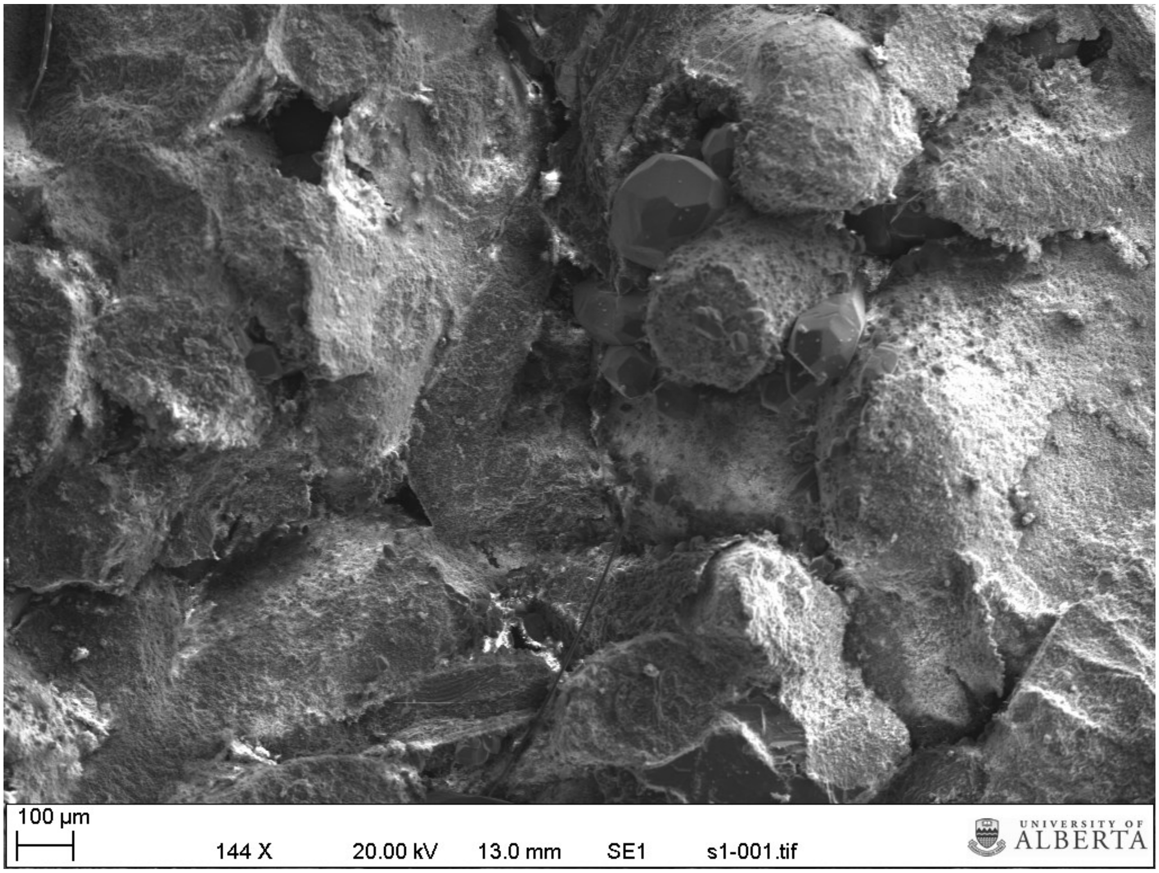

Figure 2.8 SEM image of untested Indiana limestone. Pores are clearly imaged at this scale and range in shape from nearly circular to slot-like.

2.6 Helium Pycnometer

After the dimensions of dry samples were measured, sample porosity was estimated using a helium pycnometer (Micromeritics model MVP-6DC). The gas expansion pycnometer is used to determine sample grain volume by employing Boyle's law, which states at constant temperature, an ideal gas (in this case helium is considered ideal) will show an inversely proportional relationship between pressure and volume:

$$P_1V_1 = P_2V_2 \tag{2.1}$$

where P is pressure and V is volume of gas. The pycnometer (Fig. 2.9) takes advantage of this relationship between pressure and volume by filling a reference chamber that has a known volume (V_r) with helium gas.

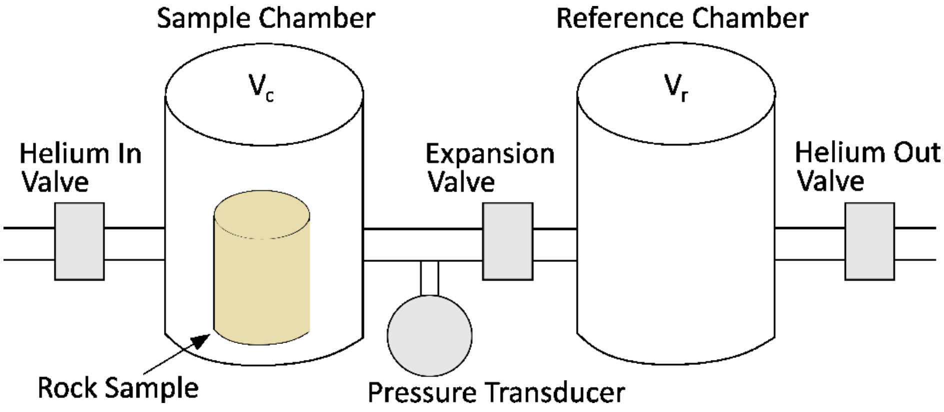

Figure 2.9 Helium pycnometer schematic. The pycnometer contains two cells, a reference cell and a sample cell (containing the rock sample to be measured), that are connected but can be isolated by a valve between the cells.

A pressure transducer records the pressure (P_r) of helium in the reference chamber. The valve between chambers is opened and helium gas travels into the second chamber containing the sample; and after equilibration with the larger total volume, the pressure (P_t) is measured. The volume V_c is calculated using Eqn. 2.1. The volume V_c represents the total volume of the reference and sample chamber minus the volume of rock grains. The sample grain volume is then:

$$V_g = V_c + \frac{V_r}{\left(1 - \frac{P_r}{P_t}\right)} \tag{2.2}$$

where V_g, V_c, V_r are the volumes of the sample (grain volume), empty sample chamber, and reference chamber respectively. The grain density is calculated from the grain volume measured by the pycnometer and sample mass:

$$\rho_g = \frac{m}{V_g} \tag{2.3}$$

Using grain density or volume, the porosity can be estimated because both bulk volume (V_b) and bulk density (ρ_b) of the sample is attainable from the measurements of dimension and mass. The porosity is then estimated by:

$$\varphi = 1 - \frac{V_g}{V_b} = 1 - \frac{\rho_b}{\rho_g} \tag{2.4}$$

The porosity of 19 samples were estimated by the helium pycnometry method. Results are displayed in Appendix A. There is an inherent error associated with the helium pycnometry technique in that all pore space in the rock is assumed to be connected and accessed by the helium when it enters the sample chamber. Some pores in rock are isolated and are not included in the porosity estimation. Intergranular porosity that may be present in some rocks is also not accounted for with this method.

2.7 Mercury Intrusion Porosimetry

The porosity and permeability of the Indiana limestone was measured using mercury intrusion porosimetry (MIP) developed by Drake and Ritter [*Ritter and Drake*, 1945]. One sample of Indiana limestone was measured estimating a permeability of 11.3 mD (1.12E-14 m^2) and measuring a 14.7% porosity. Mercury is a non-wetting fluid and as such needs to be forced into the samples pore space by external pressure. Small pores require a larger external pressure for mercury penetration than large pores, indicating an inversely proportional relationship between applied pressure and pore size. The volume of mercury penetrating the sample at varying applied pressure is measured with a highly sensitive mercury penetrometer. The intrusion of mercury is related to pore size via the Washburn [1921] equation:

$$Pr = -2\gamma Cos\theta \tag{2.5}$$

where P is the applied pressure, r is the pore throat radius, γ is the surface tension, and ϴ is the wetting angle. Drake and Ritter [1945] found mercury's wetting angle to range from 135 ° to 142° with an average of 140°. The average value of 140° is widely accepted and typically used in Eqn. 2.5. The surface tension of mercury (γ) is approximately 0.484 N/m at 25°C [*Kemball*, 1946]. Some authors [*Rigby and Edler*, 2002; *Kaufmann et al.*, 2009] suggest variations in ϴ and γ could be related to a variety of factors such as pore size, pore distribution, and surface nature.

Although mercury porosimetry provides a reliable estimate of porosity and an estimate of permeability, it has some limitations and assumptions summarized by Berodier et al. [2016]: 1) the Washburn equation assumes a cylindrical pore shape, 2) only pores connected to the outer sample are measurable, and 3) pore entry size is measured instead of actual pore size.

2.8 Summary

A description of the rocks tested with methods detailed in the following Chapters was reviewed. The Grosmont formation reservoir units GMC and GMD are highly fractured, and, although this is beneficial from a reservoir standpoint, it makes reliable and repeatable laboratory rock strength measurements difficult to achieve. Indiana limestone saturated with paraffin wax was introduced as an imperfect substitute to the bitumen-saturated Grosmont formation. Although these rocks exhibit differing geological characteristics, understanding the effects of highly viscous fluid on carbonate rock strength is valuable. The next chapter will review methods of determining the strength of the rocks described above.

3. Rock Mechanics Considerations

3.1 Introduction

The goal of geomechanical testing is to determine the strength of rock, and its behavior under various conditions (i.e. increased stress). Rock strength is one part of a geomechanical model, but realistic stresses must be applied in laboratory testing to produce useful results. Rock mechanics theory is fundamental in understanding how conditions in the Earth's crust affect rock deformation and failure. This chapter provides a review of rock mechanics theory germane to the experiments conducted in this work. Stress in the context of the earth's crust is reviewed first, followed by a summary of mechanical laboratory tests and analytical techniques applied to collected geotechnical data. The discussion is focused on the background of geomechanical tests employed in this study and analysis of the resulting data (detailed in Chapter 4 and 5). There are many texts offering more thorough reviews of rock mechanics testing and theory. The reader can refer to the classic text of Jaeger et al. [2007] covering rock mechanics fundamentals, brittle deformation of rock by Paterson [1978], and petroleum geomechanics by Fjaer et al. [2008] and Zoback [2007].

3.2 Stress in the Earth's Crust

Stress (σ) is defined as a force acting over a given area. The SI unit of measurement is the Pascal (Pa) which is equivalent to a N/m^2. Typical stress levels in the Earth's crust are on the order of megapascals (MPa). Force is a vector, so depending on the orientation at which it is applied to a cross-sectional area, normal (σ_{ij}) and shear (τ_{ij}) components of stress are generated (Eqn. 3.1). The stress acting on an infinitesimal cube of material (i.e. rock in Earth's crust) is completely defined by a 2nd order tensor:

$$\sigma = \begin{bmatrix} \sigma_{xx} & \tau_{xy} & \tau_{xz} \\ \tau_{yx} & \sigma_{yy} & \tau_{yz} \\ \tau_{zx} & \tau_{zy} & \sigma_{zz} \end{bmatrix} \tag{3.1}$$

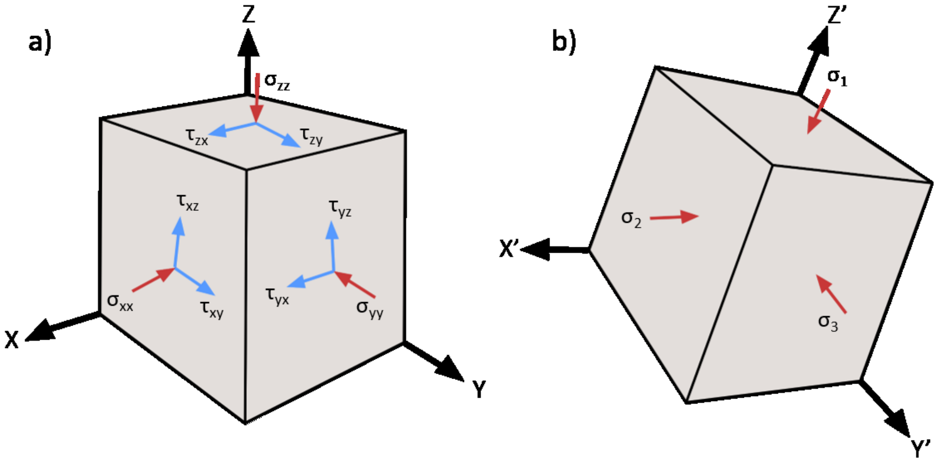

Figure 3.1 a) Complete stress tensor components acting on an infinitesimal cube of material in the XYZ coordinate system. b) Principal stresses acting on the cube after rotation to coordinate system X'Y'Z'. Rotation to this coordinate system eliminates the influence of shear stresses. Principal stresses are shown as compression-positive following the geosciences convention. Figure is modified after Schmitt et al. [2012].

The stresses acting perpendicular to the cube faces are denoted by σ_{xx}, σ_{xx}, and σ_{zz}. It is important to note that the tensor is symmetric (i.e. $\tau_{xy}=\tau_{yx}$), leaving six unique stress components. The shear stresses, τ_{xy}, τ_{xz}, and τ_{yz}, act parallel to the cube faces. The shear stress components can be eliminated through a coordinate frame rotation (see Schmitt et al. [2012]). This leads to a tensor defined by three stress magnitudes and three angles describing the rotation with respect to the known reference frame coordinates [*Zoback*, 2007]. The three stress magnitudes are known as the principal stresses:

$$\sigma' = \begin{bmatrix} \sigma_1 & 0 & 0 \\ 0 & \sigma_2 & 0 \\ 0 & 0 & \sigma_3 \end{bmatrix} \rightarrow \begin{bmatrix} S_H & 0 & 0 \\ 0 & S_h & 0 \\ 0 & 0 & S_v \end{bmatrix} \tag{3.2}$$

In the Earth, one of the principal stresses is usually vertical, due to gravitational loading. The three principal stresses are commonly defined as the vertical stress (S_v), maximum horizontal stress (S_H), and minimum horizontal stress (S_h). A rock buried at depth is subject to compressive forces, resulting in the rock mechanics convention defining compressive stresses as positive. The vertical stress, sometimes referred to as the overburden pressure, is estimated by integrating rock formation densities to a given depth (z) (Eqn. 3.3). Rock formation densities are usually measured with wireline logging techniques.

$$S_v = \int_0^z \rho(z)\, g dz \tag{3.3}$$

The horizontal stresses (S_h and S_H) are more complicated to estimate, and require multiple techniques to properly constrain including crossed dipole sonic logging, leak off testing, and image logs as outlined in Schmitt et al. [2012]. Stresses in the Earth become concentrated around boreholes [*Gough and Bell*, 1981; *Haimson and Herrick*, 1986] resulting in features, such as drilling induced tensile fractures and borehole breakouts, used to map the orientation, and bound the magnitude of horizontal stresses.

In the Western Canadian Sedimentary Basin (WCSB) of Alberta, Cox [1970] first noticed borehole elongations trending in the NW-SE direction (47°NW) from wireline caliper logs. Using additional wells Babcock [1978] confirmed the existence of these elongations, with approximate 40° NW azimuth, finding them independent of strata dip and formation age. The elongations were proposed, by Bell and Gough [1979], to be caused by borehole breakouts parallel to the least compressive horizontal stress direction. In the Saleski pilot area (Ch 2), Morin [2017] mapped stress orientations from drilling induced tensile fractures (DITF) observed in FMI logs through the Grosmont formation, and as expected, found a similar horizontal stress regime to Bell and Gough [1979], with the maximum horizontal stress, S_H, oriented at an azimuth of 50°NE.

Faults and fractures naturally occur in the Earth as the result of sediment loading and tectonic forces among other processes. The faults observed in the Earth were classified (Fig. 3.2) in terms of principal stresses by Anderson [1951], defining normal, reverse, and strike-slip faults.

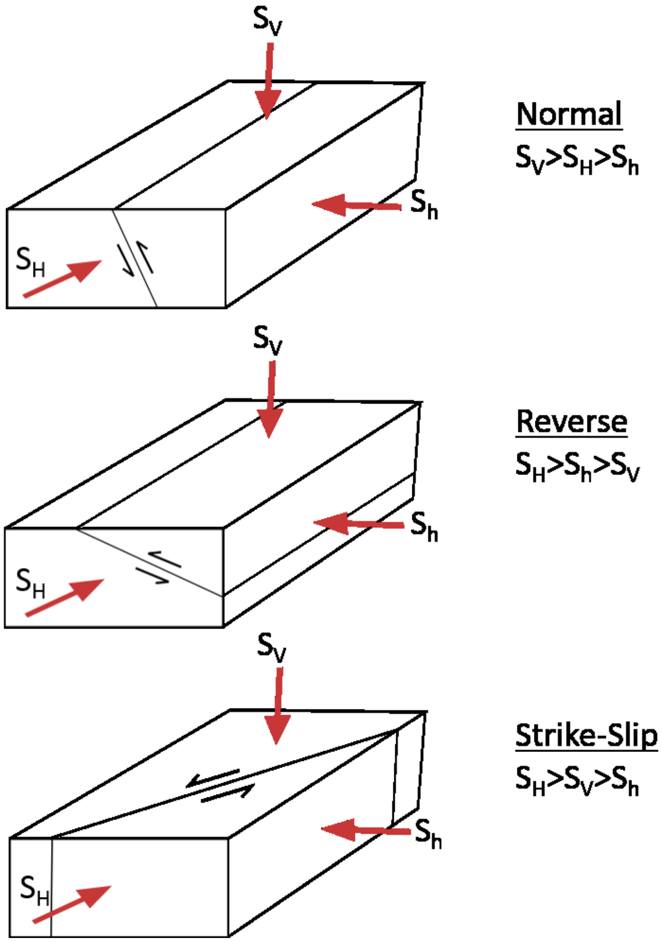

Figure 3.2 Diagram of faults with principal stress states from Anderson classification.

3.3 Laboratory Strength Tests

Rock strength is defined as the applied load a rock can support. As a rock is subjected to stress, it deforms and at some stress level the rock will no longer be able to support the load resulting in failure. The stress level, at which the rock fails, is important to understand in engineering applications, especially when perturbing the stress field in the Earth by drilling a borehole. Several laboratory-based geomechanical tests have been developed to simulate stresses acting on a rock in the Earth's crust and monitor deformation and failure of a rock sample under varied stress states. Rock strength is scale dependant and a prepared laboratory sample may have a higher recorded strength than a larger rock volume (i.e. at the reservoir scale) due to the increased number of flaws present in a larger volume sample [*Adey and Pusch*, 1999]. The compressive and tensile rock strength tests utilized in this study are diagrammed below in Fig. 3.3. Sample preparation and testing procedures are documented in Chapter 4.

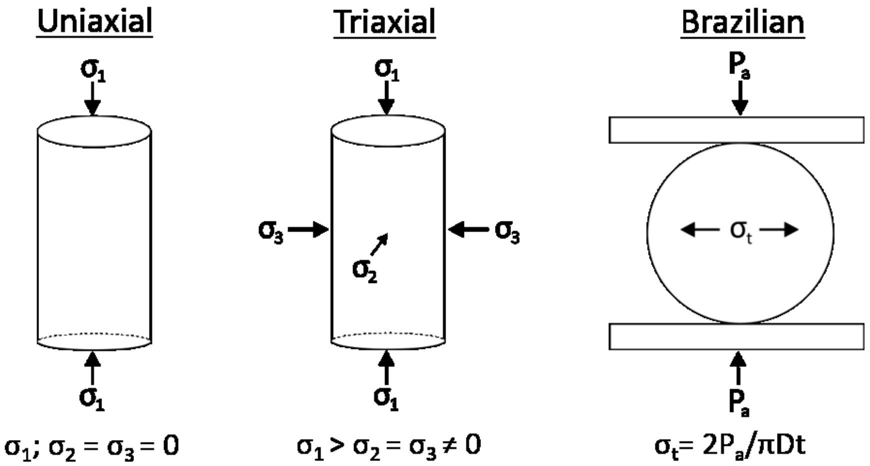

Figure 3.3 Diagrams of laboratory strength tests performed in this study. The uniaxial and triaxial tests are compressional strength tests, and the Brazilian test applies compressive force to opposing points on the disk circumference creating tension through the center of the disk. The principal stresses are σ_1, σ_2, and σ_3 in compressive testing. The Brazilian tensile disk dimensions have diameter (D) and thickness (t), which are used along with applied pressure (P_a) to calculate tensile stress (σ_t).

In the uniaxial compressive strength (UCS) test only an axial stress (σ_1) is applied to a cylindrical rock sample. This test is also called the unconfined compressive strength test, as there is no applied confining pressure. For triaxial testing, in addition to axial stress (σ_1), equal horizontal stresses (σ_2=σ_3≠0) are applied to the sample. Other compressive strength tests include hydrostatic and polyaxial tests. In hydrostatic testing a sample encased in plastic or copper jacketing is placed in a pressure chamber and subjected to one encompassing stress. Hydrostatic testing measures a rock's compressibility and pore collapse pressure. In polyaxial (or "true" triaxial) testing, the sample is machined into a cube and all three principal stresses can vary (like Fig 3.1b). The advantage is a closer representation of in-situ stresses, however, the sample preparation and procedures involved in polyaxial tests make them very difficult to perform [*Mogi*, 1971b; *Haimson and Chang*, 2000].

The Brazilian tensile strength (BTS) test is an indirect method for determining the tensile strength of a material. The development and popularity of BTS testing has been driven by challenges associated with preparation and execution of direct tensile strength (DTS) testing methods [*Jaeger et al.*, 2007]. Disks are prepared with a thickness (t) to diameter (D) ratio between 0.2 and 0.75. The approximate point load applied (P_a) to the disk creates tension through the center of the disk (σ_t).

3.4 Rock Deformation and Failure

The following analysis of rock deformation and failure assumes a homogenous and isotropic rock, which fortunately, is a reasonable approximation for Indiana limestone chiefly used in this study. However, heterogeneities exist in thin section and under SEM, even in this rock, selected for its homogenous nature at the core scale.

3.4.1 Stress and Strain in Laboratory Tests

Cylindrical rock samples deform under the compressive stresses of UCS and triaxial tests. Strain (ε) is defined as a proportional change in dimensions due to an applied force with respect to the original dimensions. Strain shortening is defined as positive in geoscience terms. Following standard notation, strain is described by:

$$\varepsilon_{ij} = \frac{1}{2}\left(\frac{\delta u_i}{\delta x_j} + \frac{\delta u_j}{\delta x_i}\right) \tag{3.4}$$

The axes are denoted by *i* and *j*, and displacements with respect to the axial directions are u_i and u_j. This results in the three-dimensional strain tensor:

$$\varepsilon = \begin{bmatrix} \varepsilon_{11} & \varepsilon_{12} & \varepsilon_{13} \\ \varepsilon_{21} & \varepsilon_{22} & \varepsilon_{23} \\ \varepsilon_{31} & \varepsilon_{32} & \varepsilon_{33} \end{bmatrix} = \begin{bmatrix} \frac{\delta u_1}{\delta x_1} & \frac{1}{2}\left(\frac{\delta u_1}{\delta x_2} + \frac{\delta u_2}{\delta x_1}\right) & \frac{1}{2}\left(\frac{\delta u_1}{\delta x_3} + \frac{\delta u_3}{\delta x_1}\right) \\ \frac{1}{2}\left(\frac{\delta u_2}{\delta x_1} + \frac{\delta u_1}{\delta x_2}\right) & \frac{\delta u_2}{\delta x_2} & \frac{1}{2}\left(\frac{\delta u_2}{\delta x_3} + \frac{\delta u_3}{\delta x_2}\right) \\ \frac{1}{2}\left(\frac{\delta u_3}{\delta x_1} + \frac{\delta u_1}{\delta x_3}\right) & \frac{1}{2}\left(\frac{\delta u_3}{\delta x_2} + \frac{\delta u_2}{\delta x_3}\right) & \frac{\delta u_3}{\delta x_3} \end{bmatrix} \tag{3.5}$$

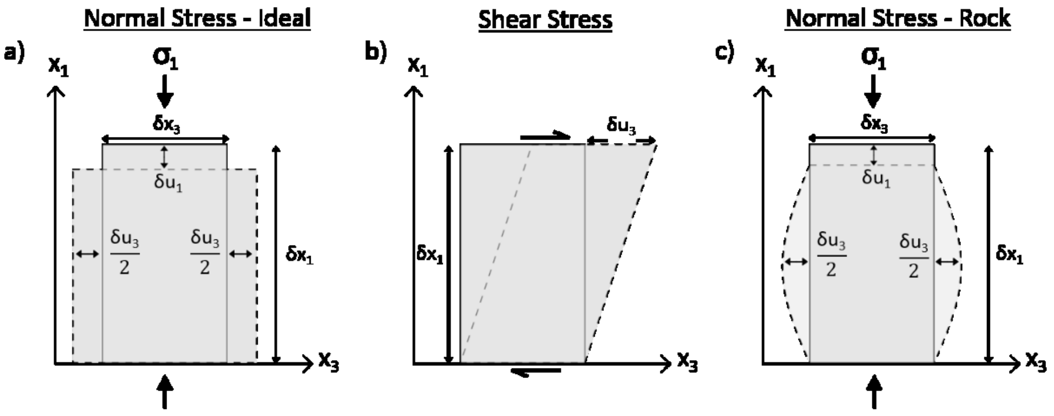

Figure 3.4 a) deformation of linear elastic material from applied normal stress, b) deformation of elastic material from applied shear stress, and c) deformation of rock sample in with frictional effects common in UCS testing.

Consider the configuration of Fig. 3.4a (ideal UCS test of linear elastic material), with the x_1-axis in the direction along the cylindrical sample's length (and direction of applied stress), and x_3-axis in the lateral direction. The sample of length, δx_1, and width, δx_3, will shorten (by δu_1) in the axial direction and expand (by δu_3) in the lateral direction as the axial stress (σ_1) is applied. The axial and lateral strains are defined as:

$$Axial\ Strain = \varepsilon_{11} = \frac{\delta u_1}{\delta x_1} \tag{3.6}$$

$$Lateral\ Strain = \varepsilon_{33} = \frac{\delta u_3}{\delta x_3} \tag{3.7}$$

If the applied stress and resulting strains are known, then two elastic moduli, Young's modulus *(E)* and Poisson's *(v)* ratio, are found by:

$$E = \frac{\sigma_1}{\varepsilon_{11}} \qquad v = -\frac{\varepsilon_{33}}{\varepsilon_{11}} \tag{3.8}$$

Young's modulus relates a material's ability to resist deformation under stress. If the material is very rigid it will have a high Young's modulus value. Poisson's ratio is a measure of a material's lateral expansion relative to it's axial contraction under applied stress.

The strain response to applied normal stress in Fig. 3.4a is representative of ideal materials and testing conditions. Realistically, under UCS testing conditions, a rock sample behaves slightly differently than the ideal material. Friction at the contact points of applied axial stress can restrict sample expansion at the ends [*Jaeger et al.*, 2007]. The non-uniform stress state results in a barrel shaped sample as depicted in Fig. 3.4c.

Strain gauges (detailed in Chapter 4) are arranged on rock samples to monitor deformation in the axial and lateral direction (Fig. 3.3) under compressive stress. The applied stress and resulting strains are continuously recorded. A typical axial stress-strain curve for a UCS test is shown in Fig. 3.5, below.

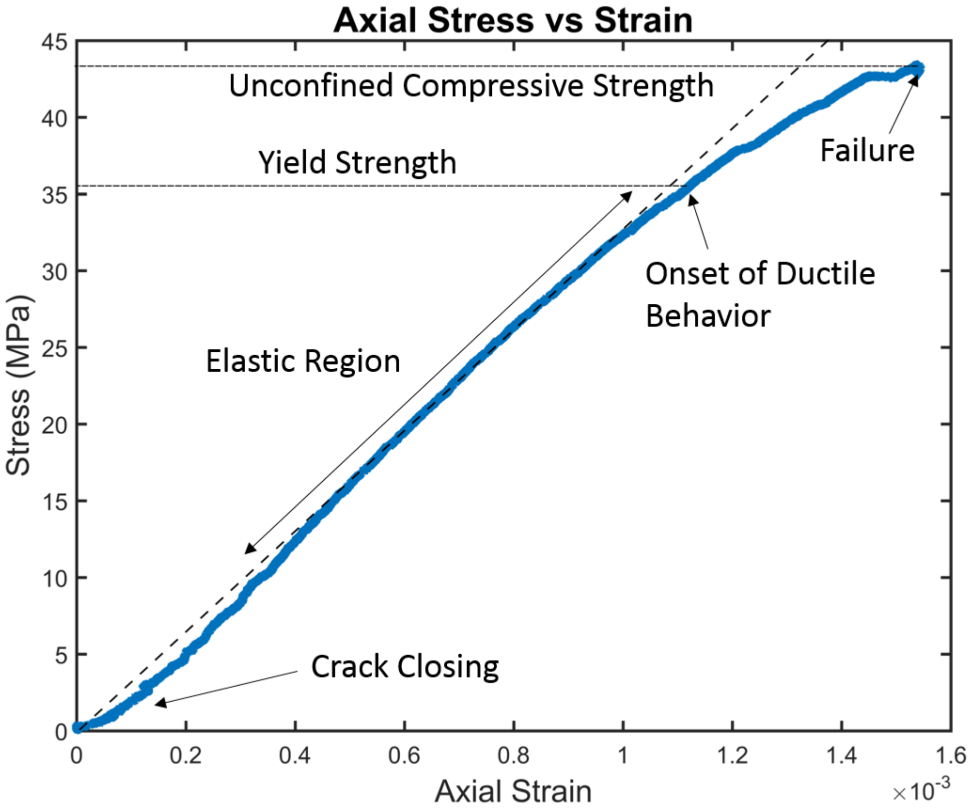

Figure 3.5 Axial stress-strain curve typical of data collected in the laboratory during UCS testing (from tested sample S49). Dashed line represents behavior of a perfectly linear elastic material.

Rock is generally porous and heterogenous on some scale, making it more complicated to analyze than a well-behaved metal or other material [*Jaeger et al.*, 2007]. To illustrate this, Fig 3.5 includes a dashed line emblematic of linear elastic behavior, but markedly different than often nonlinear elastic rocks [*Schmitt et al.*, 2012]. The axial stress-strain curve of the rock sample in Fig. 3.5 deviates from the dashed line exhibiting elastic, ductile, and brittle behavior. Near the origin, positive curvature is indicative of crack closing. The stress from initial loading forces microcracks in the rock to close. In some cases, this region is nearly elastic. The main region of elastic behavior contains the noticeably linear portion of the curve. This range of applied stresses will not cause permanent sample deformation. The slope of the elastic portion is equal to the sample's Young's modulus. The yield strength is defined where the curve departs from linear and gains negative curvature. Stresses greater than the yield strength causes permanent changes in sample shape and properties. Finally, sample failure occurs by brittle fracture, usually at or very close to the maximum recorded stress level. The UCS is defined as the maximum applied stress supported by the sample. For the experiments performed in this study, the stress-strain curve terminates abruptly at failure because stress is the controlled variable in the experiments. To visualize the full stress-strain curve extending into the post-failure region strain must be a controlled variable and this is not possible without a servo-controlled testing machine.

3.4.2 Role of Confining Pressure

The addition of confining pressure (σ_3) in triaxial experiments has been known, for more than a century, to increase peak strength and ductility of rock samples [*Jaeger et al.*, 2007]. Ductile behavior is defined as the ability of rock to deform without the loss of compressive strength [*Byerlee*, 1968], or gross fracturing [*Paterson*, 1978]. Some rocks with relatively high porosity and low strength, like Indiana limestone, exhibit ductile behavior [*Robinson*, 1959; *Schwartz*, 1964], even at rather low confining pressures (≤12 MPa) [*Walton et al.*, 2015]. Mogi [1966] found the critical confining pressure inducing ductility was generally lower for the weaker carbonate rocks. One example (there are many studies in the literature), from Paterson [1958], of increasing confining pressure effects on strength and ductility is shown in Fig. 3.6.

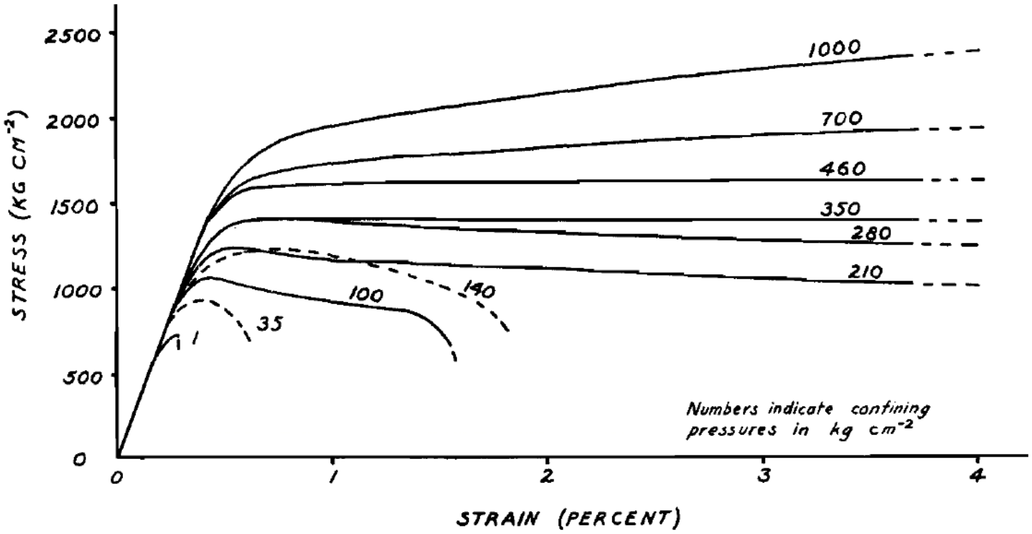

Figure 3.6 Stress-strain curves for various confining pressures. Figure is from Deformation in Wombeyan Marble by Paterson [1958]. Permission to reprint granted by the Geological Society of America.

The conversion to more familiar MPa units in Fig. 3.6 is 10 kg/cm^2 = 1 MPa (kg/cm^2 is an old force/area unit not an SI unit). The triaxially tested samples in Fig. 3.6 show the direct relationship of increased peak strength with larger confining pressures. At low confining pressure the rocks fail by brittle fracture and the stress-strain curve follows a similar path to the UCS tests. As the confining pressure increases up to 14 MPa, the strain reached before failure also increases. The sample behavior changes to fully ductile at pressures ≥ 21 MPa. Strain hardening, marked by positive slope with increasing strain beyond the yield point, is observed at confining pressures ≥ 46 MPa.

Some discussion of peak strength (or ultimate strength) has proceeded, and in cases of brittle failure, it is easily defined as the greatest stress endured prior to macroscopic fracture; but a definition of rock strength is needed for samples displaying ductile behavior. An arbitrary strain (usually 0.2%), is chosen by some authors (i.e Robinson [1959]). Topping [1955] suggested the intersection of the straight portions of the stress-strain curve, leading to a point off the curve path. The method used in this study, also adopted by Schwartz [1964], was proposed by Jeffreys [1959]. He defined failure at the point where stress-strain slope change became a minimum (tangent modulus a minimum). The mathematical definition is [*Schwartz*, 1964]:

$$\frac{\partial^2 \sigma}{\partial \varepsilon^2} = o \tag{3.9}$$

3.4.3 Rock Failure in Compression

As outlined above, the compressive stresses applied in laboratory testing can exceed the strength of rock samples causing shear failure along a fracture plane. The Mohr diagram (Fig. 3.7 b,c) graphically relates the shear (τ_f) and normal stresses (σ_n) acting on a developed failure plane under applied principal stresses (σ_1, σ_3).

$$\tau_f = \frac{1}{2}(\sigma_1 - \sigma_3)\sin 2\beta \tag{3.10}$$

$$\sigma_n = \frac{1}{2}(\sigma_1 + \sigma_3) + \frac{1}{2}(\sigma_1 - \sigma_3)\cos 2\beta \tag{3.11}$$

where β is the angle between σ_1 and σ_n (Fig. 3.7a). Failure criterion describe rock failure observed from a series of compressive strength tests, and predict behavior at untested principal stresses. The envelope fit to a series of Mohr circles is called the Mohr envelope (Fig. 3.7b), where the failure shear stress is simply a function of normal stress:

$$\tau_f = f(\sigma_n) \tag{3.12}$$

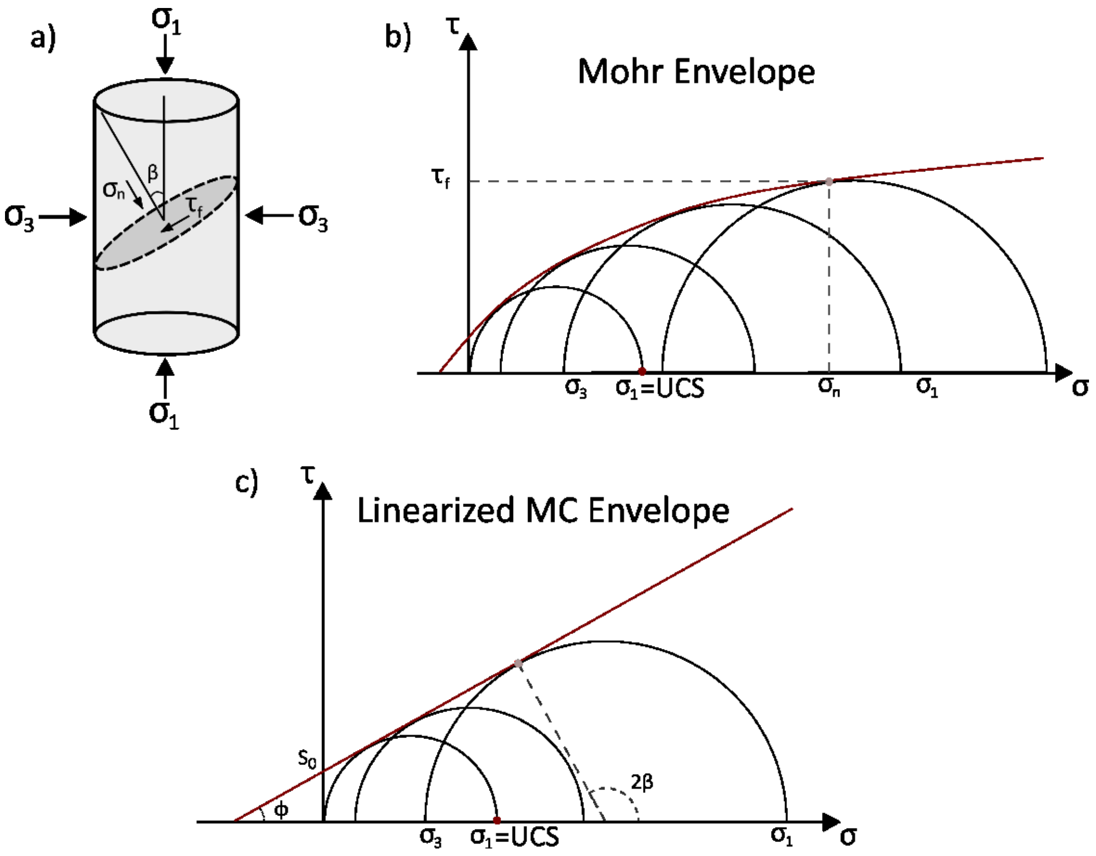

Figure 3.7 a) Stresses developed on a shear failure plane in a core sample under triaxial stress. b) Diagram of Mohr envelope fit to a series of triaxial tests. c) Diagram of the linearized Mohr-Coulomb failure criterion.

The point where the envelope and Mohr circle touch defines failure inducing shear and normal stresses. As a result, it is impossible for a Mohr circle to surpass the envelope boundary, but samples under principal stress states producing a Mohr circle below the envelope will remain intact.

As discussed, for most rocks, ultimate strength increases with increasing σ_3, but at high σ_3 the relationship becomes nonlinear and the Mohr failure envelope flattens. At low and moderate confining pressures, the relationship often remains approximately linear, and the linearized Mohr-Coulomb (MC) failure criterion (Fig. 3.7c) is commonly used:

$$\tau = S_0 + \mu \sigma_n \tag{3.13}$$

where S_0 is termed the cohesion, and μ is the coefficient of internal friction. In relation to the linearized MC failure envelope, S_0 represents the τ-intercept, and μ is the slope. The angle φ in Fig. 3.7c, called the internal angle of friction, is related to μ and β by:

$$\tan \varphi = \mu \tag{3.14}$$

$$\beta = \frac{\pi}{4} + \frac{\varphi}{2} \tag{3.15}$$

S_0 is not measurable from laboratory testing and can be expressed in terms of the UCS (C_0) and μ [*Zoback*, 2007] or φ [*Fjaer et al.*, 2008]:

$$S_0 = \frac{C_0}{2}\left[\frac{1-\sin\varphi}{\cos\varphi}\right] = \frac{C_0}{2}\left[(\mu^2+1)^{\frac{1}{2}} + \mu\right]^{-1} \tag{3.16}$$

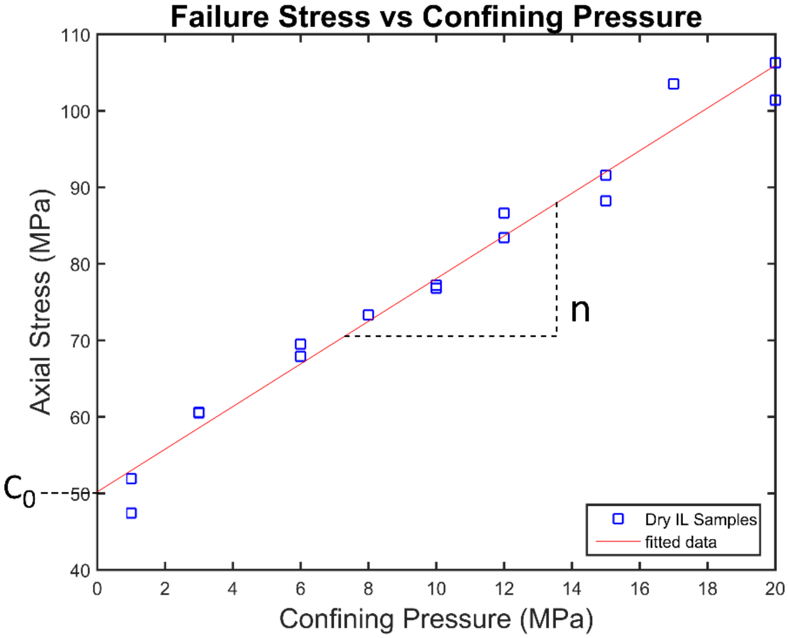

Figure 3.8 Example of ultimate strength data from a series of triaxial tests on dry Indiana limestone, used to determine C_0 and the slope of best fit, n.

It is possible to estimate C_0 from a series of triaxial testing results. Fig. 3.8 displays results from a series of triaxial tests on dry Indiana limestone, with best fit from linear regression. The C_0 value is read off the intersection of axial stress axis and best fit line. The best fit line slope (n) can also be used to find μ [*Zoback*, 2007]:

$$\mu = \frac{n-1}{2\sqrt{n}} \tag{3.17}$$

The discussion of MC failure criterion has been developed in the τ-σ plane, but the criterion can also be shown in the principal stress plane (σ_1, σ_3) [*Jaeger et al.*, 2007]:

$$\sigma_1 = C_0 + \sigma_3 tan^2\beta \tag{3.18}$$

Another popular failure criterion for triaxial datasets is the empirical, nonlinear Hoek-Brown (HB) criterion [*Hoek and Brown*, 1980]. The HB failure criterion for intact rocks is:

$$\sigma_1 = \sigma_3 + C_0 \left(m_i \frac{\sigma_3}{C_0} + 1 \right)^{0.5} \tag{3.19}$$

where m_i is a material constant, with estimated value of 10 for limestone [*Hoek and Brown*, 1997]. Both the MC and HB failure criteria assume rock behavior is not influenced by the intermediate stress (σ_2). This is sufficient for triaxial strength experiments (where $\sigma_2 = \sigma_3$) and rocks that experience little σ_2 influence; however, it is known that σ_2 has a significant impact on some rock types [*Colmenares and Zoback*, 2002]. Mogi [1971a] performed true triaxial tests on carbonate rocks, both limestone and dolomite, and found increasing σ_2, much like increasing σ_3, led to greater ultimate strength of samples (except with very high σ_2). An increased σ_2, with respect to a constant σ_3, has also long been observed to embrittle rock samples [*Heard*, 1960; *Handin et al.*, 1967; *Mogi*, 1971b]. There are many failure criteria (i.e. Wiebols and Cook, Lade, Drucker-Prager, von Mises and modified versions of these and others) that account for σ_2, making them more suitable for describing failure under true triaxial tests. The application of these criteria to a variety of rock types are reviewed by [*Colmenares and Zoback*, 2002; *Benz and Schwab*, 2008; *Zhang et al.*, 2010].

3.4.4 Pore Pressure Effects

Rock is a porous material and in the Earth's crust fluids, such as water and bitumen, commonly occupy pore space. So far, the discussion of stress, strain and laboratory experiments has ignored the effects of pore pressure on rock strength. Here, we introduce the concept of effective stress, recognizing that it does not fully describe the intricacies of poroelastic behavior of rock in all situations. The concept of effective stress was developed in the context of soil mechanics by Terzaghi [1936], but the simple theory is also applicable to failure criteria of rocks [*Zoback*, 2007; *Fjaer et al.*, 2008]. The effective stress (σ') is written as:

$$\sigma' = \sigma - P_f \tag{3.20}$$

where the pore pressure *(P_f)* asserts an opposing force to compressive stresses (σ). The effective stresses can easily be applied to the discussion of rock failure. In relation to Mohr diagrams, pore pressure shifts the Mohr circles to the left, bringing them closer to the failure envelope, and therefore decreasing the shear and normal stress needed to cause failure.

Triaxial tests can be performed under drained and undrained conditions (definitions follow Paterson [1978]) with the introduction of a pumping system to apply pore pressure. Drained tests maintain a constant pore pressure by allowing the saturating pore fluid to exit the system as compressive stress is introduced. In undrained tests, a pore pressure is set and then isolated from the system during experimental deformation.

For the triaxial experiments described in Chapter 5, approximately half of the tested Indiana limestone samples were saturated with viscous paraffin wax. The laboratory setup did not include equipment to introduce or maintain a pore pressure. Pore pressure effects on sample strength are then related to the build up of pore pressure resulting from insufficient permeability to react to changes in porosity during experimental deformation at some critical strain rate [*Brace and Martin*, 1968]. If a sample is subjected to pore pressure and has overall increased porosity during deformation, relative rock strengthening occurs, termed dilatancy hardening [*Paterson*, 1978]. In the case of experiments with no initial pore pressure, an increase in porosity during compression would not cause pore pressure effects influencing rock strength.

3.4.5 Tensile Failure

Rock failure under tensile conditions is generally less studied than rock under compression. One reason for this is rock at depth in Earth's crust is very rarely under tensile stress [*Zoback*, 2007]. Many sedimentary rocks have tensile stress of approximately zero, or very low values because of pre-existing flaws aligned perpendicularly to the applied tensile stress [*Fjaer et al.*, 2008]. Tensile strength for isotropic rocks is reported as:

$$\sigma_3 = -T_0 \tag{3.21}$$

The use of Brazilian tensile strength (BTS) tests to determine a brittle material's tensile strength has a history dating to the 1940's reviewed by Li and Wong [2013]. The BTS testing theory assumes an isotropic, homogenous and linear elastic material [*Mellor and Hawkes*, 1971]. The basic configuration is the application of a diametrical load to a cylinder (or disk), as in Fig. 3.3. BTS tests are an indirect tensile strength measurement method, as the stress state is inhomogeneous and tensile in near the center of the disk. The BTS test is popular because of relative ease of sample preparation and testing procedure, along with more realistic extensional failure resulting from compression akin to in situ crustal conditions [*Aydin and Basu*, 2006]. The tensile stress at failure (σ_t) is given by [*ASTM D3967-08*, 2008]:

$$\sigma_t = \frac{2P_a}{\pi D t} \tag{3.22}$$

where P_a, D, and t, are the applied load, disk diameter, and disk thickness, respectively. A set of curved jaws or cushions are recommended for reducing the stress through distribution at the load application point. Principal stresses act perpendicular (σ_Θ) and parallel (σ_r) to diametrical loading [*Mellor and Hawkes*, 1971]. Hondros [1959] developed a solution for the stress state of a disk and cylinder under BTS conditions where the load is distributed over a finite arc:

$$\sigma_\theta = \frac{P_a}{\pi R t \alpha}\left\{\frac{[1-(r/R)^2]\sin 2\alpha}{1-2(r/R)^2\cos 2\alpha+(r/R)^4} - \tan^{-1}\left[\frac{1+(r/R)^2}{1-(r/R)^2}\tan 2\alpha\right]\right\} \tag{3.23a}$$

$$\sigma_r = -\frac{P_a}{\pi R t \alpha}\left\{\frac{[1-(r/R)^2]\sin 2\alpha}{1-2(r/R)^2\cos 2\alpha+(r/R)^4} + \tan^{-1}\left[\frac{1+(r/R)^2}{1-(r/R)^2}\right]\tan 2\alpha\right\} \tag{3.23b}$$

where P_a is again the applied load, R is the disk radius, r is the distance from the disk center, t is the disk thickness and 2α represents the angular distance of the load distribution. Following Mellor and Hawkes [*Mellor and Hawkes*, 1971], at the center of the disk these equations can be shown to reduce to:

$$\sigma_\theta = \frac{P_a}{\pi R t}\left(\frac{\sin 2\alpha}{\alpha} - 1\right) \approx \frac{P_a}{\pi R t} \tag{3.24a}$$

$$\sigma_r = -\frac{P_a}{\pi R t}\left(\frac{\sin 2\alpha}{\alpha} + 1\right) \approx -\frac{3P_a}{\pi R t} \tag{3.24b}$$

The approximated final form of Eqn. 3.24a is equivalent to σ_t of Eqn. 3.22. The resultant error from loading force application over a 15° arc is approximately 2% [*Mellor and Hawkes*, 1971]. Fairhurst [1964] first recognized that reported BTS values typically underestimate the tensile strength if failure doesn't emanate from the disk center as required for test validity [*Colback*, 1966]. Perras and Diedrichs [2014] found the direct tensile strength results in sedimentary rocks are approximately 70% of the value obtained from BTS testing.

3.5 Summary

In this chapter, a background of rock mechanics theory related to the geomechanical tests employed in this study was presented. The basics of stress in the Earth's crust and Anderson's faulting theory were reviewed. The context then shifted to laboratory based rock strength testing where, test types, sample stress and strain, rock failure in compression and tension, and pore pressure effects were discussed. The next chapter presents details of sample preparations and testing procedures.

4. Laboratory Experiments

The purpose of this chapter is to describe in detail the preparations and procedures for rock strength experiments performed in the laboratory. Both compressive and tensile strength tests were carried out on Indiana Limestone samples. Only tensile strength tests were performed on Grosmont formation samples. The procedures of preparing the samples and performing experiments were guided by the American Society of Testing and Materials (ASTM) international standards. A table of sample specifications is presented in Appendix A.

4.1 Compressive Strength Tests

4.1.1 Sample Preparation

Before describing the experimental procedure, sample preparation for compressive strength tests must be discussed. ASTM standards [*ASTM D4543*, 2008] specify the procedure for preparing laboratory cylindrical core test specimens from blocks of rock and drill core. The Indiana limestone (described in Chapter 5) used in the rock strength experiments was purchased in blocks (from Kocurek Industries) with dimensions of approximately 30cm x 30cm x 10cm (Fig. 4.1). The blocks were then cut with a diamond rock saw (Fig. 4.2) to a length that allowed for right cylindrical rock cores with a slightly larger than 2:1 length to diameter ratio to be drilled. The 2:1 ratio is specified within the ASTM guidelines.

These cut blocks of Indiana Limestone were cored using a thin-walled diamond drill bit mounted on a drill press (Fig. 4.3). After coring, the circumferential surface was generally smooth and free of abrupt irregularities and therefore no further finishing was required. Then, the ends were machined flat using a surface grinder (Fig. 4.4) to within the tolerances (Table 2) specified by the ASTM [*ASTM D4543*, 2008].

Table 2 ASTM 4543 sample preparation tolerances

Item	**Standard**
Support surface	Not to depart from plane by more than 0.0013 mm (0.0005 in)
Dial gauge	Sensitive to 0.002 mm (0.0001 in)
Specimen L/D	Between 2.0 and 2.5
Specimen diameter	No less than 47 mm (1-7/8 in)
Specimen sides	Straight to within 0.50 mm (0.020 in)
Specimen ends	Less than 25 μm (0.001 in) deviation from best fit
Specimen ends	Parallel to within 0.25°

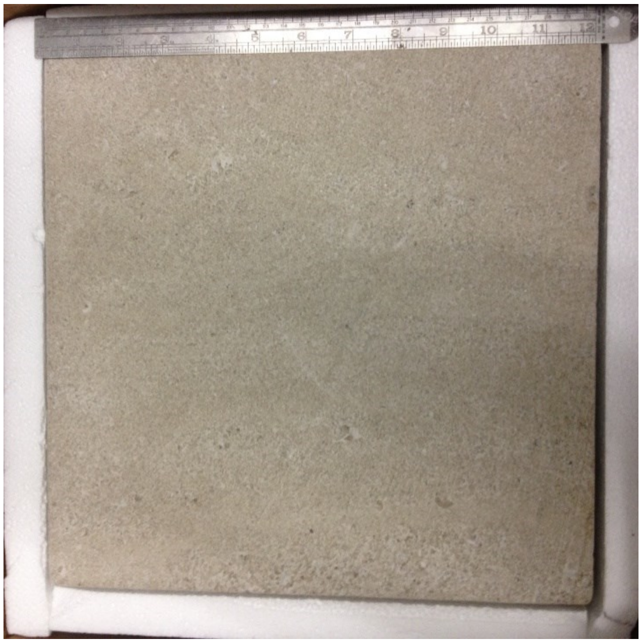

Figure 4.1 Top view of one raw block of Indiana Limestone used for rock strength experiments. A ruler is shown for scale.

Figure 4.2 Image of the diamond rock saw used to cut Indiana limestone blocks. The blocks are fed into the saw by a manually movable platform. Water is pumped onto the blade to wash away cuttings and cool the blade and rock.

Figure 4.3 Photo of the drill press and example of a thin walled drill bit used to cut core samples. Water is pumped through a water swivel adapter, to cool the diamond core barrel and wash cuttings away from the rock surface. The rock blocks are clamped securely to a ½” thick piece of plywood on the drill table to prevent unwanted motion.

Figure 4.4 Photo of the surface grinder used to machine the ends of the cored specimens. Specially machined V-blocks are used to hold the sample in place on the flat, magnetic surface. The surface grinder operates manually and like the coring process, a pump provides water to the surface of the grinding wheel acting to cool and wash away cuttings.

The flatness was measured by placing the specimen upright on a machined flat steel support surface under a displacement dial gauge with 25 µm accuracy (Fig. 4.5). The dial gauge pin has a rounded contact tip and moves freely (in most cases) along the surface of the specimen. Maximum and minimum values are noted while moving the pin across 3 different diameters on each end of the specimen. Each specimen end was ground flat so the largest difference across any measured diameter was less than 25 µm (0.001 in). This also ensures the ends are parallel to within 0.25°. The dial gauge deflects abnormally when the pin encounters a large pore space on the sample surface. In some cases, the measurement falls out of the 25 µm ASTM standard, but guidelines state to ignore these occurrences. Often, the surface pore spaces are small enough and the pin glides smoothly along the surface. ASTM standards [*ASTM D4543*, 2008] state dimensions and tolerances are particularly important for determining rock properties of intact strong rocks, referring to rocks with peak strengths greater than 50 MPa. In this study, 47.3MPa was the largest stress recorded during uniaxial compressive strength (UCS) testing on Indiana limestone samples.

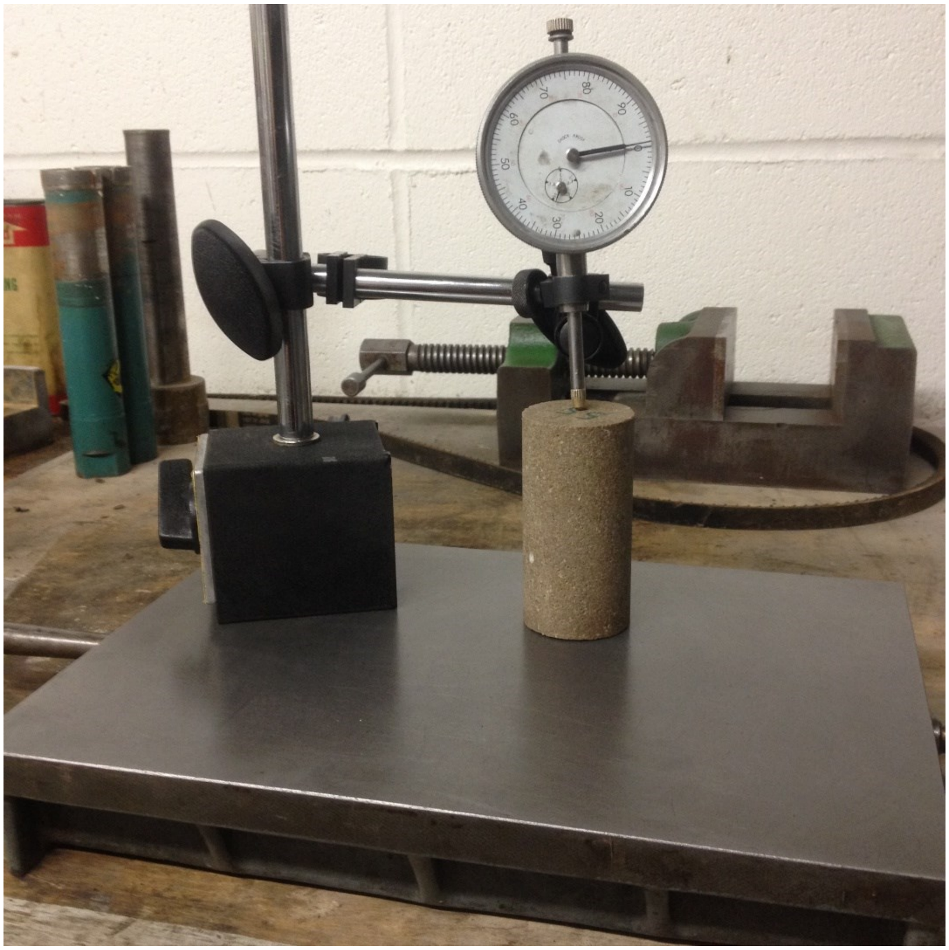

Figure 4.5 Photo of the apparatus used for determining the flatness of the cylindrical end surfaces. The displacement gauge is mounted on an adjustable stand with magnetic base. The base sits on top of the flat steel support surface.

After completion of coring and planing, the sample was placed in a vacuum oven at approximately 90°C and dried for 24 hours. The sample was then removed from the oven and cooled in a desiccator jar under vacuum for an additional 12 hours. All samples were tested at room temperature of 23.5°C.

Each sample's mass and dimensions (length and diameter) were then measured. A digital caliper (0.01 mm accuracy) was used to measure the diameter by taking the average of a pair of measurements, made at right angles to each other, at the approximate middle of the sample length. Although specimens were cored using the same diamond drill bit, small variances in sample diameter were measured. Specimen length was also determined with the digital caliper by placing the caliper in the middle of both ends, performing the measurement at least twice and taking the average value. The cross-sectional area and volume of the specimen was calculated using the length and diameter measurements. The specimen mass was recorded using a digital scale with 0.1-gram accuracy.

Approximately half of the samples were saturated with paraffin wax to simulate reservoir conditions of the bitumen saturated Grosmont formation. Prior to saturating the samples, the porosities (φ) were estimated using helium pycnometry (discussed in detail in Chapter 2). The porosity value is essential to estimating the sample saturation. A block of wax was cut, then dimensions were measured with a digital caliper to calculate volume (V), and mass (m) was measured with a digital scale. The measured dimensions were somewhat difficult to attain because of the softness of the wax and are estimated to 0.1 mm. The density (ρ) of the wax was calculated based on the measurements (m/V). Together in an oven-safe dish, Indiana limestone specimens and wax went in the oven at 90°C under vacuum. The wax melts at approximately 60°C causing the samples to be immersed in the liquid wax. Samples remained in the oven for 24 hours, followed by removal and another 24-hour cooling period. The saturation (S) was calculated from the estimated sample porosity and wax density as follows:

$$S = \frac{M_{meas} - M_{dry}}{M_{exp} - M_{dry}} \tag{4.1}$$

where M_{exp} denotes the theoretical mass of a 100% wax-saturated sample, M_{meas} is the actual measured mass of the sample after saturation, and M_{dry} is the measured dry mass of the sample. M_{exp} was calculated, assuming all available pore space was wax filled, by following equation:

$$M_{exp} = (\varphi \times V \times \rho) + M_{dry} \tag{4.2}$$

where φ is sample porosity, V is envelope volume and ρ is paraffin wax density.

When samples were pulled from the liquid wax and allowed to cool, a small amount of wax ran out of the surface area pores, so 100% saturation values were not expected. An attempt was made to allow the sample to solidify in the wax, but removing the wax without compromising the sample proved difficult. Recorded saturation values (Appendix A) of over 85% are satisfactory for the purposes of this study. Oil saturation values from the production zones average 82% and 79% for the Grosmont C and D reservoirs respectively [*Russel-Houston and Gray*, 2014], although in those studies it is not stated whether the remainder of the pore space is saturated with water or gas.

4.1.2 Strain Gauges

After samples cooled, strain gauges (Omega SGD-10/350-LY41, 350 ohms) were applied to measure the axial and lateral (or circumferential) strains exhibited under load during compressive strength tests.

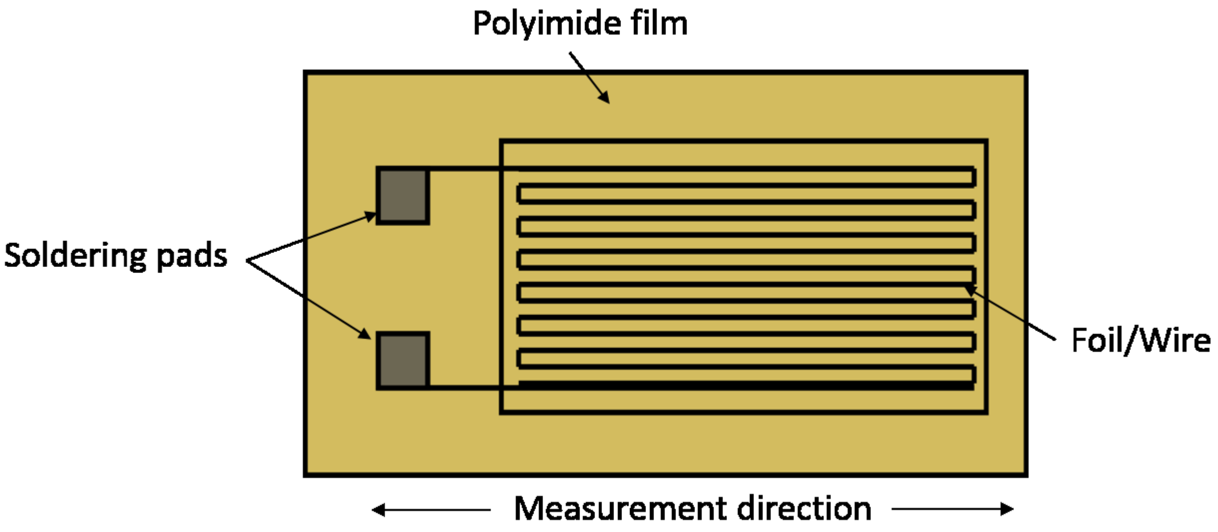

Figure 4.6 Schematic of strain gauge.

The strain gauge shown above (Fig. 4.6) contains a single continuous wire or foil that deforms with the sample under applied load, assuming the gauge is properly bonded to the sample surface. The foil is composed of the copper-nickel alloy constantan, and is sealed in a flexible polyimide film. The strain is measured parallel to the long edge of the gauge (Fig. 4.6). As the wire stretches or shortens the effective length and therefore electrical resistance changes as:

$$R = \frac{\rho_r \times L}{A} \tag{4.3}$$

where R is resistance, ρ_r is resistivity, a property of the wire, L is length and A is the cross-sectional area. The change in resistance is related to strain by the gauge factor:

$$GF = \frac{\Delta R/R}{\varepsilon} \tag{4.4}$$

where GF, ΔR, R and ε are the gauge factor (provided by the manufacturer), change in resistance, resistance and linear strain respectively. The gauge factor is determined experimentally by the manufacturer on a sample for a given production run and relates the change in resistance of the material to the mechanical strain. The strain gauges used for these experiments have a nominal resistance of 350 Ω ± 0.35% and gauge factor of 2.13 ± 0.11. The change in resistance (ΔR) when the gauge is under strain is a significantly smaller value (approximately 5 orders of magnitude) and poses a problem for accurate measurement. An unbalanced Wheatstone bridge circuit (Fig. 4.7) is a popular method of addressing such a measurement problem.

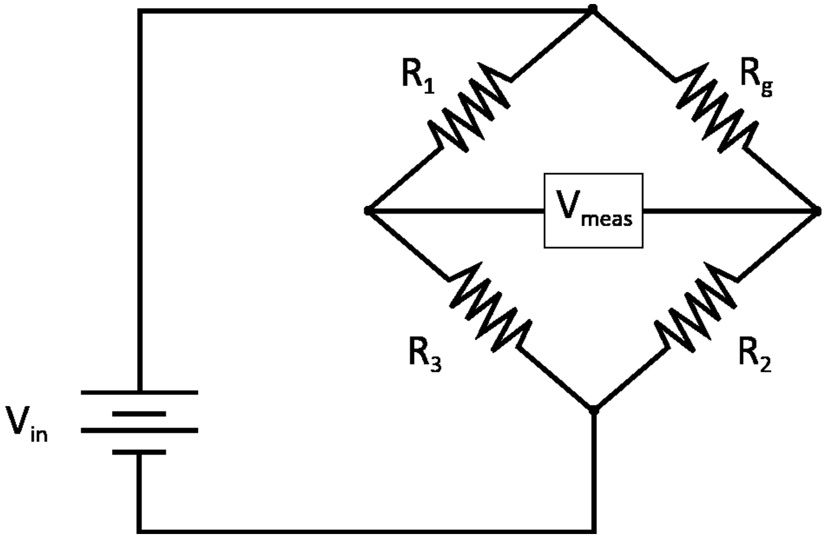

Figure 4.7 Diagram of a Wheatstone bridge circuit. Also known as a Quarter bridge.

The Wheatstone bridge circuit relates the change in resistance to a measurable change in voltage which varies about 0 Volts.

$$V_{meas} = V_{in}\left[\frac{R_2}{R_2 + R_g} - \frac{R_3}{R_1 + R_3}\right] \tag{4.5}$$

where R_g is the resistance of the strain gauge and R_1, R_2, and R_3 are constant resistances, in this case produced by 350 Ω precision resistors (Vishay Group, 0.01% error). The bridge is activated by a constant input voltage (from NI SCB-68) of 5V (V_{in}), and the output response voltage (V_{meas}) is measured (NI PXI-6229, 48.8 µV sensitivity) across the middle of the two sets of resistors (one of the sets contains the strain gauge, R_g). The value of R_g can be thought of as $R+\Delta R$ when the sample is being strained because under unstrained conditions the strain gauge has a resistance of 350 ohms like the other resistors in the circuit. Theoretically, if all the resistors including the contact lines were perfectly equal, the system will report a value of 0V for unstrained conditions, although practically the voltage measured is a very small number due to unavoidable differences in resistance along the arms of the bridge. To account for the non-zero voltage measured in the unstrained condition, the variable V_r is introduced; where V_r is the difference in the ratio of V_{meas} to V_{in} from strained to unstrained conditions:

$$V_r = \left[\frac{V_{meas}}{V_{in}}\right]_{strained} - \left[\frac{V_{meas}}{V_{in}}\right]_{unstrained} \tag{4.6}$$

Substituting R_g for $R+\Delta R$ and making use of equation (4.4) the strain calculated from the measured voltage is then straightforwardly:

$$\varepsilon = \frac{-4V_r}{GF(1+2V_r)} \tag{4.7}$$

The strain gauges were carefully placed in the center of the specimen and bonded to the surface with adhesive (Loctite 496). The glue cured for 24 hours before wires were soldered onto the strain gauge pads. The wires transmit data from the gauges, through a 16-bit data acquisition system (NI SCB-68, NI PXI-6229, NI PXI-1033) sampled at 20 Hz, into the digital format recorded by a Labview™ program.

During compressional strength testing problems were encountered with the strain gauges. The strain gauges often failed at confining pressures above 10 MPa during triaxial testing. It was thought that the pore spaces on the specimen surface were causing a break in the strain gauge wire when pressure was applied. To remedy this, a layer of glue was applied to the sample surface filling the other pore spaces (Fig. 4.8). After curing, the glued area was sanded smooth and strain gauges were applied. This also helps to ensure the gauges have a good bond with the sample surface. Fine sanding was performed prior to gauge application on all wax-saturated samples enabling better gauge to sample adhesion. The strain gauges are placed in the middle of the sample and while this is a point measurement of the strain at that location, it is expected that the stress is most uniform at the middle of the sample and this location best represents the sample strain. Strain gauge measurements are also sensitive to pressure perpendicular to the gauge grid and temperature. The pressure effect is approximately 0.55 ± 0.2 x 10^{-6} MPa^{-1} [*Jansen*, 1997].

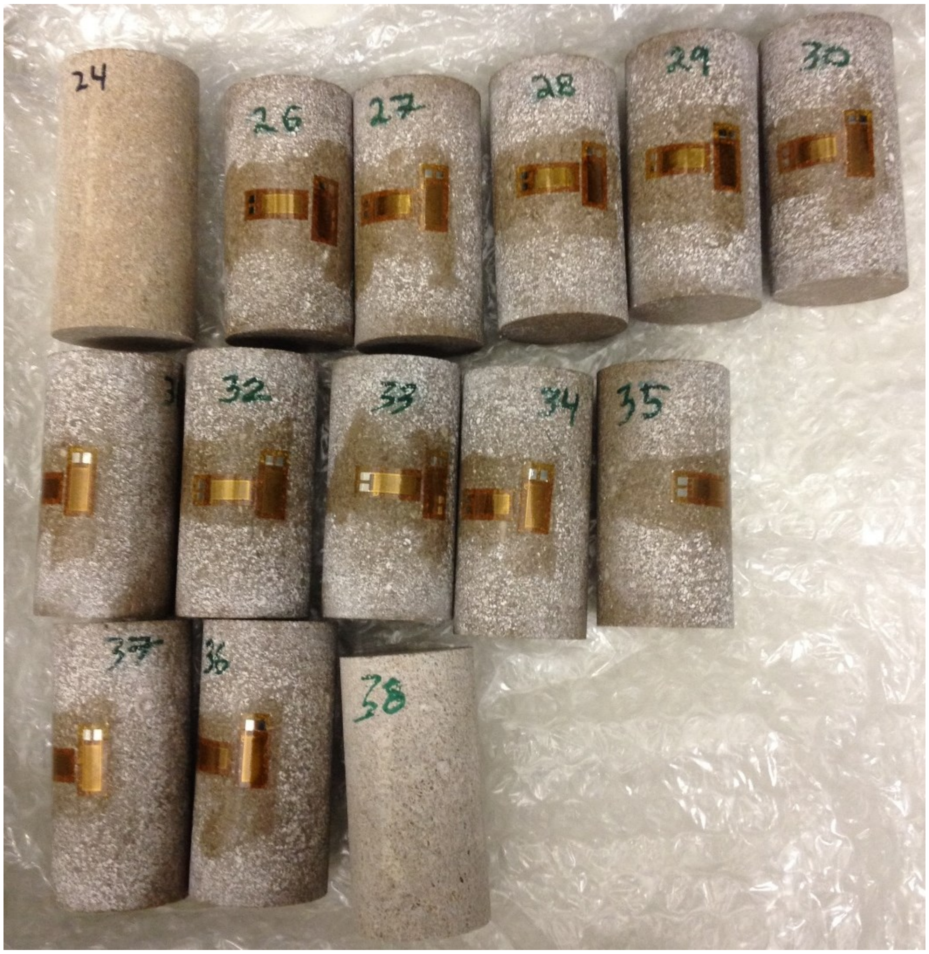

Figure 4.8 Photo of prepared samples with strain gauges attached. The glue filling the outer surface pores is the darker area under strain gauges.

4.1.3 Experimental Apparatus

The compressive strength tests performed on Indiana Limestone included UCS tests and a series of triaxial tests at a range of confining pressures from 1MPa to 20 MPa. The compressive strength tests followed ASTM standards [*ASTM D7012-14e1*, 2014] when possible. The description of the testing equipment and procedures begins by describing the UCS test and then noting additional considerations for triaxial tests.

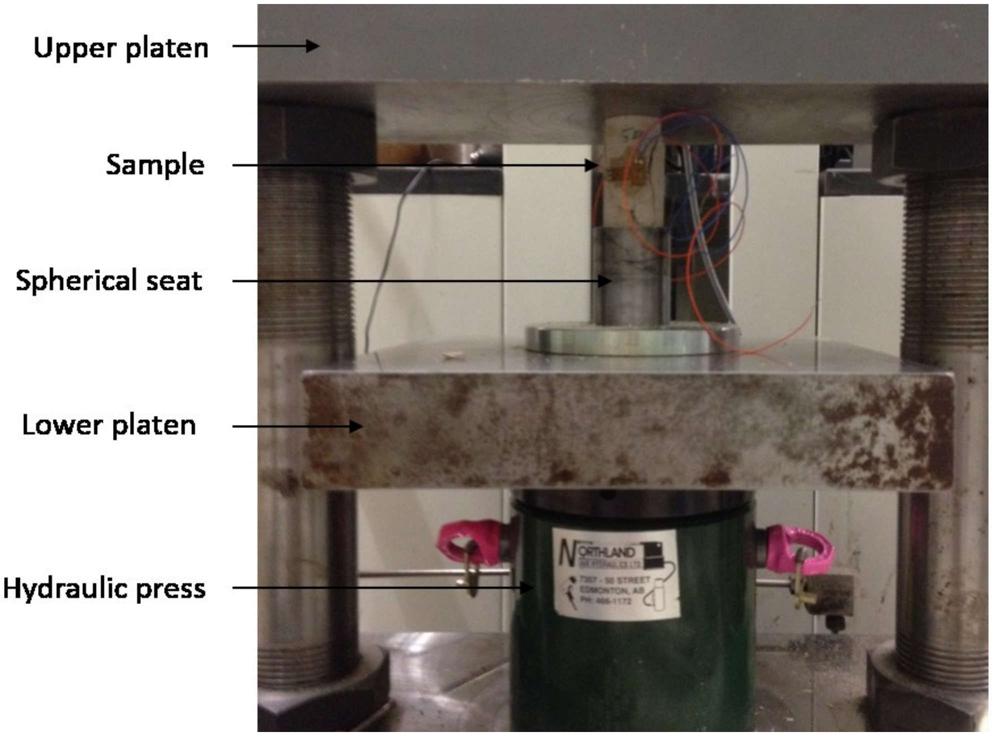

Figure 4.9 Photo of uniaxial compressive strength experimental set-up.

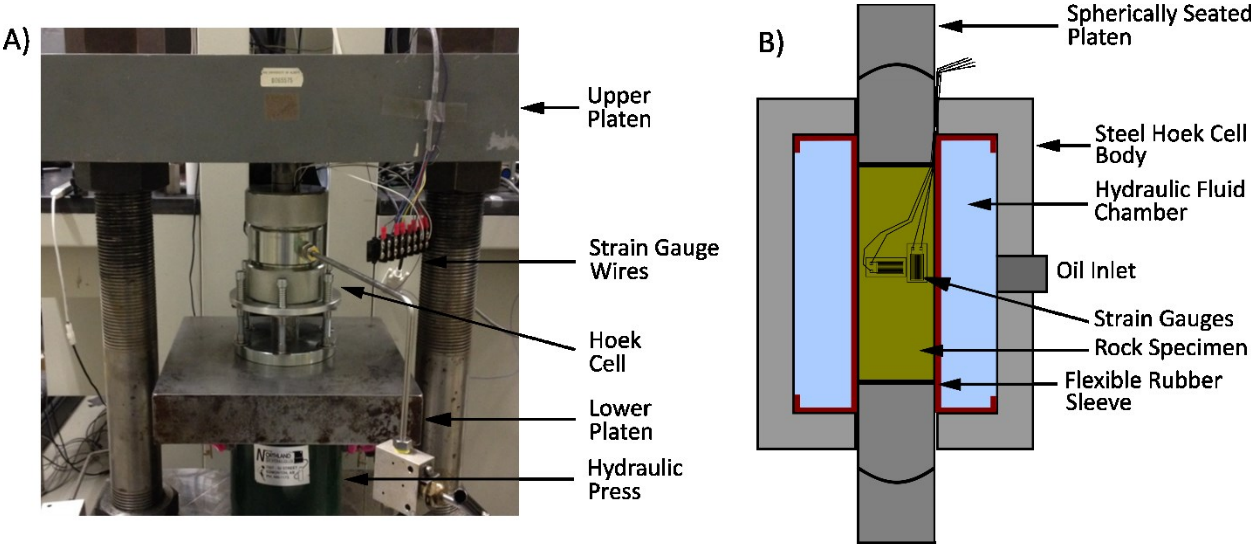

Figure 4.10 A) Photo of triaxial compressive strength experimental set-up. B) Schematic of Hoek cell.

Two hand pumps control the axial load applied by the hydraulic press (Simplex RLN 1002) (Fig. 4.9). The lab is not equipped with a servo-controlled machine and therefore uniformly increasing the axial stress is mainly reliant on operator skill. The load applied by the axial ram of the hydraulic press is measured by a pressure transducer (Wika Model A-10), outputting a voltage that is converted to stress (MPa) acting upon the sample through knowledge of axial ram and sample dimensions.

The confining system used for the triaxial tests is a Hoek cell shown in Fig 4.10. The sample is centered within the flexible rubber sleeve of the Hoek cell. The sample position within the rubber sleeve is modified by adjusting the Hoek cell stand legs. A single hand pump moves hydraulic fluid into the Hoek cell chamber setting the confining pressure. In some experiments the confining pressure appeared to decrease slightly with time and the pump needed to be operated intermittently to maintain (within 5%) the set confining pressure. A small crack in a joint connecting two sections of hydraulic hose caused the pressure drop and was fixed. A second pressure transducer (same model external pressure transducer as the hydraulic press) measures the applied confining pressure. This pressure is also recorded for the experiment duration.

The bottom platen arrangement consists of a square flat platen resting on top of the hydraulic press piston (10.95 cm diameter); above it sits a spherically seated steel platen with a 50.8 mm (2 in) diameter for UCS tests and a 38.1 mm (1.5 in) diameter (fits Hoek cell) for triaxial tests. A single rigid top platen (Fig. 4.9) is used in UCS testing, while an additional 1.5” diameter spherically seated platen identical to the bottom platen, is used to perform triaxial tests. The spherically seated platens in both tests allow the sample to move through very small angles to compensate for any error in the flatness of specimen ends (although much effort is taken to prevent this as described in 4.1.1), or misalignment of the apparatus, specifically the top and bottom rigid platens. The rigid top platen is vertically adjusted one side at a time, using a wrench to turn the large nuts above and below the platen. This adjustment is performed for every experiment to accommodate samples of varying length and changes in the apparatus from UCS to triaxial tests. The alignment between the top and bottom rigid platens is measured using a large level. Platen surfaces are wiped clean with an ethanol solution and a fine towel before setting the testing configuration.

The load frame stiffness in relation to the tested rock sample is an important system parameter. If the frame is relatively soft rock failure cannot be controlled. The stiffness of the frame (k_m) is found by:

$$k_m = \left[\sum_{i=1}^{N} \frac{1}{k_i}\right]^{-1} \tag{4.8}$$

where N is the number of frame components, and k_i is the stiffness of each component calculated by:

$$k = \frac{AE}{L} \tag{4.9}$$

where A is the cross-sectional area, E is the material's Young's modulus, and L is the length [*Hudson et al.*, 1972]. Considering the dimensions and material properties of platens and support rods, the estimated load frame stiffness is ~6.0 x 10^3 kN/cm. The approximate Indiana limestone sample stiffness (k_s) is 4.1 x 10^3 kN/cm given by:

$$k_s = \frac{\pi}{4} DE \left(\frac{L}{D}\right)^{-1} \tag{4.10}$$

where D is specimen diameter and L is specimen length. The frame stiffness is greater than the rock stiffness in this instance and should not impact measurements. Sample displacement is an uncontrolled variable with the current laboratory equipment, therefore the entire stress-strain response (including the post-failure region) cannot be observed.

Safety measures should not be overlooked in any laboratory testing procedure. For the UCS and Brazilian tensile tests, a wooden shield was constructed to fit over the load frame. This shielding system provides protection from flying pieces of failed rock specimen that could cause injury or damage to other equipment, such as the camera. The wooden shield is open in the front and a transparent plastic plate is clamped to the bottom rigid platen. The transparent plate enables video recording of both UCS and Brazilian tensile tests. Steel lines and connections, appropriately rated to handle the typical hydraulic pressures, are part of the system design. The system also includes multiple isolation valves along the steel lines to limit the amount of fluid lost in case of a leak. The hand pumps have hydraulic lines extending ~4 m away from the load cell providing a distance buffer from failing samples. Personal protective equipment including safety goggles, closed toe shoes, lab coat and rubber gloves is also mandated.

4.1.4 Procedure

For UCS tests, the specimen is placed in the center of the load frame on top of the spherically seated platen as shown in Fig. 4.9. The top and bottom platens are aligned with a level to ensure they are parallel and can be checked with a dial gauge like the one used in sample preparation. All safety shielding is positioned. The wires soldered to the strain gauge are connected to the system. A camera (Canon 7D, 60 fps) is placed outside of the transparent plastic safety plate to record video of the sample during experimental testing. The axial load is applied to the sample through the hydraulic press by operating the hand pumps alternately, so just as the stroke of one pump is complete, the other starts; increasing the axial stress as smoothly and continuously as possible. The axial stress and resulting deformation is continuously recorded with the Labview™ program. Uniform pressurization rates of approximately 0.7 MPa/s were maintained until the specimen ultimately fails. The failure of the rock specimen must occur within 2 to 15 minutes per ASTM standards [*ASTM D7012-14e1*, 2014].

Triaxial strength tests require additional steps related to setting a confining pressure. The specimen is placed in the Hoek cell on top of a spherically seated platen. An additional spherically seated platen is placed on top of the specimen. The alignment of the Hoek cell with top and bottom platens is checked with levels and if necessary the legs on the Hoek cell frame are adjusted to align with platens. The strain gauge wires are attached to the digital acquisition system. A small axial load is applied to ensure sample and spherical platens are seated properly before the confining pressure is set. The confining pressure is set to the desired pressure by operating the Hoek cell hand pump. The sample is then placed under axial load by operating the hand pumps that control the hydraulic press and the applied stress and resulting deformation is continuously recorded digitally by the Labview™ program. The axial load is continuously increased until sample failure at approximately the same pressurization rate as the UCS tests.

4.2 Tensile Strength Tests

4.2.1 Sample Preparation

ASTM standard D3967-08 [2008] guided the tensile strength tests. It specifies both sample preparation and testing procedures for splitting tensile strength measurements of intact rock core specimens. Brazilian tensile strength tests were performed on dry and wax-saturated Indiana limestone samples plus dry and bitumen-saturated Grosmont formation samples. Only one bitumen-saturated Grosmont formation sample was tested. Most were tested dry, as the bitumen was previously extracted by the Soxhlet method to perform ultrasonic velocity experiments [*Rabbani et al.*, 2017].

For Indiana limestone tests, a core sample was prepared, as described for compressive strength tests (4.1.1). The Grosmont samples came as drill core recovered from the borehole. The core size was originally (~87 mm) but it is re-cored to the desired 50.8 mm (2 in) diameter for ultrasonic experiments [*Ong et al.*, 2016].

The core samples of Indiana limestone and Grosmont formation are cut into disks at a right angle to the longitudinal axis. A diamond bladed rock saw with a clamping mechanism is used to make the right angle cut. Often, the disks cut using the saw are parallel and no grinding is required to the ends. The thickness to diameter ratio of the disks must be between 0.2 and 0.75 [*ASTM D3967-08*, 2008].

The thickness and diameter are measured with a digital caliper. A minimum of three thickness measurements, with one in the center of the disk, are taken and averaged for the reported thickness value. Similarly, the diameter is measured 3 times and averaged, including one measurement across the anticipated loading diameter. The sample mass was determined with a digital scale.

Then disks are oven dried under vacuum for a minimum of 24 hours at 70°C. All tensile tests were performed at room temperature of 23°C.

All the Grosmont formation and four of the Indiana limestone disks had a strain gauge applied to on their face. The strain gauge was placed in the center of the disk perpendicular to the diametrical load, to measure the strain under tension.

Samples were marked on the edges of the face, across the diameter of intended loading. The marks help with sample alignment and post-testing failure path analysis.

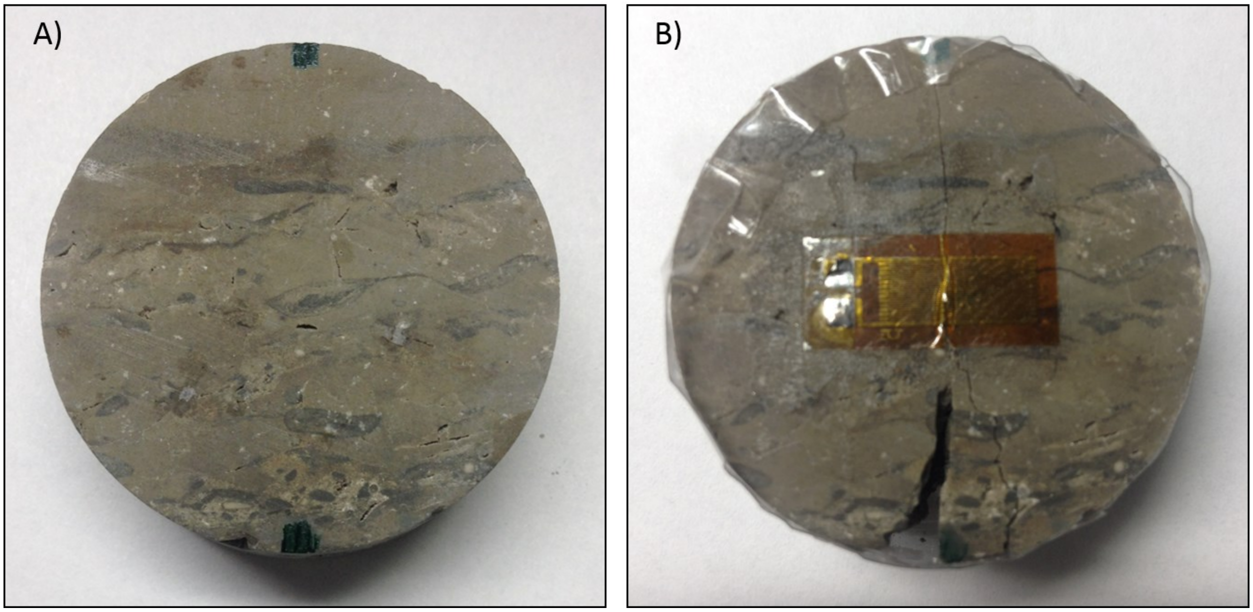

Figure 4.11 Photo of prepared Grosmont formation (sample A1) Brazilian disk test specimen. A) Pre-testing. B) Post-testing.

4.2.2 Experimental Apparatus

The same load frame, hydraulic press and spherically seated bottom platen was used in UCS testing and Brazilian tensile strength measurements (Fig. 4.12). The spherical seat was lubricated to ensure unrestricted motion.

Plywood cushions 1/4'" thick are placed between the platens and the specimen surface to distribute stress concentrations over an arc at the contact points with the platens. The cushions help prevent contact crushing and are common in Brazilian measurements [*Perras and Diederichs*, 2014]. The plywood strips are cut so approximately 15° of arc length (~ 4mm) contact the disk.

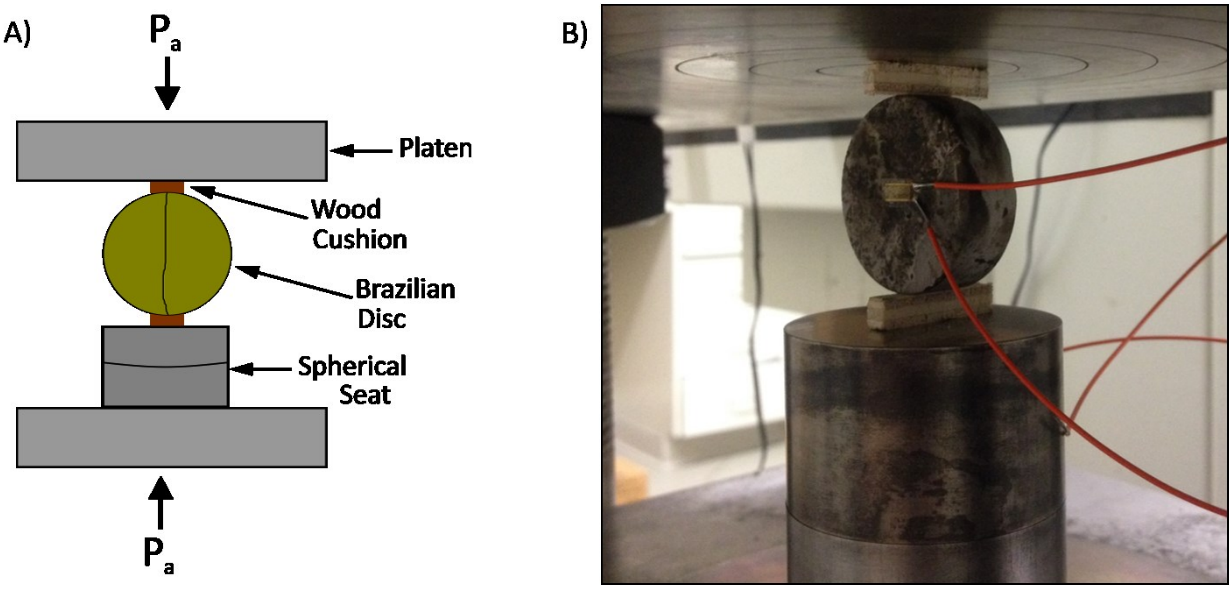

Figure 4.12 Schematic A) and photo B) of Brazilian tensile strength laboratory testing set-up.

4.2.3 Procedure

The specimen is rested on a plywood cushion, centered on the spherically seated platen. The top plywood cushion is positioned on the specimen and the top platen is lowered into contact with it. The top platen provides a light force and prevents the disk from falling out of position. Without applying the small force of the top platen, it is very difficult to align the specimen and balance it on the bottom cushion. This is especially true when a strain gauge is mounted on the face of the specimen, as the connecting wires cause unbalance and the specimen falls off the bottom cushion.

The disk alignment with wood cushions is adjusted using the diametrical marks placed on the disk during sample preparation. If using a strain gauge, the wires soldered to the gauge are connected to the system. The same safety shielding accessories used in the compressional strength tests are put in place and the camera is set in front of the transparent plate to record video of the ensuing test.

Once alignment of specimen has been verified, a continuously increasing compressive load is applied to the specimen until failure occurs. The loading rate is kept as constant as possible, considering the experimental apparatus (wood cushions deform before rock samples). Failure should occur within 1 to 10 minutes per ASTM standard [*ASTM D3967-08*, 2008].

4.3 System Calibration

Before testing rock samples, the system was calibrated to a cylindrical sample of 6061 T6 aluminum. From compressive testing, the estimated Young's modulus for the aluminum sample was 69.0 GPa. The Young's modulus was found by taking the slope of the linear portion (average modulus) of the axial stress-strain curve shown below (Fig. 4.13). More detail on the determination of elastic moduli will follow in Chapter 5. 6061 T6 aluminum has a Young's modulus of 70.1 GPa [*Herbert et al.*, 2001], giving confidence in the experimental system. The value was not expected to match perfectly, but closely, as the aluminum sample has been compressed many times in the past.

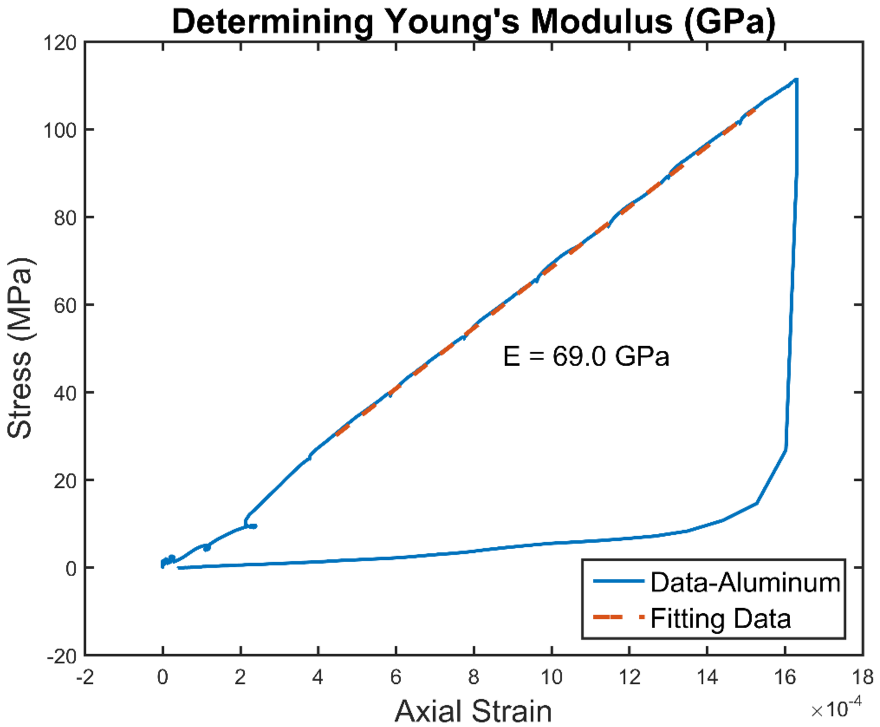

Figure 4.13 Axial stress-strain curve of aluminum sample and fitted data to estimate Young's Modulus.

5. Indiana Limestone Geomechanical Testing Results

ABSTRACT:

Indiana Limestone, a readily available carbonate rock, was selected for geomechanical testing as an analogue to Alberta’s bitumen-saturated, Devonian-aged Grosmont formation. To study the effects of a highly viscous material occupying the pore space, both completely dry samples and samples saturated with paraffin wax were tested. Compressive strength tests including Unconfined Compressive Strength (UCS) and Triaxial strength tests, employing confining pressures of up to 20 MPa, were completed on 39 cylindrical Indiana Limestone samples. Brazilian tensile testing was also completed on 10 dry samples and 10 wax-saturated samples. The experimental results are presented, and show that peak sample strength tested under compressive conditions does not change significantly with the addition of paraffin wax. However, there appears to be subtle variation in elastic properties and failure mode on the macro and microscopic scales, when comparing dry and wax-saturated specimens. The Brazilian tensile strength data also show some discrepancy and suggest the wax-saturated samples have a greater average tensile strength than the dry tested samples.

5.1 Introduction

The motivation for this work is borne out of an interest in the geomechanical properties of the Grosmont Formation, located in northern Alberta, Canada. The Grosmont Formation is an important carbonate-hosted bitumen reservoir for future energy production in Alberta. The AER [*Alberta Energy Regulator*, 2015] estimates the Grosmont contains 64.5 billion cubic meters of crude bitumen in place.

Crude bitumen differs from conventional oil plays as it is highly viscous and will not flow under in situ natural conditions particularly at the temperatures of only ~12°C in the region. Depending on reservoir depth, some crude bitumen, such as the oil sands in the Fort McMurray area of Alberta, are surface mineable. Otherwise in-situ production techniques are required to stimulate the bitumen by essentially reducing its viscosity. Mohebati et al. [2014] provides a summary of Grosmont pilot projects, starting in the mid 1970’s and describes recent attempts at applying thermal bitumen recovery techniques to the Grosmont. Production technologies and techniques are well-developed for oil sands, as is the study of the reservoir geomechanics; but to our knowledge little work has been completed regarding the geomechanics of bitumen saturated carbonates. Here, we describe a set of laboratory experiments to investigate the role a highly viscous fluid plays on the strength and elastic properties of a carbonate rock.

There are several reasons to investigate a reservoir's geomechanical properties particularly when production techniques, such as steam assisted gravity drainage (SAGD), perturb the stress field in a bitumen reservoir through the injection of steam. This process is complicated and is controlled by many variables such as pore pressure variations, thermal stresses, and chemical reactions. At the onset, however, knowledge of the basic rock strength can be used to reduce the risk of borehole failure and fractures propagating to surface resulting in high environmental impact and associated economic and social costs for the operator. Conversely, reservoir stimulation relies on the ability to cause fractures and thereby increase the effective permeability of the reservoir. Knowledge of geomechanics in those cases can lead to better planning of well bore placement and orientation, ultimately increasing recovery.

Performing a laboratory based investigation of a reservoir rock's mechanical properties is challenging principally because limited amounts of core are usually available for testing. It is also difficult to replicate in-situ conditions, as the highly viscous fluids contained in the rock mobilize at room temperature and pressure. The maximum amount of information needs to be derived from each available core sample and because of the destructive nature of mechanical measurements it is often the last test performed. For example, to perform ultrasonic measurements used in determining values of bulk modulus and velocity, the sample is drained of bitumen and cut to dimensions that enable a strong signal to be transmitted through the sample [*Rabbani et al.*, 2017]. Often the length is cut shorter than the standard 2:1 length to diameter ratio recommended for compressive strength tests. This jeopardizes the validity of a subsequent compressive strength test on such a sample.

The reservoir architecture of the Grosmont Formation is locally heterogenous characterized by pervasive fractures and karsting [*Putnam et al.*, 2016], making it problematic to collect meaningful and repeatable geomechanical measurements. Tested samples are generally prepared from the most competent sections of recovered core in each borehole, but often the reservoir section, of most interest, contains among the least competent cores. In some parts of the reservoir with the highest bitumen saturation, the bitumen bonds the particles together and if extracted the rock crumbles apart during sample preparation. All the concerns mentioned above can make reliable and useful results difficult to attain.

To compromise, Indiana limestone saturated with paraffin wax was chosen as an analogue to the bitumen-saturated Grosmont Formation rock. We realize that this is an imperfect comparison, but Indiana limestone does share a similar pore structure with parts of the Grosmont. Further, paraffin wax at room temperature simulates a quasi-solid bitumen at the relatively cold natural in situ reservoir temperatures of ~12°C. Though not ideal, because these materials share comparable properties with the formation in question, some value can be derived from the failure processes in these rocks.

The relative ease of procurement along with inherently uniform physical properties has made Indiana limestone the subject of many geotechnical testing programs. Studies have focused on the mechanical properties [*Robinson*, 1959; *Schwartz*, 1964; *Brace and Riley*, 1972; *Heard et al.*, 1974; *Amadei et al.*, 1984; *Cargill and Shakoor*, 1990; *Vajdova et al.*, 2004; *Lisabeth and Zhu*, 2015; *Walton et al.*, 2015], microstructure [*Hoagland et al.*, 1973; *Peck et al.*, 1985; *Zheng et al.*, 1989; *Ji et al.*, 2012; *Vajdova et al.*, 2012], fracture initiation, propagation and toughness [*Schmidt*, 1976; *Schmidt and Huddle*, 1977; *Ingraffea*, 1981; *Rinehart et al.*, 2015], and borehole breakouts [*Haimson and Herrick*, 1986; *Ewy and Cook*, 1990a, 1990b] in Indiana limestone.

The study of the effect of fluids, particularly water, on the strength of Indiana limestone is also well documented in the literature. Robinson [1959] saturated core samples with distilled water and applied a pore pressure, and observed the factor controlling failure to be the difference between pore and confining pressure. Heard et al. [1974] found water-weakening effects in both partially (~34% strength decrease) and fully saturated (~37% strength decrease) Indiana limestone samples under triaxial compression. Recently, Lisabeth [2015] studied the effect of water chemistry on strength, and demonstrated that equilibrated fluid has less effect in weakening compressed limestone samples. Using the ring method, Vutukuri [1974] determined the tensile strength of Indiana limestone saturated with various fluids and found as the surface tension and dielectric constant of the fluid increased, the tensile strength decreased. Hoaglund [1973] and Peck [1985] found the fracture energy decreased in wet samples using the double cantilever beam test.

Here, we describe an extensive suite of tests on both dry and wax-saturated Indiana limestone cores to investigate both compressive and tensile failure and the associated elastic properties. The tests include unconfined compressive strength (UCS), conventional triaxial, and the indirect Brazilian tensile strength measurement. We first provide a brief review of prior geomechanical studies using Indiana limestone as the sample material. We then follow with sample characterization and a description of the equipment and procedures used in this study to make measurements. Next, the collected rock strength data and ensuing discussion is presented. Finally, core photos and thin section observations provide further insight into the failure mode and characteristics. The data and failed samples from the test, will allow us in future to revisit some of the classic studies of rock failure at low pressure with emphasis on the transition from brittle to ductile failure.

5.2 Experimental Description

5.2.1 Sample Material

Indiana limestone, also known as Salem limestone or Bedford limestone, is a readily available carbonate rock sourced from the Bedford-Bloomington Indiana area. The fossiliferous limestone is Mississippian-aged and nearly monomineralic containing an average value of greater than 97% calcite, with the rest of the rock being composed of magnesite, silica and trace iron-oxides [*ILI*, 2007]. Grain sizes range from approximately 5 µm for cement to 300 µm for an average sized fossil [*Vajdova et al.*, 2004]. There are two groups of Indiana Limestone; the buff-colored variety was used in this study and contains higher porosity and permeability than its grey-colored counterpart [*ILI*, 2007]. Indiana Limestone is considered a freestone, meaning it is isotropic, without discernable bedding planes and therefore an easy rock to work with because, in principal, it can be cut, or cored in any direction without impacting experimental results. Its availability and homogenous properties have made it a popular choice for laboratory-based geomechanical investigations.

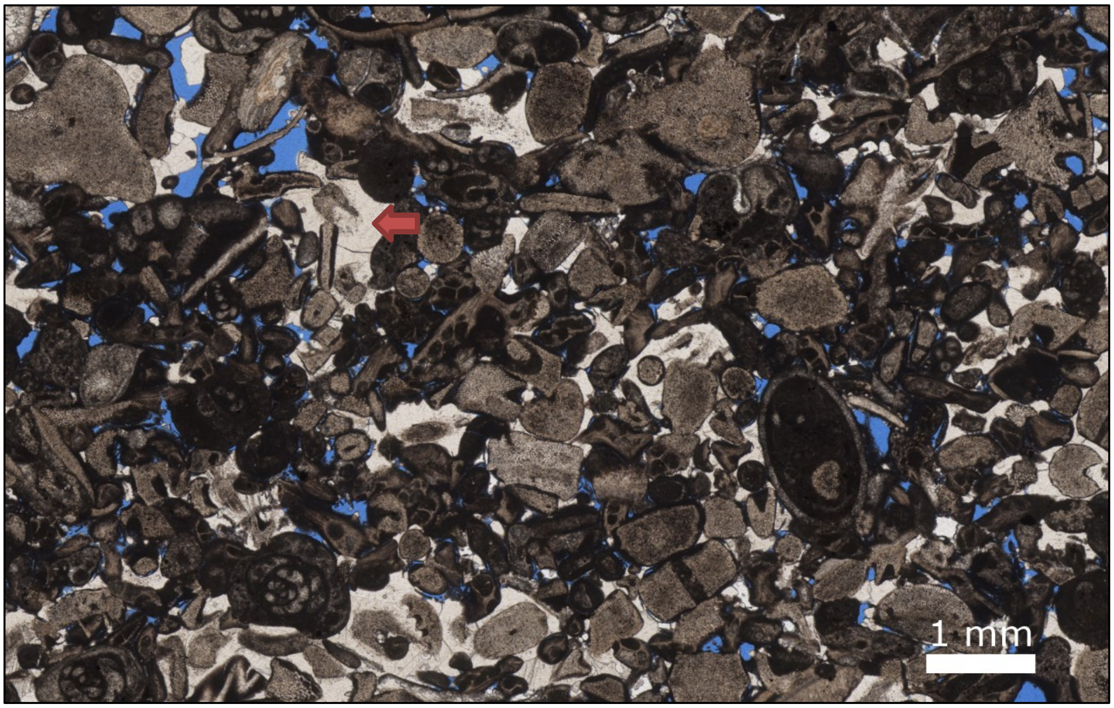

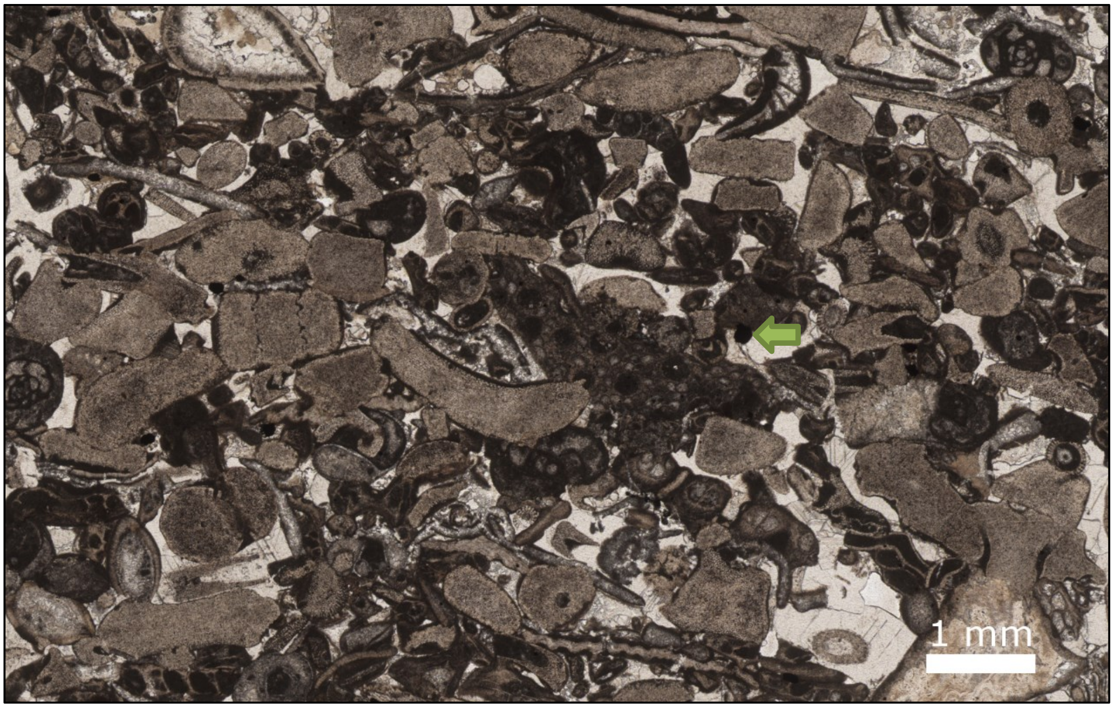

Figure 5.1: Top: A thin section from dry sample with pore space highlight by blue epoxy. Red arrow indicates an example of a region of sparry calcite cement (light colored) among generally darker fossil clasts. Bottom: Thin section prepared from paraffin-wax saturated sample. Green arrow indicates possible void in pore space.

In Fig. 5.1, a thin section prepared from untested Indiana limestone is presented. All thin sections displayed in this paper have been impregnated with a blue-dye epoxy to highlight unoccupied pore space, and to enable thin section preparation through macroscopic failure planes in deformed samples. The pore spaces highlighted in Fig. 5.1 are roughly on the grain size scale, and like the grains, exhibit an irregular geometry. Intergranular porosity is most dominant, while minor intragranular porosity is also present. A thin section was also prepared from an undeformed wax-saturated sample. The volume of paraffin wax is known to significantly decrease upon cooling [*Mancktelow*, 1988], and evidently there is sufficient wax to prevent the blue dye epoxy from permeating the sample, but there appears to be a few black spots, highlighted with a green arrow in Fig. 5.1, potentially indicating voids in the pores space.

Following Dunham's [1962] classification, Indiana limestone is interpreted as a grainstone, considering its grain supported appearance and lack of mud. The grains deposited are mostly shells, left behind by marine invertebrates, that become interlocked, compacted and cemented together [*Ausich et al.*, 1997]. Smith [1966] studied 278 Indiana limestone thin sections from 12 different areas, and found bryozoan pieces were most abundant, followed by plates from echinoderms, primarily crinoids and blastoids. There is a random orientation of the fossil fragments in the untested thin sections. Very few microcracks or mechanical twins are obviously evident. Of the flaws present, most are contained within the sparry calcite cement, and presumably the result of thin section preparation.

The prepared samples contain an average grain density of 2.69 g/cm^3 and porosity of 15.7% with a standard deviation of 0.4% estimated from helium pycnometry. For comparison, the specific gravity of a single calcite crystal is 2.71 [*Klein and Dutrow*, 2008]. An average bulk density of 2.26 g/cm^3 was calculated from the sample dimensions and mass. The sample permeability is 11.3 mD estimated from Hg injection porosimetry.

Paraffin wax (at room temperature) is used as the saturant in these experiments as a replacement for bitumen at low in situ temperatures. The paraffin wax used here (ArtMinds™) was obtained commercially and is completely melted at 82°C. The general composition of paraffin wax is a combination of hydrocarbons (alkanes) of the form C_nH_{2n+2} [*Rossetti et al.*, 1999], whereas bitumen is a much more complex combination of long chain hydrocarbons particularly asphaltenes and maltenes including aromatics and saturates [*Selucky et al.*, 1977]. At low temperature heavy oils and bitumen are known to have small shear modulus [*Han et al.*, 2008]. Manckeltow [1988] and others have studied paraffin wax as a replacement for rock in geological and tectonic models and found that paraffin wax behaves elastically, especially at low temperatures where it remains highly viscous. The viscosity of bitumen at virgin Grosmont reservoir temperatures is estimated to range up to 10^7 cP [*Yang et al.*, 2014], rendering it practically solid under in situ conditions. Similarly, the paraffin wax used is solid at room temperature of 23°C. Its estimated density, from measured dimensions and mass, is approximately 910 kg/m^3.

5.2.2 Sample Preparation

For the compressive strength tests, right cylindrical samples, with a length and diameter of approximately 72 mm and 36 mm respectively, were cored from large blocks of Indiana limestone supplied from a commercial vendor. The cylinders were end-ground to be parallel with at least 25 μm to meet standards set forth under ASTM [*ASTM D4543*, 2008]. After coring and polishing, samples were placed in a vacuum sealed oven and allowed to dry for 24 hours, whereupon they were removed and weighed. To saturate samples, a dish containing a dry sample and block of paraffin wax were placed in a vacuum sealed oven at approximately 90 °C, for 24 hours. At this temperature paraffin wax fully melts and imbibes the sample. The resulting saturation values are >85% as determined by comparisons between the measured masses of the samples when dry and after wax imbibition with that predicted for a hypothetical fully saturated sample. For comparison, bitumen saturation values in production zones average 82% in the Grosmont C and 79% in the Grosmont D reservoirs [*Russel-Houston and Gray*, 2014]. Water and gas fill the remainder of available pore space [*MacNeil*, 2015]. All samples cool in a desiccator jar for a minimum of 24 hours after removal from the oven. The surface pores partially drain when the sample is removed from the liquid wax to cool. Saturation values, therefore, are likely greater than the reported values, aside from the outer pores. This is supported by the thin sections (Fig 5.1, in which no blue dye epoxy penetrates the pore space of the wax-saturated samples.

A pair of foil strain gauges (Omega SGD-10/350-LY41, 350 ohms) were mounted perpendicularly on the sample to record the resulting deformation from testing in the axial and lateral directions. At higher confining pressures (>10 MPa), deformation of the strain gauge into the pore space caused strain gauge failure before testing was complete. To remedy this problem, a layer of epoxy was applied, filling the outer pores and covering the prospective strain gauge area. The strain gauges were then mounted after lightly sanding the cured epoxy until smooth.

The Brazilian tensile testing specimens begin with the preparation of a core sample, which is then cut at a right angle to the longitudinal axis to form a series of discs. The discs were dried, weighed and half were saturated with paraffin wax. Stain gauges were mounted at the centers on a subset of two wax-saturated and two dry samples to monitor the strain under the tensile conditions of the test.

5.2.3 Experimental Procedures

For UCS tests in which only an axial load is applied, the cylindrical core samples are placed in the middle of a load frame (Fig. 5.2A) on top of a spherically seated platen that allows for the movement of the sample through small angles. Under the spherically seated platen is a rigid, square lower platen that rests on a 10.95 cm diameter hydraulic piston (Simplex RLN 1002). The axial load is applied as steadily as possible by alternately operating two hand pumps that control the hydraulic piston, and uniform pressurization rates of ~0.7 MPa/sec were repeatable. Failure ultimately occurs as the sample is pressed against the rigid upper platen. Applied forces are determined from a pressure transducer (Wika Model A-10) with 0.3 MPa resolution connected to the hydraulic piston. The resulting strain gauge deformations are obtained from the mV level potentials across an unbalanced Wheatstone bridge (excitation voltage = 5V) using procedures developed in Melendez-Martinez and Schmitt (2016). Pressure transducer and Wheatstone bridge responses were digitally recorded to a resolution of 16 bits at a sampling rate of 20 Hz using a National Instruments PXI-1033 converter controlled by a Labview™ program.

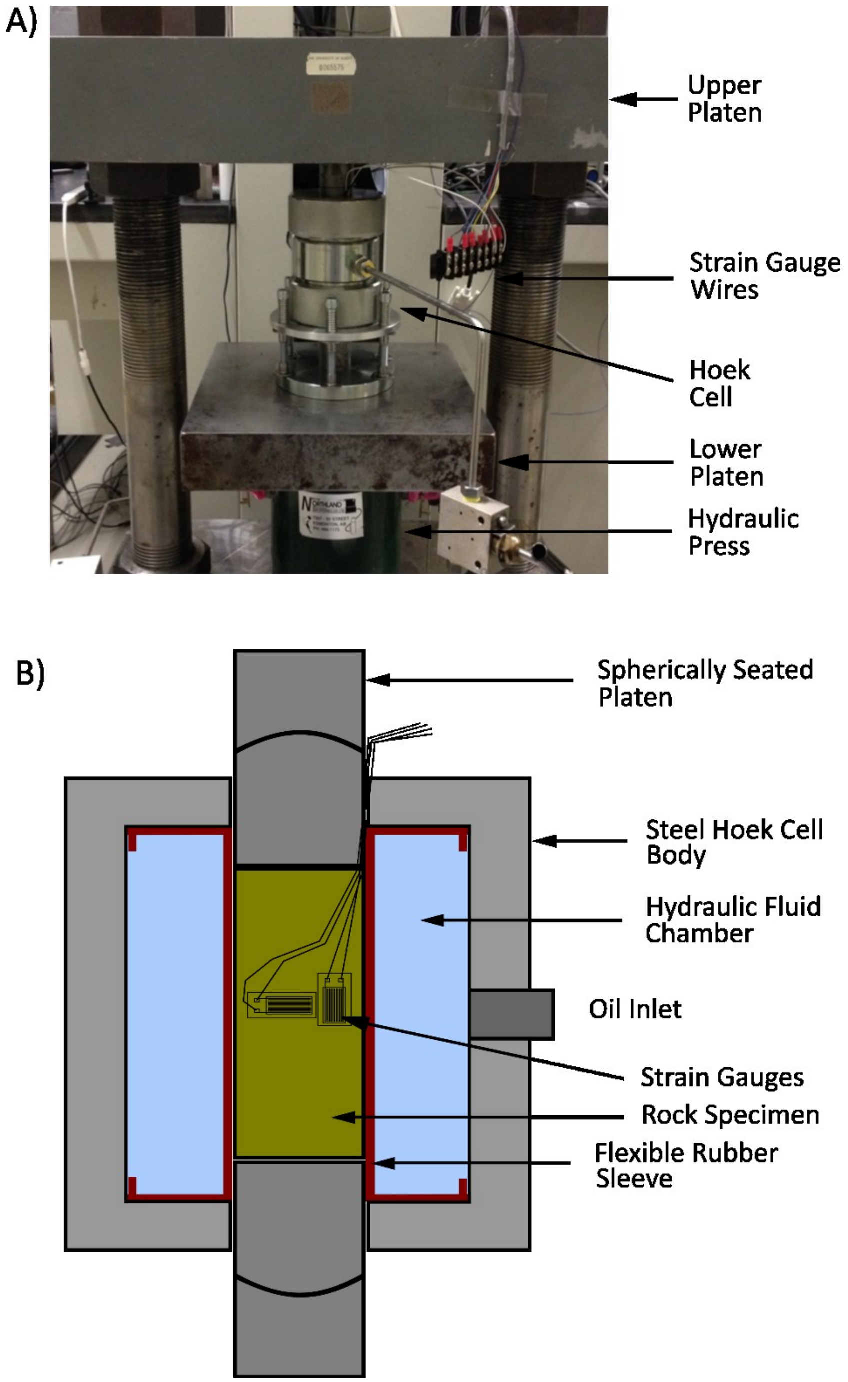

Figure 5.2 A) Image of triaxial strength test laboratory set-up, the same load frame was used for all experiments. B) Schematic of Hoek Cell.

A Hoek cell (38.1x75 mm from Jet Materials) was used to apply a lateral confining pressure to the samples during triaxial testing (Fig. 5.2B). The confining pressure is set by hand pumping hydraulic fluid into the chamber of the Hoek cell, where the sample resides in a flexible rubber sleeve. Spherically seated platens are placed on each end of the sample. Both axial and confining pressures are continuously measured during these tests.

A deficiency of the current Hoek cell arrangement is that once the lateral confining pressure is set it cannot be adaptively controlled. During triaxial testing, lateral expansion of the sample causes the confining pressure to increase by as much as 6 MPa. This problem is especially prevalent at confining pressures above 10 MPa, where effects of ductile deformation are observed. The axial strain is limited to 1% in stress-strain plots (Fig. 5.4 and 5.5) as greater strain values tend to produce confining pressures that deviate more than 5% from the intended value for the confining pressure.

Standard Brazilian tests [*ASTM D3967-08*, 2008] were also employed to obtain measures of the material's tensile strength. A sample disk is placed in the load frame (Fig. 5.2A) and a force is applied across the diameter of the disk as shown in Fig. 5.3B. Plywood cushions ¼ inch thick are used to distribute the concentrated force at contact points of the sample and platens to decrease the risk of sample failure by compression. The wood cushions are cut to a width of 4.5 mm producing a contact arc with the sample of roughly 15°. For such a contact arc, the resulting error in tensile strength relative to a true point load has been estimated to be approximately 10% [*Perras and Diederichs*, 2014]. Tension is generated through the center of the disk during loading, ultimately causing the disk to pull apart, typically in half. Like the UCS and triaxial tests, the load is increased continuously until failure occurs and a strain gauge across the center of the disk, perpendicular to the applied force, measures the deformation.

A Canon 7D camera with frame rate of 60 fps was used to record video of the UCS and Brazilian tests. The collected video can be analyzed to determine the validity of the Brazilian test as failure must initiate near the disk center. Core photos of the triaxially tested samples are taken post failure as the Hoek cell does not allow video recording. All samples are handled cautiously post testing and taped backed together (if failure is brittle) and stored in plastic bags for further analysis.

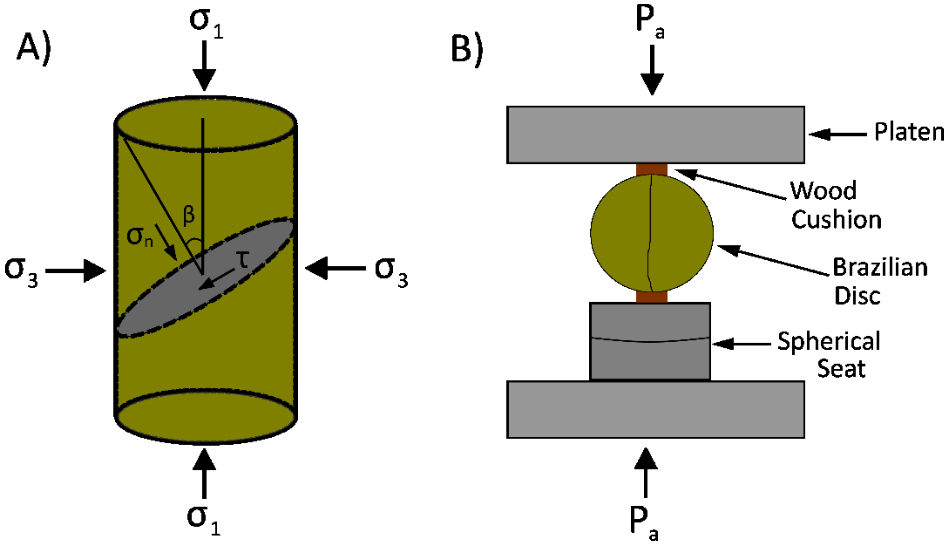

Figure 5.3 A) Schematic of the stresses acting on a core sample under compression and resulting failure plane. σ_1 and σ_3 indicate the maximum and minimum principal stresses respectively, σ_n is the normal stress to the failure plane, τ is the shear stress, and β is the angle between σ_n and σ_1. B) Schematic of Brazilian tensile strength tests. P_a denotes the applied pressure and the typical failure plane through the sample is drawn.

5.3 Experimental Results and Discussion

5.3.1 Mechanical Data

As commonly reported, the convention for the mechanical data presented is positive for compressive stress and shortening strain. The maximum and minimum principal stresses acting in the compressive strength experiments are denoted by σ_1 and σ_3 respectively (Fig. 5.3A). Following the convention, the UCS tests can be defined as σ_1=axial stress, and $\sigma_2=\sigma_3=0$. For the conventional triaxial tests, σ_1=axial stress, and $\sigma_2=\sigma_3$=applied confining pressure. The Brazilian test data is presented in terms of tensile splitting strength (σ_t), and is calculated by the following [*ASTM D3967-08*, 2008]:

$$\sigma_t = \frac{2P_a}{\pi D t} \tag{1}$$

Where P_a is the applied pressure at failure, while D and t denote the disk diameter and thickness, respectively.

5.3.2 Compressive Strength Data

Selected stress-strain curves obtained from the compressive strength tests are displayed in Fig. 5.4 and 5.5. The interpreted peak strength values presented in Fig. 5.7 are highlighted with arrows. The stress-strain curves with confining pressures below 10 MPa end abruptly as brittle shear failure of the sample occurs. The interpreted failure stress is intuitive and is reported as the highest value of stress endured by the sample prior to failure. For strains collected under conditions of $\sigma_3 \geq 10$ MPa, the curves are noticeably different as the samples exhibit ductile behavior. Instead of a large stress drop from abrupt failure, the stress-strain curves again become linear beyond the yield point. The measured stress is observed relatively constant as the sample is not supporting additional load, and strain is increasing. Following the recommendation of Schwartz [1964], for this ductile behavior, the peak stress value is reported where the slope of the stress-strain curve becomes a minimum (tangent modulus is a minimum) and remains practically constant. Some lateral stress-strain curves (i.e. dry 20 MPa CP curve) do not show an increasing strain, as expected from the axial stress-strain curve. This is likely the result of strain gauge failure. In the triaxial tests performed lateral strain gauge failure was much more prevalent than axial gauge failure.

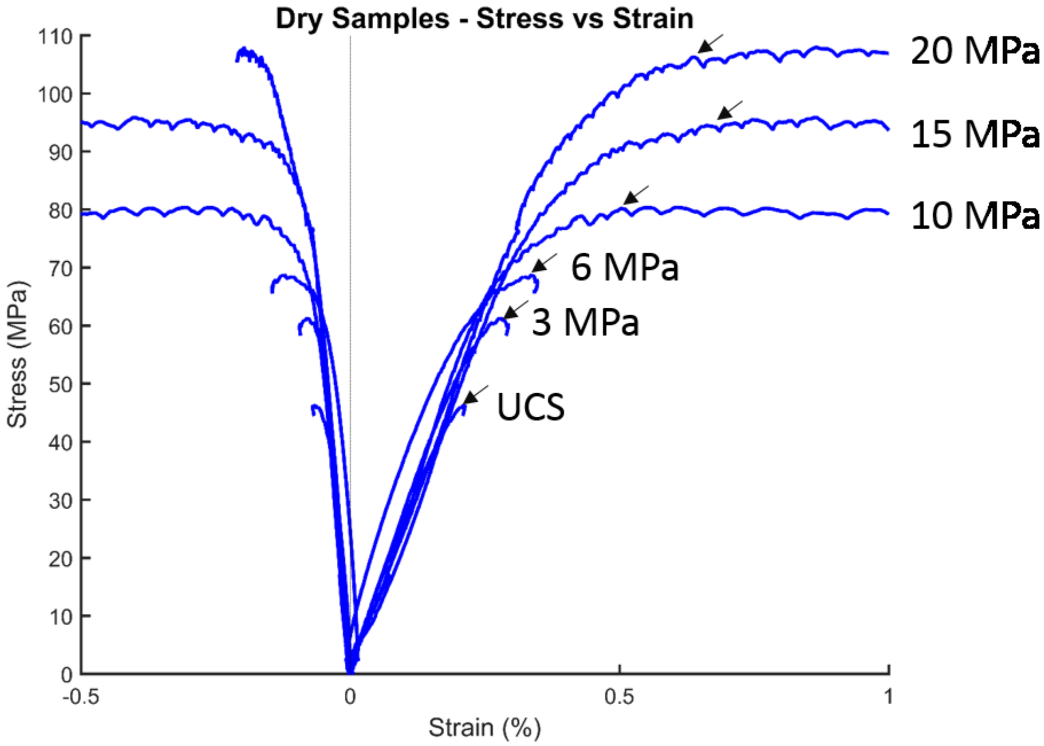

Figure 5.4 Axial stress vs axial (positive strain) and lateral (negative strain) strain curves for dry samples at confining pressures (σ_3) of 0 (UCS), 3, 6, 10, 15 and 20 MPa. Arrows mark interpreted failure points.

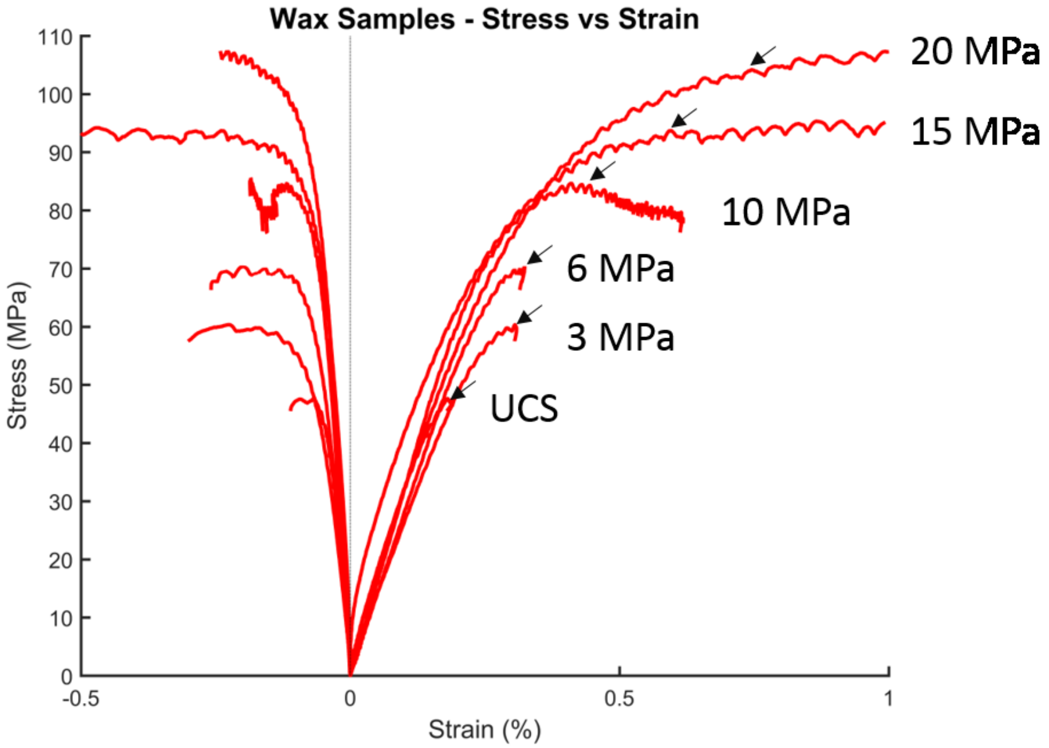

Figure 5.5 Axial stress vs axial (positive strain) and lateral (negative strain) strain curves for wax-saturated samples at confining pressures (σ_3) of 0 (UCS), 3, 6, 10, 15 and 20 MPa. Arrows mark interpreted failure points.

The photos in Fig. 5.6 show the post-failure condition of a representative sample subset after triaxial testing. As the confining pressure is increased the sample failure changes from brittle to ductile as has long been known for such rock types. The samples subjected to a low confining pressures of σ_3 = 3 MPa clearly experienced brittle failure. The slope of these curves is relatively linear up to the point of failure. Even by modest confining pressures of σ_3 = 6 MPa the curves differ noticeably with a longer range where the strain increases nonlinearly with axial stress prior to a still brittle failure with an obvious failure plane consistent with Mohr-Coulomb failure theory. Similar behaviour is seen at these lower confining pressures for both dry and wax-saturated samples.

At higher confining pressures, however, the presence of the wax appears to retard the onset of more ductile failure. When σ_3 = 10 MPa, for example, the observed peak stress for both the dry and the wax-saturated samples are similar. However, the post-test visual inspections of the samples (Fig. 5.6B) show that the wax-saturated sample underwent brittle failure (i.e. in 2 distinct pieces) whereas the dry sample remained intact albeit containing a through-going shear failure plane, suggesting the wax plays a role in promoting brittle failure at this confining pressure. There is also evidence of strain softening before brittle failure in the wax saturated sample at this confining pressure. The reasons for this are currently not understood but are possibly related to the fact that an undrained pore pressure response may exist causing the effective stress on the sample to be diminished.

When σ_3 is brought to 15 MPa, the dry sample exhibits a malleable character with no well-developed failure plane evident upon visual inspection. The complementary wax-saturated sample is intact and noticeably barrel-shaped; showing signs of ductile deformation. However, it also contains a prominent shear zone that is much wider than the plane of failure in other triaxial tests. Both samples undergo ductile deformation at the highest confining pressure of $\sigma_3 = 20$ MPa. Note that photo of the dry sample tested with $\sigma_3 = 20$ MPa was broken during handling (the closest substitute, at $\sigma_3 = 17$ MPa, is shown in Fig. 5.6D_{dry}), but prior to this the deformed sample was barrel shaped with no visible failure plane similar to the corresponding wax-saturated sample of Fig. 5.6D_{wax}.

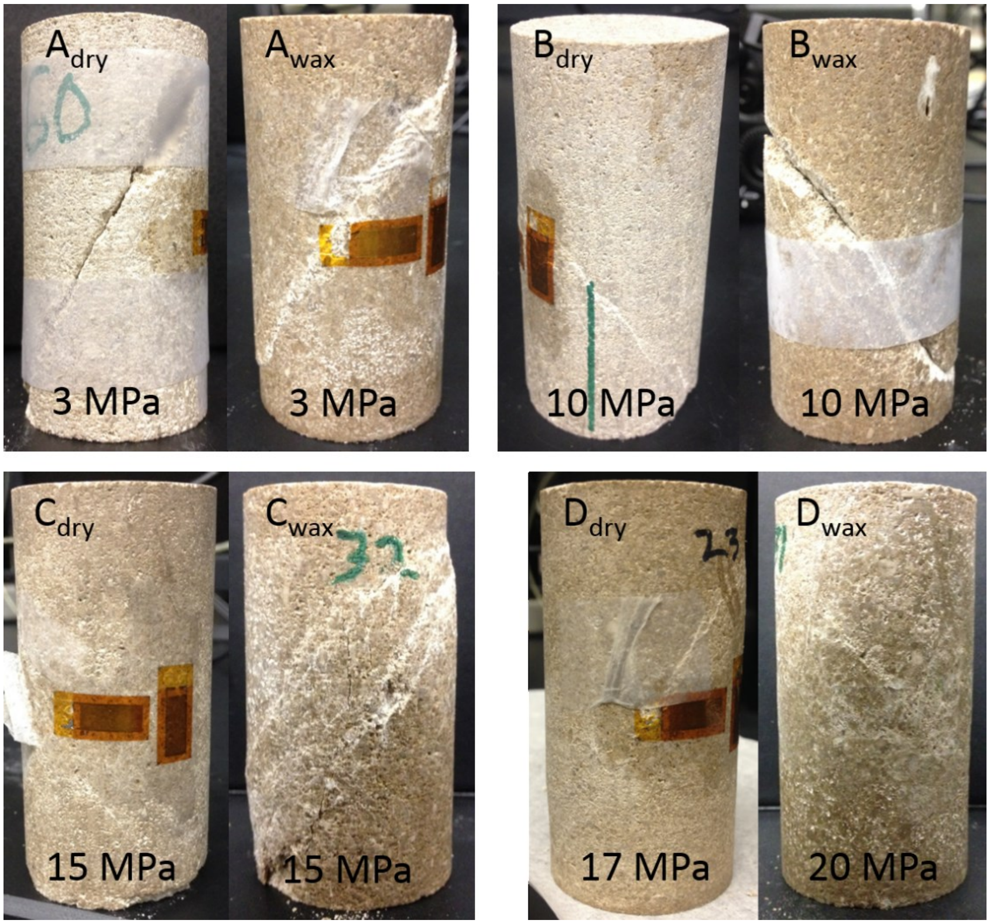

Figure 5.6 Photos of samples after triaxial testing. Dry samples are pictured in the top row and wax-saturated samples on the bottom row. Confining pressures used during testing: 3 MPa (A), 10 MPa (B), 15 MPa (C), 17 MPa (D_{dry}) and 20 MPa (D_{wax}).

The compressive strengths of 39 total UCS and triaxial tests comparing dry sample data to paraffin wax-saturated sample data (Table 3) are plotted in (Fig. 5.7) as the peak strength of each sample in terms of axial stress (σ_1) applied versus the confining pressure (σ_3). For comparison, Table 3 contains data from the recent study by Walton et al. [2015]. The peak strength values were estimated from the Mohr-Coulomb fit to the data; the Young's modulus values, estimated (to 0.1 MPa) from a plot, were averaged at each confining pressure.

Table 3 Compressive strength data

Sample	**σ3 (Mpa)**	**Peak Stress (MPa)**	***E* (GPa)**	***v***
		Dry Sample Data		
S49	0	43.7	32.5	0.27
S52	0	46.3	26.2	0.20
S53	0	46.3	23.1	0.23
S59	0	44.5	24.6	0.22
S7	1	47.4	36	0.20
S16	1	51.9	30.1	0.28
S8	3	60.6	30.2	0.17
S60	3	60.5	26.7	0.21
S54	6	67.9	26.6	0.25
S10	6	69.5	23	0.25
S25	8	73.3	33.1	0.23
S11	10	76.8	29.1	0.26
S13	10	77.2	29.6	0.19
S22	12	86.6	31.1	-
S56	12	83.4	32.8	0.23
S14	15	91.6	26.1	0.22
S17	15	88.2	31.1	0.20
S23	17	103.5	-	-
S12	20	106.3	26	0.22
S15	20	101.4	36.3	-
Average			29.2	0.23
Std. Dev.			3.9	0.03
		Wax-Saturated Sample Data		
S24	0	45	24.2	0.37
S37	0	47.6	27.8	0.27
S39	0	44.3	24.4	0.29
S40	0	46.8	21.9	0.32
S18	1	50.9	24.6	0.32
S36	1	48.8	28.4	0.29
S20	3	58.8	24.1	0.31
S35	3	53	22.8	0.20
S21	6	67.9	27.6	0.27
S34	6	66.8	21.9	0.18
S26	8	75	27	0.20

S19	10	79.8	31.2	0.24
S33	10	77.5	33.6	0.18
S27	12	80.9	29.1	0.18
S28	15	93.5	26.1	0.22
S32	15	89	27.2	0.21
S29	17	95.7	27.8	0.21
S30	20	104.5	25.6	0.21
S31	20	102.8	26.2	0.18
Average			26.4	0.24
Std. Dev.			2.9	0.06
Data from Walton et al. [2015]				
-	0	62.6	24.6	-
-	1	67	24.5	-
-	2	71	24.3	-
-	4	79	24.7	-
-	6	87	25.6	-
-	8	94	26.6	-
-	10	102	26.2	-
-	12	108	26.4	-
Average			-	0.16
Std. Dev.			-	0.028

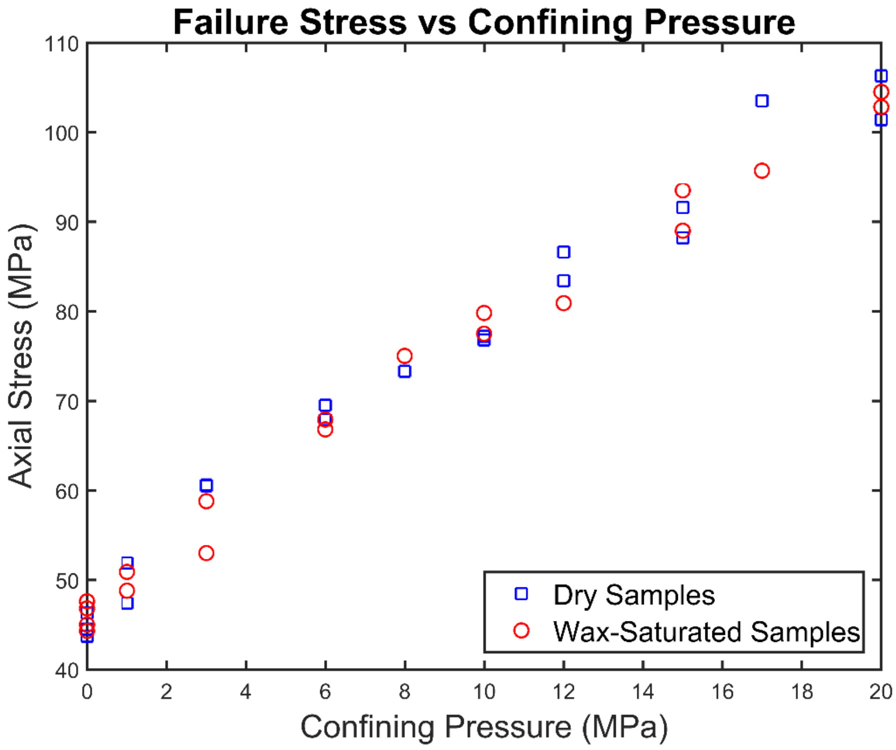

Figure 5.7 Peak strength of dry and wax-saturated Indiana Limestone samples as a function of confining pressure.

The interpreted failure strength increases as expected from approximately 45 MPa for UCS tests up to roughly 105 MPa for triaxial tests with an applied confining pressure of 20 MPa. There is no discernable difference in peak sample strength when comparing the dry and wax-saturated samples. Both datasets can be fit with linear functions of:

$$\sigma_1 = 2.96\sigma_3 + 47.8\ MPa \tag{2}$$

$$\sigma_1 = 2.90\sigma_3 + 47.5\ MPa \tag{3}$$

The linear functions (of the general form $\sigma_1 = P1 * \sigma_3 + P2$) have coefficients of determination (R^2) near 1, indicating a very good fit to the datasets. The 95% confidence range (Table 4) of each coefficient, P1 and P2, show these equations are statistically very similar.

Table 4 Linear regression parameters from strength data

	P1 (95%)	P2 (95%)	R^2
Dry	(2.74, 3.18)	(45.5, 50.2)	0.98
Wax-Saturated	(2.73, 3.08)	(45.7, 49.2)	0.99

This behaviour suggests that a simple linear Mohr-Coulomb failure criterion, defined as:

$$\tau = S_0 + \sigma_n \mu_i \tag{4}$$

may adequately describe the shear failure in this material under the testing conditions and is consistent with the findings of Walton et al. [2015].

The linearized form of the Mohr-Coulomb failure criterion is plotted along with the corresponding Mohr circles for all compressive tests completed in Fig. 5.8. The internal angle of friction, often represented as μ_i, was determined by finding the slope, n, of the best fit line to the data plotted in Fig. 5.7 by the following formula [*Zoback*, 2007]:

$$\mu_i = \frac{n-1}{2\sqrt{n}} \tag{5}$$

The cohesion, S_0, was determined by finding the y-intercept (C_0) of the above-mentioned best fit line to the triaxial testing data using the formula:

$$S_0 = \frac{C_0}{2\left[\left(\mu_i^2 + 1\right)^{\frac{1}{2}} + \mu_i\right]} \tag{6}$$

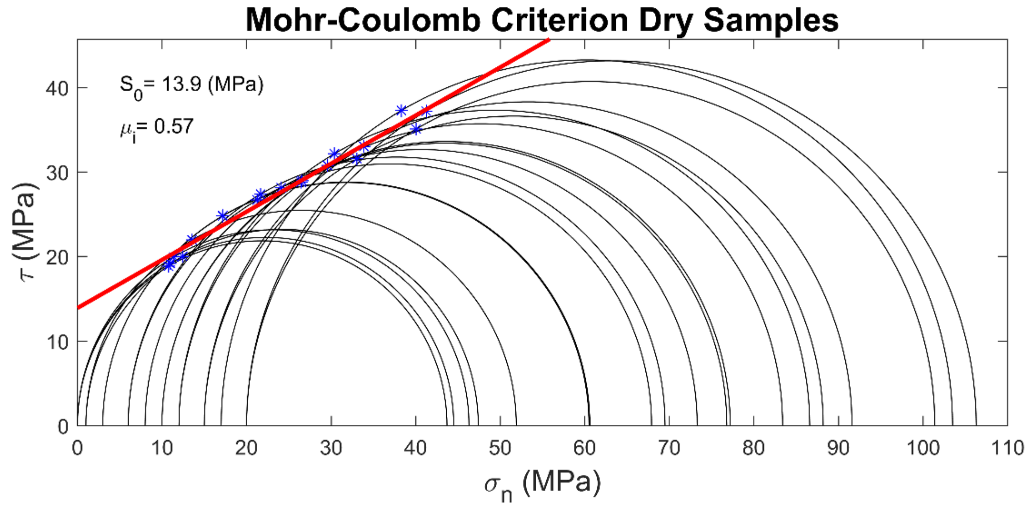

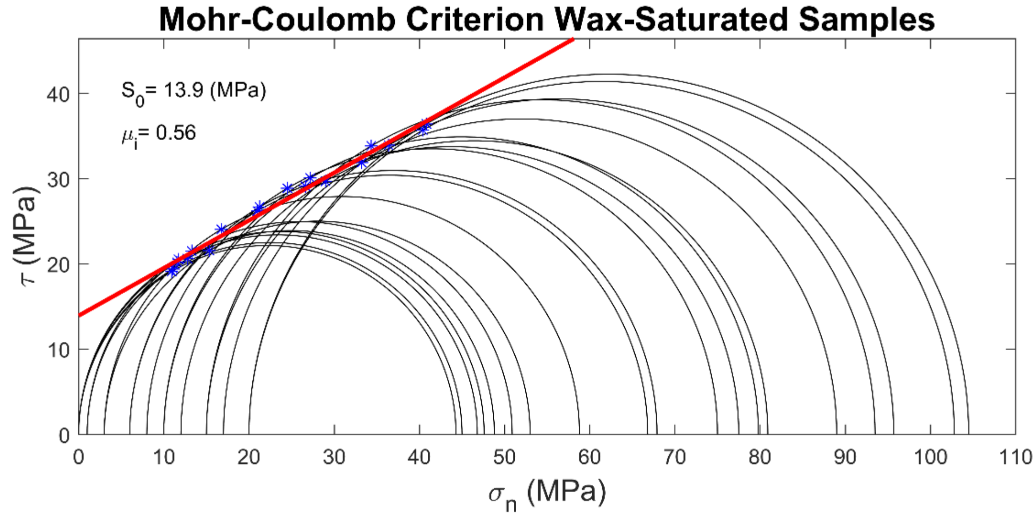

Figure 5.8 Upper: Mohr-Coulomb failure criterion for all measured dry samples. Lower: Mohr-Coulomb failure criterion for all measured wax-saturated samples.

The failure points plotted on the Mohr circles (blue stars Fig. 5.8) are found by:

$$\tau_f = \frac{1}{2}(\sigma_1 - \sigma_3) * sin2\beta \tag{7}$$

$$\sigma_n = \frac{1}{2}(\sigma_1 + \sigma_3) + \frac{1}{2}(\sigma_1 - \sigma_3) * cos2\beta \tag{8}$$

where angle β was estimated, when possible, using a protractor on the failed sample's shear failure plane. Mohr-Coulomb criterion parameters for the two datasets are nearly identical and the resulting envelopes fit the datasets reasonably well, as expected from the observed trends in the peak strength plot of Fig. 5.7.

5.3.3 Elastic Properties

In addition to peak strength, the rock's Young's modulus (*E*) and Poisson's ratio (*ν*) were measured using the strain gages under compressive stress. For purposes of relative comparison, the value of the average modulus, *E*, reported here was obtained from the slope of the of the linear portion of the axial stress-strain plot by linear regression. The axial stress-strain curve (Fig. 5.9) begins with positive curvature or increasing slope, progresses to a practically steady value where linear regression is applied to find Young's modulus, and lastly, the curvature becomes negative before sample failure. The linear portion of the stress-strain curve was determined visually, and the resulting Young's modulus varied up to approximately 5% depending on the stress range selected for linear regression. Poisson's ratio was estimated by dividing Young's modulus by the slope of the lateral-stress strain plot's linear section. The estimated values are posted in Table 3.

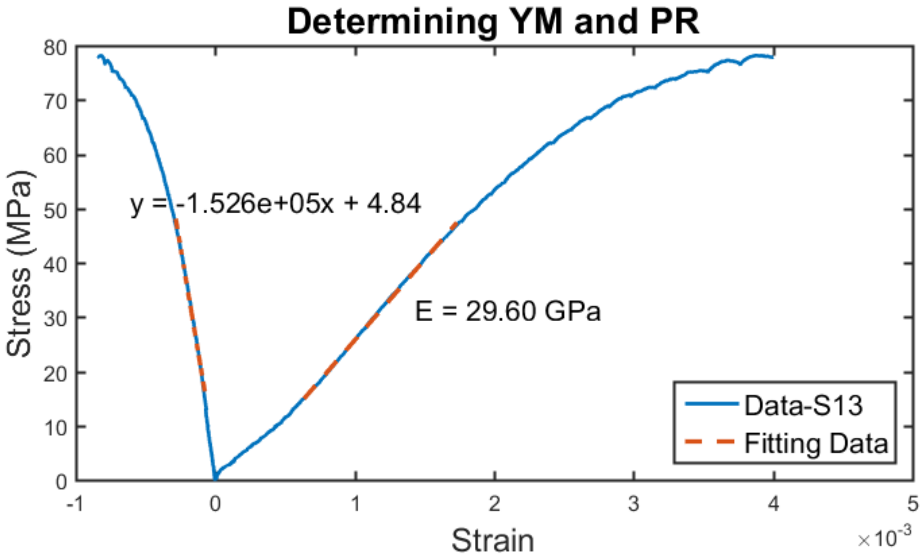

Figure 5.9 Example of Young's Modulus and Poisson's Ratio determination. The straight portion of both the axial (positive) and lateral (negative) stress vs strain curve is isolated, and a linear fit is determined. The slope of the axial stress-strain curve is Young's modulus (E), and for sample 13 is 29.6 GPa. The slope of the lateral stress-strain curve is used to calculate Poisson's ratio.

The determined Young's moduli are plotted versus confining pressure in Fig. 5.10, and this measure shows a great deal of scatter. At first glance, the data looks somewhat erratic; but it should be noted that for the 8 confining pressures where both dry and wax-saturated values available, 6 of these have greater values of Young's moduli for dry samples (the exceptions being at 6 and 10 MPa). Although the results are inconclusive, it could suggest that the dry samples behave in a stiffer manner than the wax-saturated samples. This is somewhat unexpected as one would expect a material saturated with a viscoelastic fluid to be stiffer than its unsaturated equivalent. Perhaps the wax is providing an means for dissipation of the applied stresses thus making it less stiff. On the other hand, the average wax-saturated Young's modulus value is 26.4 GPa, while the average dry Young's modulus value is 29.2 GPa. If an error of 5% is expected in the average values, the upper limit of average wax-saturated sample Young's modulus and lower limit of the dry sample's Youngs modulus are both 27.7 GPa. This indicates that it is statistically possible, although not likely, that there is no trend in the data. One observable trend in the Poisson's ratio data is more scatter in values at lower confining pressures. This is evident in both datasets. Wax-saturated samples also have higher Poisson's ratio values at these low confining pressures (<6 MPa). The average Poisson's Ratio values for dry (0.23) and wax-saturated (0.24) samples are nearly identical.

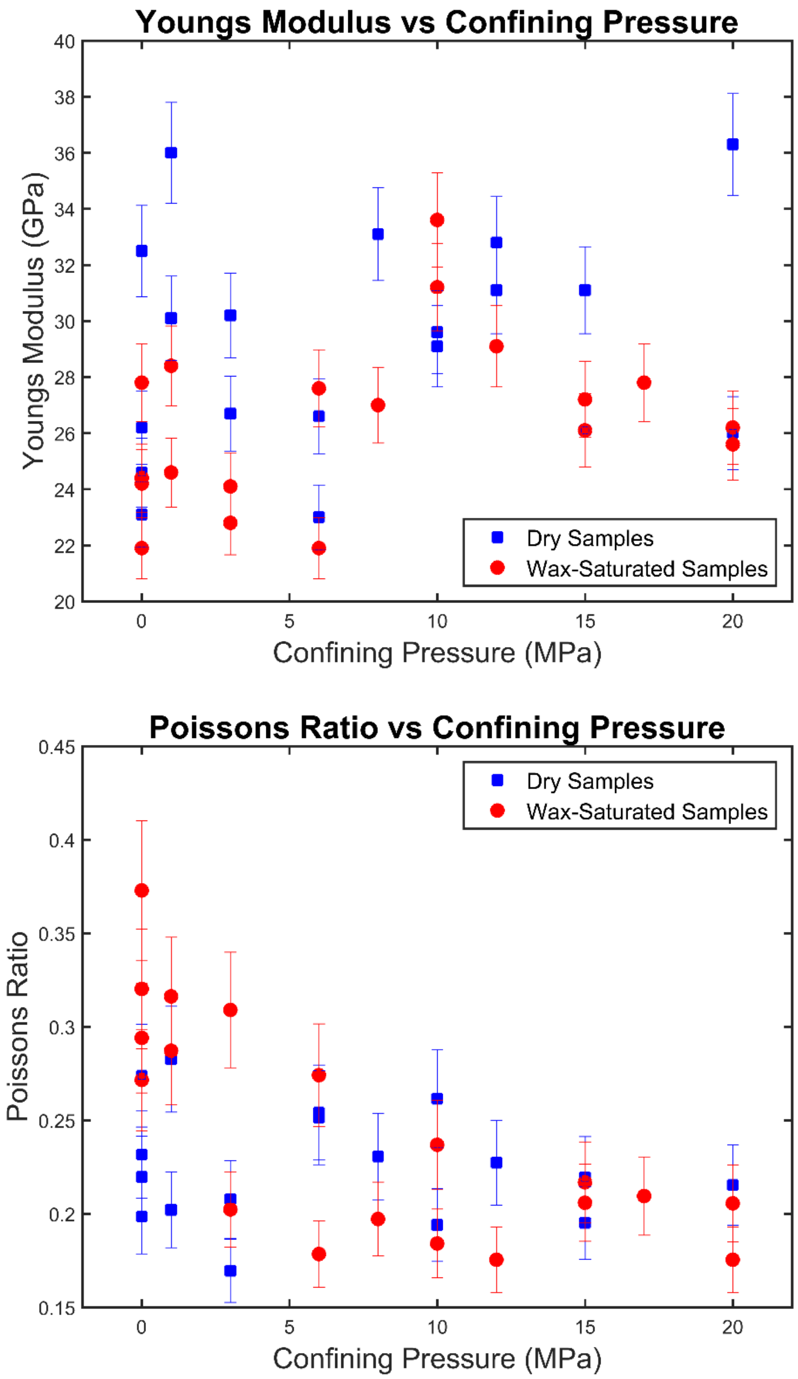

Figure 5.10 Elastic properties of tested samples. Top: Estimated Young's Modulus plotted versus confining pressure. Bottom: Estimated Poisson's ratio plotted versus confining pressure.

5.3.4 Microscopic Observations

To investigate the effects of both wax saturation and confining pressure on failure at the microscopic scale, four sets of thin sections from samples subjected to triaxial testing are presented in Fig. 5.11. The thin sections were prepared with the long edge parallel to the σ_1 (axial compression) direction and scanned under cross-polarized and non-polarized light using a (Nikon CoolScan 5000 ED, 4000 dpi). Where brittle failure occurred, the thin sections intersect the failure plane perpendicular to strike. The same area and magnification of the section are shown in each image of Fig. 5.11.

Dominate structural mechanisms observed in thin sections include microfractures and mechanical twinning of calcite (Fig. 5.12). Twinning in calcite is an example of intracrystalline deformation and is known to occur at room temperature [*Turner et al.*, 1954] and very low strains of less than 1% [*Burkhard*, 1993]. Mechanical twinning is thought to be caused by pore collapse resulting from confining pressure application and further collapse and stress concentration when the axial load is applied in triaxial tests [*Groshong Jr.*, 1974; *Friedman et al.*, 1976]. Friedman and Heard [1974] performed creep experiments on Carthage Limestone (lower porosity than Indiana Limestone) and found the number of twinned grains and lamellae spacing index was a function of both differential stress and loading duration. Hugman [1979] noted that because twinning occurs at low differential stresses, tensile microfractures can also be initiated at very low stress levels. He found that grain-boundary microcracks were most common in UCS tests and decreased with increasing confining pressure, while intragranular microfractures increased with confining pressure. Olsson and Peng [1976] recognized twinning as a predominant microcrack nucleation mechanism. Microfractures are precursive to the macroscopic failure of a specimen [*Friedman*, 1975].

In Fig. 5.11, there is evidence of increased mechanical twinning intensity (#/mm) and microfracturing with increasing differential pressure (σ_1 - σ_3). This is consistent with reports from Groshong [1974] and Jamison and Spang [1976] on room temperature triaxial tests of Indiana limestone, although the lowest differential stress at failure they recorded was approximately 85 MPa, roughly corresponding to the highest differential stress recorded in these experiments. A recent and detailed investigation into the micromechanics of dry Indiana limestone under triaxial compression (with σ_3 = 5 MPa and 20 MPa) was performed by Vajdova et. al [2012], finding calcite cement undergoes significant microcracking while the allochems remain relatively intact, even at high strain.

Thin sections from Fig. 5.11A show a brittle fracture formed during testing at 3 MPa confining pressure. There is a slight increase in twinning localized to the failure plane compared with the undeformed section of Fig. 5.1. Most microfractures appear to be intergranular, contained within the calcite cement, although there exists a small number of intragranular fractures. The blue dye epoxy does not penetrate the wax-saturated sample other than at the site of macroscopic failure, as expected. At 10 MPa (Fig. 5.11B) confining pressure both samples again undergo brittle failure, but there are noticeable increases in twinning intensity and microfracture development. These changes occur in both cement and grains. The dominant direction of microcrack propagation is parallel to the σ_1 direction (horizontal). The wax-saturated specimen has a larger damage zone with more extensive fractures forming at an oblique angle to the macroscopic failure plane.

The dry and wax-saturated samples clearly experience different failure modes during the tests performed at 15 MPa confining pressure. Fig. 5.11C_{wax} shows an extensive damage zone around the failure with pervasive microcracking networks, and therefore increased sample permeability. In contrast, there is no macroscopic failure plane present in thin section prepared from the dry sample (Fig. 5.11C_{dry}), although mechanical twinning and microfractures exist. Pore collapse and fractures are responsible for increasing the ratio of intragranular to intergranular porosity.

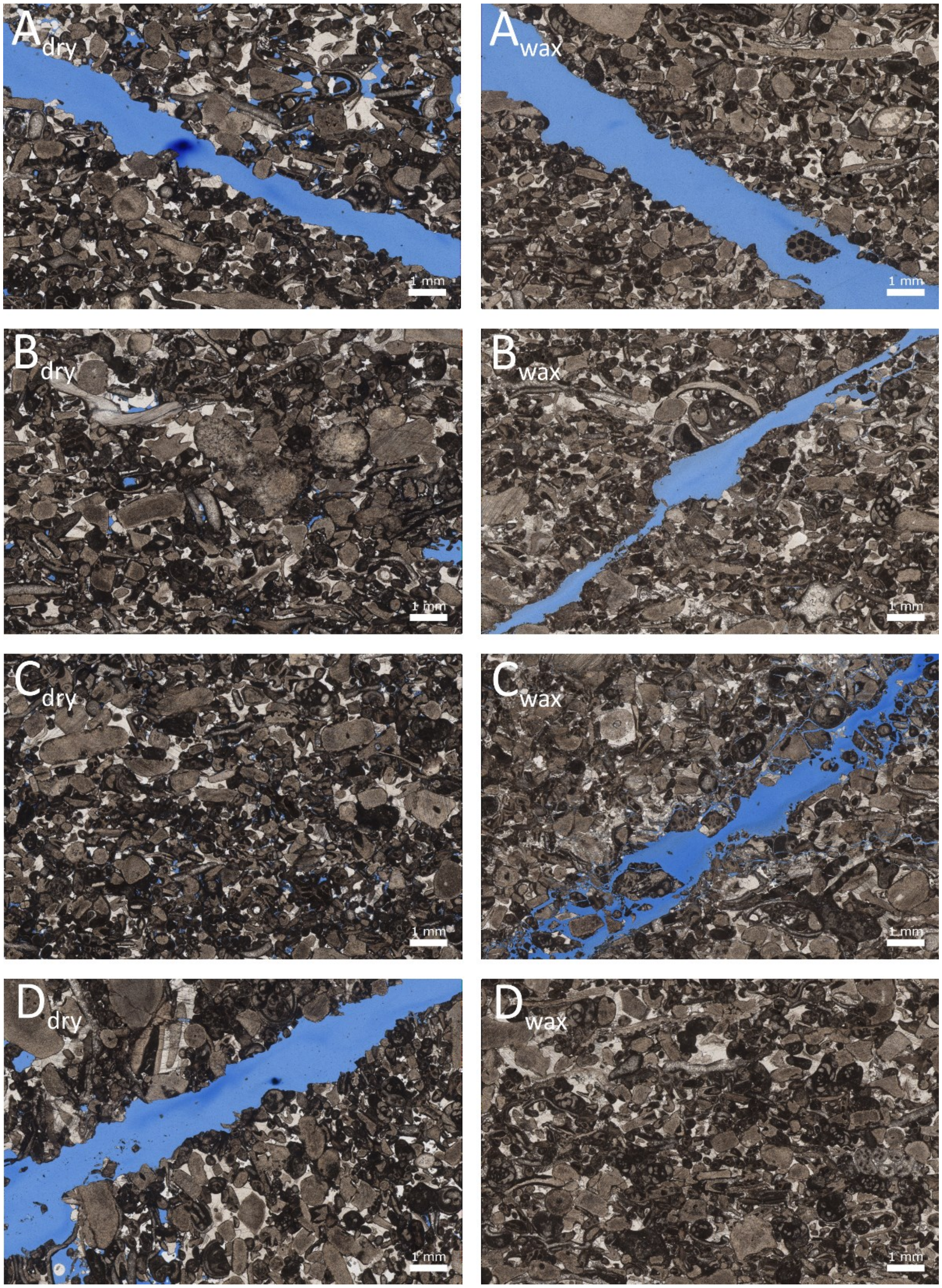

Figure 5.11 Thin sections prepared from deformed samples. Confining pressure for thin sections are as follows: A) 3 MPa, B) 10 MPa, C) 15 MPa, D) Dry – 17 MPa, Wax – 20 MPa.

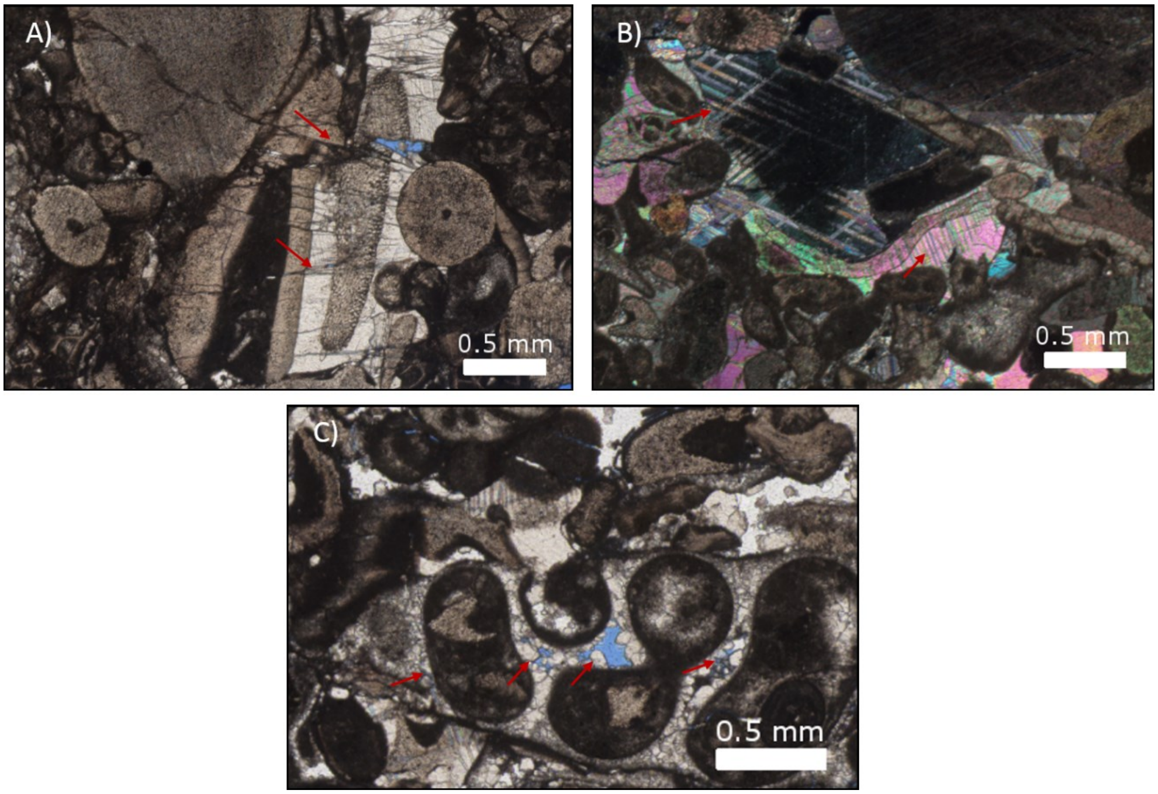

Figure 5.12 Magnified thin sections showing (red arrows) examples of: A) microfractures aligned parallel to σ_1 offsetting fossil clasts, B) calcite twinning under polarized light, and C) pore collapse with fragmented cement fill. Microfractures are evident in all thin sections.

Unfortunately, thin sections could not be prepared from dry samples tested at 20 MPa confining pressure, due to previously discussed problems with sample damage during removal from the rubber Hoek cell sleeve. However, a thin section was prepared through the dry sample tested at 17 MPa confining pressure (Fig. 5.11D_{dry}), containing a macroscopic failure plane. The microfractures developed propagate through grains and cement and offset along these features is observed, but at this scale most cracks appear closed (cannot detect blue epoxy). The thin section shown in Fig. 5.11D_{wax} is taken from the first wax-saturated sample that exhibits fully ductile deformation. The grains are rotated and align parallel to the maximum compressive stress. Intense mechanical twinning is detected and most visible microfractures also appear closed at this scale.

5.3.5 Tensile Strength Data

The Brazilian tensile test is used to experimentally determine the tensile strength of 10 dry and 10 wax-saturated disks. The prepared disks were cut from 4 core samples, then evenly distributed between dry and wax-saturated conditions to prevent sample bias. The results are plotted in Fig. 5.13. It is interesting to observe the greater average tensile splitting strength appears of the samples saturated with paraffin wax compared to the dry samples. Ignoring the highest and lowest values from each dataset, then taking the average, we get an approximately 17% increase in tensile splitting strength (6.1 MPa – dry, 7.1 MPa – wax-saturated) with the addition of the paraffin wax. The standard deviation of splitting tensile strength is 0.39 for the dry tested samples and 0.58 for the wax-saturated samples. The resulting tensile strength increase for wax-saturated samples is significant.

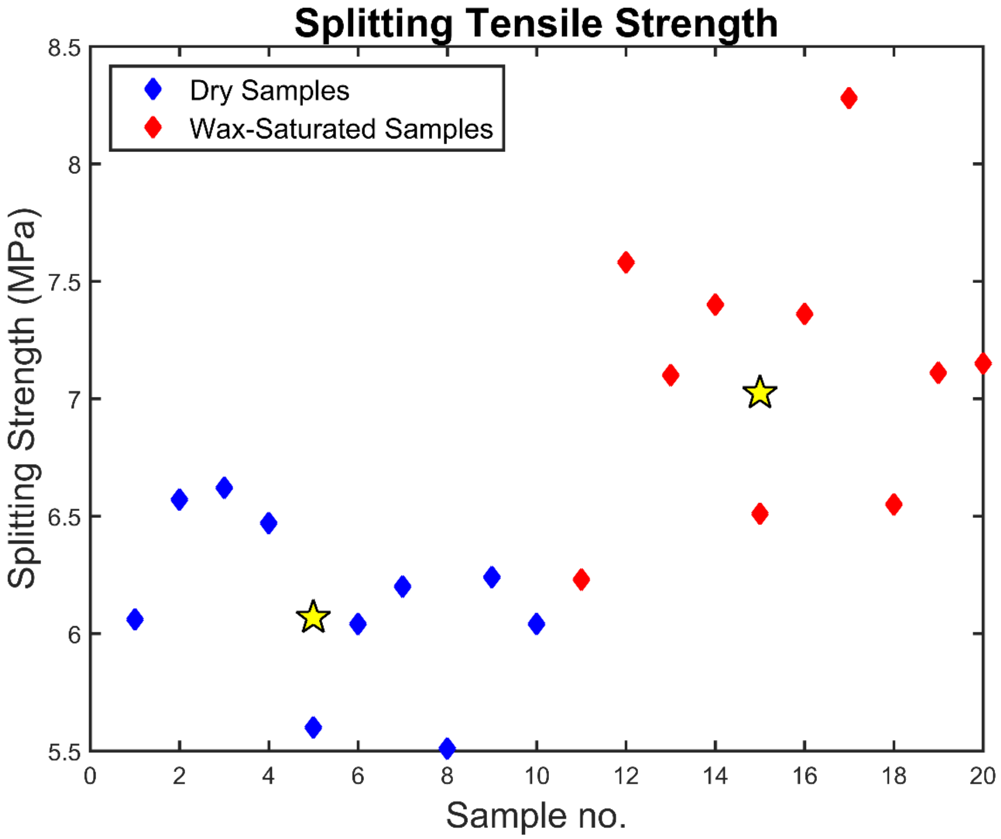

Figure 5.13 Plot of the splitting tensile strength for each sample. Stars indicate the average tensile splitting strength excluding the highest and lowest recorded value from each dataset.

Evidently, the paraffin wax used in these experiments does not have the same influence as the mobile liquids used by Vutukuri [1974]. If the wax had a low surface tension and dielectric constant, one would expect the tensile strength to be comparable to the dry sample; but an increase in tensile strength is unexpected. In our case, the wax is acting in opposition to the tensile stress created through the center of the disk during Brazilian testing. The wax is perhaps acting as a glue bonding the sample together. Paraffin wax would have a tensile strength on its own although this would be difficult to measure with the

Brazilian test due to the ease of deformation in compression. The tensile strength of the paraffin wax may be contributing to the overall tensile strength of the samples from Brazilian tensile testing.

An increase in the tensile strength of rock resulting from the presence of a viscous fluid has potential implications for the drilling and completion of wells in bitumen saturated carbonate reservoirs like the Grosmont. In zones of bitumen saturation, a wellbore could possibly endure higher tensile stresses and in zones of lower saturation (naturally or production associated) the wellbore could be more susceptible to tensile failure of the borehole wall. Morin [2017] analyzed 22 image logs collected from wells drilled through the Grosmont formation and interpreted the presence of drilling induced tensile fractures in 20 of the image logs. No borehole breakouts were found in the dataset.

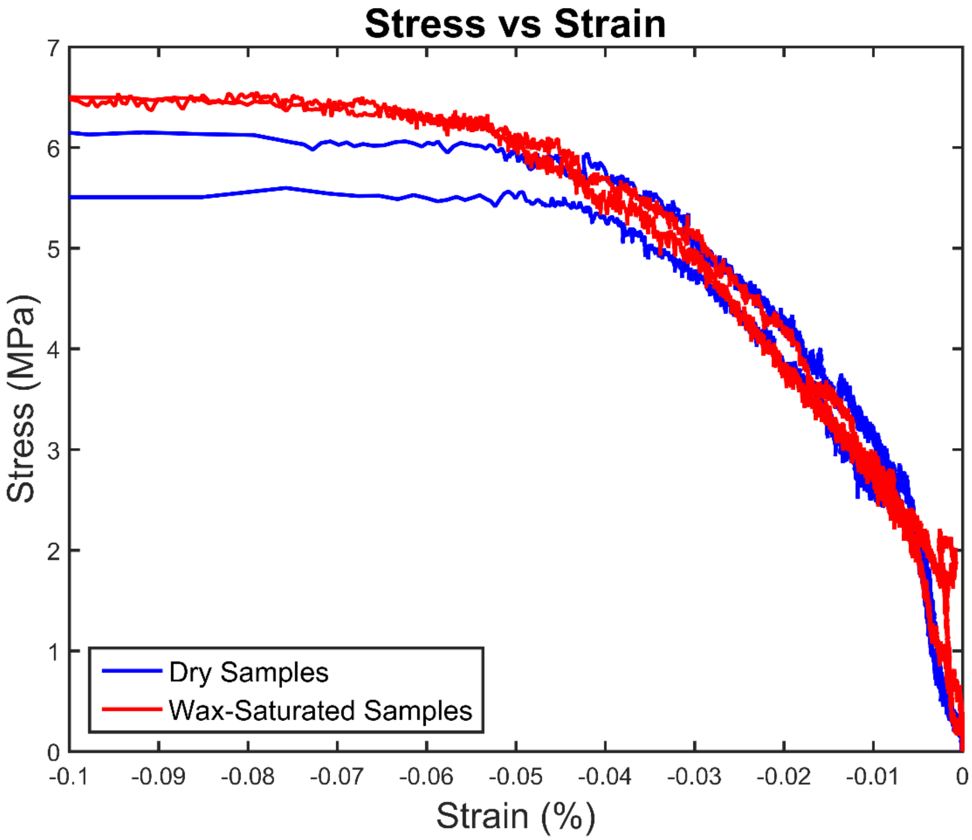

Figure 5.14 Stress-strain curves for 4 Brazilian tensile tests, with strain gauge mounted in center.

Fig. 5.14 shows the resulting negative strain (tension) induced by the applied stress in the Brazilian test. Samples fail suddenly by splitting through their center, resulting in concurrent strain gauge failure as they tear in half. Strain gauge failure is evident in Fig. 5.14 as the strain extends linearly in the negative direction near the peak of the curve. The plotted curves follow a similar path, but the wax-saturated samples withstand larger strain before failing at greater applied stress than their dry counterparts. The curves showing the wax-saturated sample data represent two of the lowest recorded tensile strength values in that group.

5.4 Conclusions

The experimental results from 39 compressive strength tests and 20 indirect tensile strength tests are presented. Approximately half of all samples were saturated with paraffin wax to mimic the practically solid bitumen of the Grosmont formation at in situ conditions. The experimental data show that when comparing dry and wax-saturated compressive test results, the peak compressive strength does not differ across the range of confining pressures applied. The wax saturation does appear, however to affect other attributes of the failure. First, using a simple measure of the samples' Young's moduli, the dry samples unexpectedly appear stiffer. Second, the existence of the wax retards the onset of ductile failure in these samples. Third, the wax also systematically increases the apparent tensile strength of the samples as determined in Brazilian tests. The reasons for this differing behaviour is not yet known, but it possibly results from the fact that 'pore pressures' may be elevated within the wax saturated samples as they are compressively stressed; and these increased pore pressures would in turn reduced the effective stress on the material. However, given that the wax under the strain rates and temperatures of the experiment remains substantially solid it is not clear whether the usual concepts of effective pressure can be so easily applied.

On the microscopic scale of thin section analysis, brittle failure occurs at low differential stress with little obvious deformation observed outside the macroscopic failure site. The failure mode transition to a ductile state involves intense twinning and microfracturing at confining pressures of 15 MPa for dry samples and 20 MPa for wax-saturated samples. When failing by brittle fracture, the wax saturation tends to promote larger scale damage and extensive fracture networks propagating outward at oblique angles from the macroscopic failure plane, especially at elevated (15+ MPa) confining pressures. These fracturing features are not prevalent in dry specimens tested under the same stress conditions and could increase permeability heterogeneity in the wax-saturated samples.

Future work includes analysis of Brazilian tensile tests performed on Grosmont samples, along with integration of available image logging data.

6. Grosmont Formation Brazilian Tensile Strength Results

6.1 Introduction

In addition to the paucity of material, the Grosmont formation core samples, as previously mentioned, did not meet the standard length to diameter ratio recommended for compressional testing. However, the dimensions required for Brazilian tensile strength (BTS) testing are met by cutting the available core into disks. In this short Chapter, the results of Grosmont formation BTS testing are presented. The same testing procedure as the Indiana limestone BTS tests of Chapter 5 was utilized. Although limited core was available for testing, the results shown in this chapter begin to develop a range of tensile splitting strengths for reservoir units of the Grosmont formation. Knowledge of this range contributes to the ultimate goal of building a geomechanical model of the Grosmont formation. The tensile strength of the Grosmont formation may also be of interest because of its relation to drilling induced tensile fractures observed in image logs by Morin [2017].

6.2 Brazilian Tests

A total of four core samples were cut into disks for Brazilian tensile strength testing. The specifications of the core samples are displayed below in Table 5. Three core samples came from the Grosmont C reservoir unit and one from the Grosmont D subunit. Except for sample A1, all core is from well 100-1-27-85-19W4 (UTM Zone 12 Northing 6251511 m, Easting 382333m). The exact depth and well that core sample A1 originates from is unknown, as this information was not provided to us in our early studies, however it is believed to be close (in depth) to the core sample used by Rabbani et al. [2017] at 360.6 m. The length of core sample A1 was 43.5 mm and the diameter of all samples was approximately 37 mm.

Table 5 Grosmont formation core sample specifications

Sample	**Depth from (m)**	**Depth to (m)**	**Porosity (%)**		**Dry bulk density (g/cm^3)**		**# of BTS Disks**	**Grosmont Subunit**	**Grosmont Subunit**
			He Pyc	**MIP**	**Dimensional**	**MIP**			
SA1	~360.6	~360.6	10.9	8.7	2.49	2.54	3	GMC	Sucrosic dolomite
S3	384.46	384.72	15.8	17.3	2.26	2.22	3	GMC	Vuggy dolostone
S6*	374.66	374.85	9.0	7.7	2.64*	2.57	1	GMC	Laminated to massive dolomudstone
S17	347.27	347.46		22.9	2.11	2.13	3	GMD	Laminated to massive dolomudstone

* bitumen-saturated

The sample porosities are estimated from helium pycnometry (He Pyc) and mercury intrusion porosimtery (MIP) (Table 5). The dimensional bulk density of sample 6 was measured in its naturally bitumen saturated state (not dry as the heading suggests).

Three disks were cut from each of core samples A, 3, and 17. Sample 6 had dimensions appropriate for Brazilian testing, so no cutting was required. Prior to BTS testing, bitumen was extracted from core samples, except sample 6, for ultrasonic wave speed experiments. Representative post-testing pictures (Fig. 6.1) and BTS results (Fig. 6.2) for each core sample are shown below.

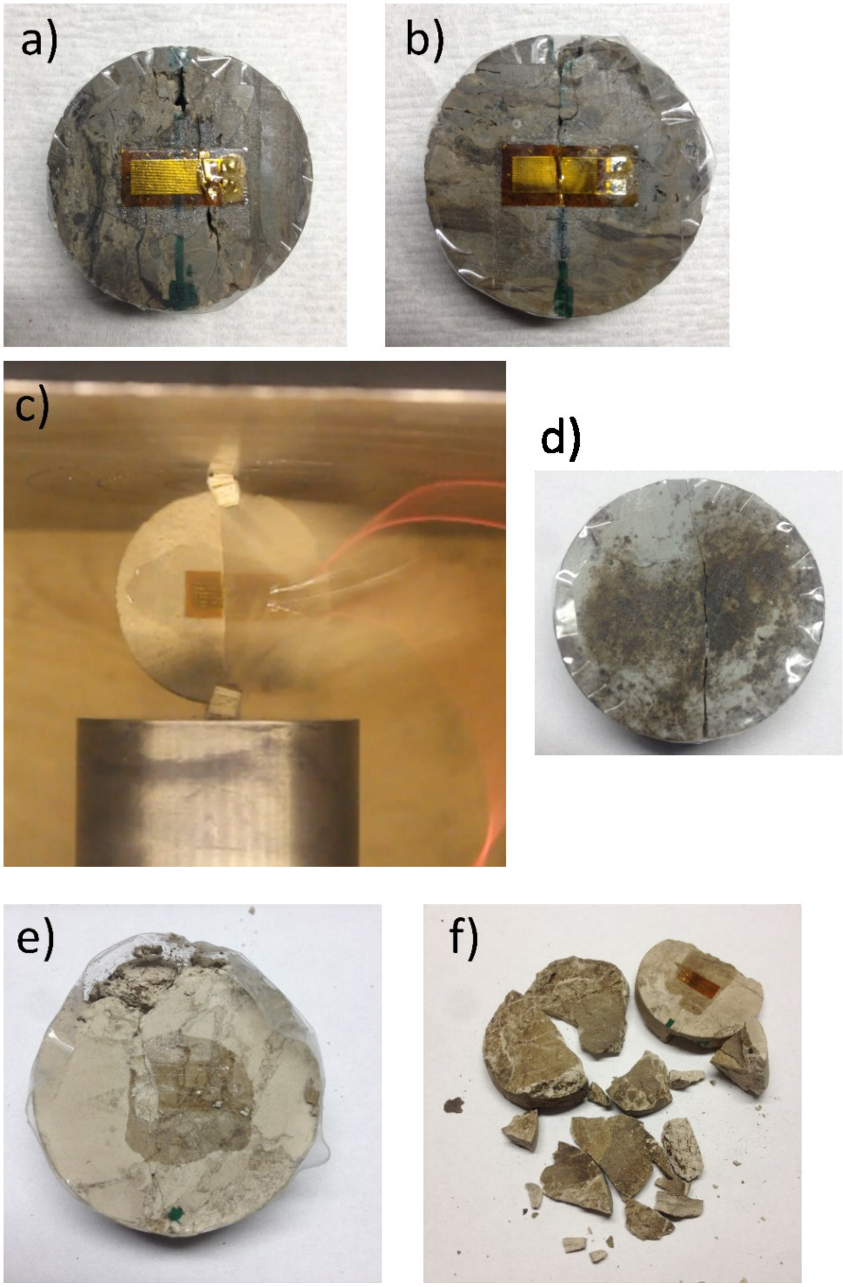

Figure 6.1 Sample photos post-BTS testing. a) A1-1: load applied parallel to laminated features. b) A1-2: load applied perpendicular to laminated features. c) 3b: Frame from recorded video at failure. d) 6a: failure of bitumen saturated sample. e) 17a: failure following plane of weakness. f) 17b: invalid test example as sample crumbles with applied load.

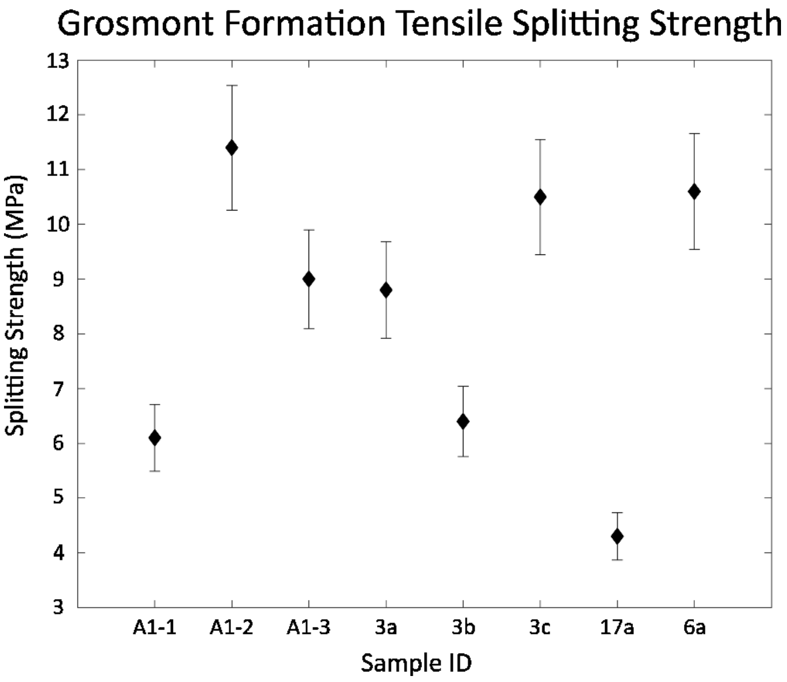

Figure 6.2 Brazilian tensile splitting strength of Grosmont formation samples. Error bars represent 10% error in splitting strength at disk center from stress distribution through wood cushions at contact points (15° arc) [*Perras and Diederichs*, 2014].

The tensile splitting strength from tested Grosmont formation samples range from a low of 4.3 MPa in sample 17a to 11.4 MPa in sample A1-2 (Fig 6.2). The range and scatter of reported splitting strength values is due to testing various facies and sample heterogeneities within those facies. For example, the lowest value of 4.3 MPa was recorded from testing a laminated to massive dolomudstone from the Grosmont D formation, whereas the highest recorded value of 11.4 MPa resulted from testing a sucrosic dolostone from the Grosmont C formation. It is expected that sample constitution and structure will have a considerable influence on tensile strength.

Even disks tested from the same core sample (i.e. samples A1 and 3) show a great deal of scatter in tensile splitting strength (Fig. 6.2). From a visual perspective, core sample 3 appeared the most like Indiana limestone, with no observed bedding features; but it still has a fairly broad range of strength values (6.4-10.5 MPa). A preferred bedding orientation was observed in sample A1, and to test the influence on tensile strength, disk A1-1 and A1-2 were oriented with the applied load parallel and perpendicular to bedding respectively. This is visibly demonstrated in Fig. 6.1 a) and b), where the green line drawn on the disk face indicates diametrical loading. There is a blatant difference in tensile strength with a nearly 2:1 ratio between A1-1 and A1-2. The resulting failure plane of sample A1-1 appears to follow bedding, likely a plane of weakness. The failure plane also deviates from perfectly diametrical, unlike A1-2, calling the test validity into question.

A requirement of the Brazilian tensile strength test is failure initiation from the disk center and failure plane roughly along the diametric loading [*Colback*, 1966]. Unfortunately, two of three disks from sample 17 resulted in invalid failure. Core sample 17 was very weak and difficult to cut into disks without compromising the structural integrity. Upon testing samples 17b and 17c broke into multiple pieces (Fig. 6.1f). The failure plane of 17a appears to follow a bedding feature and breaks from strictly diametrical, but two halves remain, and the test is counted as valid.

Except for sample 6a, the Soxhlet extraction method using toluene, was used to remove bitumen from the samples prior to BTS testing. Conclusions of bitumen's influence on tensile splitting strength cannot be drawn from testing one sample, but it is interesting that 6a has the second highest reported strength. The results from BTS testing in Chapter 5 indicate, that compared with dried samples, wax-saturated Indiana limestone has higher tensile strength values. Further testing is required to determine if a similar trend could be observed within bitumen saturated Grosmont formation samples.

6.3 Conclusions

In summary, from limited core available for BTS testing, the splitting strength values range from 4.3 MPa to 11.4 MPa. Heterogeneities at the core and reservoir scale are responsible for splitting strength scatter within Grosmont formation rocks. For some samples, strength values differ markedly depending on the orientation with respect to the applied diametrical load, suggesting strength anisotropy. Further testing is needed to better characterize the rock strength of the Grosmont formation.

7. Conclusion

7.1 Conclusion

This thesis was motivated by an interest in studying the Grosmont formation's geomechanical properties. The giant quantity of largely unexploited bitumen-in-place residing in the Grosmont formation economically concerns many parties. Geomechanical knowledge is essential to unlock resources from complex reservoirs. The paucity of Grosmont formation core available for this study prevented the completion of a full geomechanical testing program. An analogue was utilized to study the effects of a viscoelastic fluid in the pore space of a carbonate rock. Indiana limestone and a paraffin wax saturant replaced the bitumen filled porosity of Grosmont formation rocks. To our knowledge, no prior geomechanical testing of carbonate rock with viscous pore fluid has been reported.

Chapters 2 and 3 provided background material relevant to the laboratory-based strength tests described in later chapters. Geological aspects of the Grosmont formation were reviewed in Chapter 2, with emphasis on the Grosmont C and D reservoir subunits. The intense fracturing and karstification of the Grosmont formation result in complicated heterogeneities at the core scale, but nearly homogenous, attractive properties (i.e. high porosity/permeability) at the reservoir scale [*Putnam et al.*, 2016]. Indiana limestone was used as a replacement for Grosmont formation rocks in mechanical testing. Of course, as with any geological substitution, this is an imperfect comparison. Indiana limestone has a nearly monomineralic calcite composition, while dolomitization is one of the most important processes responsible for the alluring reservoir quality of the Grosmont formation. The homogenous, isotropic and coherent nature of Indiana limestone starkly contrasts many zones of the vuggy, fractured Grosmont formation. The saturating fluids of the two rocks, paraffin wax and bitumen, are both solid at the subjected temperatures, but impacts of their differing chemical composition on rock strength are unknown. Chapter 2 concluded with a review of techniques used in sample characterization: helium pycnometry, mercury porosimetry, thin-sections, and scanning electron microscope.

Chapter 3 introduced rock mechanics theory fundamental to understanding the applicability of the laboratory experiments. The rock mechanics tests are designed to simulate a rock under stress in the Earth's crust. The crustal stress state determines the faulting regimes observed when stresses exceed rock strength. Rock is more complicated than linear elastic materials but failure at low confining pressures can often be described by Mohr-Coulomb faulting theory. An envelope can be developed to predict failure by performing multiple triaxial strength tests. The brittle-ductile transition may occur at low confining pressures especially within weaker, porous carbonate rocks [*Mogi*, 1966]. Conventional triaxial experiments were used here, but the intermediate principal stress is known to have an impact on both limestone and dolomite [*Mogi*, 1971a].

Chapter 4 detailed the sample preparation process, laboratory testing equipment, and experimental procedures of compressive and tensile rock strength tests. All sample preparations and mechanical tests were completed in house. The unique paraffin wax saturation was achieved simply by combining the sample and wax in a vacuumed oven where wax melted and imbibed the sample. Laboratory testing results of Indiana limestone are found in Chapter 5 and tensile strength tests of Grosmont core samples are found in Chapter 6.

The following was revealed through the comprehensive series of 8 UCS, 31 triaxial, and 20 BTS tests combined with subsequent post-failure microstructural analysis of dry and wax-saturated Indiana limestone samples (Chapter 5):

- There is no statistical difference in ultimate sample strength between dry and wax-saturated samples across the range of applied confining pressures, and as a result, the generated Mohr-Coulomb failure envelopes are nearly identical.
- The estimated Young's modulus values of dry samples are higher at many applied confining pressures. This implies that the dry samples behave stiffer than wax-saturated samples, a somewhat unexpected result. Some scatter is observed in the Young's modulus values and confirmation may require further testing. The average estimated Poisson's ratios are nearly identical.
- Wax saturation delays the transition from brittle to fully ductile behavior as confining pressures are increased. This is concluded from analyzing stress-strain curves and visual inspection of post-failure samples.
- Thin section analysis supports the delayed ductile response in wax-saturated samples. Increased calcite twinning intensity and microfractures are prevalent in dry samples at lower confining pressure than wax-saturated counterparts.
- Under brittle failure conditions, wax-saturation promotes larger scale damage and connected fracture networks emanating from the macroscopic failure plane at oblique angles. The permeability heterogeneity is therefore also likely increased in these samples.

- Brazilian testing results show the apparent tensile strength of the wax-saturated samples is notably higher (~17%) than the dry samples.

The investigation of the Grosmont formation strength in Chapter 6 is restricted to BTS tests. From the valid tests performed, a GMD laminated dolomudstone had the lowest recorded tensile splitiing strength of 4.3 MPa. The highest tensile strength found was 11.4 MPa from testing of a GMC sucrosic dolostone. Sample heterogeneity, particularly bedding features, considerably affects results and suggests strength anisotropy exists in the Grosmont formation. Definitive conclusions cannot be drawn from the limited dataset and, as such, additional testing is required to confirm observed trends and develop a tensile strength range of Grosmont formation rocks.

The mechanical experiments of this study could be improved, and some recommendations are put forth here. A triaxial cell capable of maintaining constant confining pressures as high strain levels are reached would positively impact testing outcomes. This would allow the analysis of testing results beyond the few percent strain observed here. A servo-controlled machine would further this cause as the full expression of the stress-strain curve including the post-failure region is observable. It would also remove the operator influence on stress application present with the dual hand pump configuration. The application of pore pressure to the wax saturated triaxial experiments could also yield interesting results.

From a practical execution perspective, a sample extruder would help extract samples from the Hoek cell without causing additional damage. This would be particularly beneficial for triaxial experiments performed at high confining pressures, where ductile deformation promotes sample barrelling at high strains. For Brazilian tensile tests, upgrading the wood cushions to a set of machined steel curved jaws would make experiment performance easier and more consistent. The wood cushions have slight width variations that could impact results, plus the Brazilian disks are very hard to balance on the cushions with strain gauges attached.

7.2 Future Work

This work on mechanical testing of porous rock saturated with viscous material could be expanded upon in many ways. Testing a dolomitic rock and additional experimental inputs related to thermal recovery techniques could also produce results pertinent to exploitation of Grosmont formation resources. These inputs could include the introduction of intermediate stress, higher stresses, elevated temperatures, water as a partial saturating fluid, and use of other viscous saturating fluids. In order to compensate for the lack of compressive testing of Grosmont formation cores, an alternative method such as the Scratch Test as described by Schei et al. [2000] could be utilized.

In this study, thin sections were prepared through the fracture plane of samples with a brittle failure mode. For samples that exhibited fully ductile behavior, with no identifiable failure plane, the thin section was cut through the sample's center. An alternative method to investigate the internal structure of the samples is computed tomography (CT) x-ray scanning. The non-invasive imaging of CT scanning would provide an additional view of the wax influence on sample deformation and porosity distribution.

This study was focused on production of experimental results and basic interpretation principles. The failure processes observed in these tests could benefit from further theoretical analysis. Modern numerical modelling approaches could also be utilized to better understand these results. If ultrasonic wave speed experiments and CT scanning were performed in conjunction with the rock strength experiments, empirical relationships existing between rock strength, porosity, pressure, and velocity may be recognized and used in a predictive manner.

Further testing is necessary to move toward the ultimate goal of characterizing the Grosmont formation strength and building a complete geomechanical model. This would require additional core, perhaps exclusively for mechanical testing. Performing experiments at controlled temperatures resembling in situ temperatures would provide realistic testing conditions by keeping bitumen immobile and contained within the pore space. The integration of these measurements with well logging data and techniques such as mini frac or leak-off testing would better constrain the stress state and geomechanical characteristics of the Grosmont formation.

References

Adey, R. A., and R. Pusch (1999), Scale dependency in rock strength, *Eng. Geol.*, *53*(3–4), 251–258, doi:10.1016/S0013-7952(99)00041-1.

Alberta Energy Regulator (2015), ST98-2015: Alberta’s Energy Reserves 2014 and Supply/Demand Outlook 2015-2024, , 299.

Amadei, B., V. Janoo, M. Robison, and R. Kuberan (1984), Strength of Indiana limestone in true biaxial loading conditions, *25th US Symp. Rock Mech.*, 338–348.

Anderson, E. M. (1951), *The dynamics of faulting and dyke formation with applications to Britain*, Hafner Pub. Co.

Ardakani, E. P., and D. R. Schmitt (2016), Geothermal energy potential of sedimentary formations in the Athabasca region, northeast Alberta, Canada, *Interpretation*, *4*(4), SR19-SR33.

Ardakani, E. P., and D. R. Schmitt (2017), Geophysical evidence for an igneous dyke swarm, Buffalo Creek, Northeast Alberta, *GSA Bull.*, 47.

Ardakani, E. P., D. R. Schmitt, and T. D. Bown (2014), Case History - Detailed topography of the Devonian Grosmont Formation surface from legacy high-resolution seismic profiles, northeast Alberta, *Geophysics*, *79*(4), B135–B149, doi:doi:10.1190/geo2013-0268.1.

ASTM D3967-08 (2008), Standard Test Method for Splitting Tensile Strength of Intact Rock Core Specimens 1, *ASTM Int. West Conshohocken, PA,*, 20–23, doi:10.1520/D3967-08.2.

ASTM D4543 (2008), Standard Practices for Preparing Rock Core as Cylindrical Test Specimens and verifying Conformance to Dimensional and Shape Tolerances, *Astm*, (D4543-8), 1–9, doi:10.1520/D4543-08.

ASTM D7012-14e1 (2014), Standard Test Methods for Compressive Strength and Elastic Moduli of Intact Rock Core Specimens under Varying States of Stress and Temperatures, , doi:https://doi.org/10.1520/D7012-14E01.

Ausich, W. I., T. W. Kammer, and D. L. Meyer (1997), Middle Mississippian disparid crinoids from the Midcontinental United States, *J. Paleontol.*, *71*(1), 131–148.

Aydin, A., and A. Basu (2006), The use of Brazilian test as a quantitative measure of rock weathering, *Rock Mech. Rock Eng.*, *39*(1), 77–85.

Babcock, E. A. (1978), Measurement of subsurface fractures from dipmeter logs, *Am. Assoc. Pet. Geol. Bull.*, *62*(7), 1111–1126.

Barrett, K. R. (2016), Reservoir geology of the Grosmont Formation Bitumen Steam Pilot, Saleski, Alberta, *Bull. Can. Pet. Geol.*, *64*(2), 147–165, doi:10.2113/gscpgbull.64.2.147.

Barrett, K. R., J. Hopkins, K. N. Wilde, and M. E. Connelly (2008), The origin of matrix and fracture mega-porosity in a carbonate bitumen reservoir, Grosmont Formation, Saleski, Alberta, in *World Heavy Oil Congress, Edmonton*, pp. 10–12.

Bell, J. S., and D. I. Gough (1979), Northeast-southwest compressive stress in Alberta evidence from oil wells, *Earth Planet. Sci. Lett.*, *45*(2), 475–482, doi:10.1016/0012-821X(79)90146-8.

Belyea, H. R. (1952), Notes on the Devonian system of the north-central plains of Alberta,

Benz, T., and R. Schwab (2008), A quantitative comparison of six rock failure criteria, *Int. J. Rock Mech. Min. Sci.*, *45*(7), 1176–1186, doi:10.1016/j.ijrmms.2008.01.007.

Berodier, E., J. Bizzozero, and A. C. A. Muller (2016), Mercury intrusion porosimetry, in *A Practical Guide to Microstructural Analysis of Cementitious Materials*, p. 419, CRC Press.

Bown, T. D. (2011), Legacy Seismic Investigations of Karst Surfaces: Implications for Heavy Oil Extraction From the Devonian Grosmont Formation, Northeastern Alberta, Canada.

Brace, W. F., and Rj. Martin (1968), A test of the law of effective stress for crystalline rocks of low porosity, in *International Journal of Rock Mechanics and Mining Sciences & Geomechanics Abstracts*, vol. 5, pp. 415–426, Elsevier.

Brace, W. F., and D. K. Riley (1972), Static uniaxial deformation of 15 rocks to 30 kb, *Int. J. Rock Mech. Min. Sci.*, *9*(2), 271–288, doi:10.1016/0148-9062(72)90028-9.

Brune, J. N., and M. a. Ellis (1997), Structural features in a brittle–ductile wax model of continental extension, *Nature*, *387*(6628), 67–70, doi:10.1038/387067a0.

Burkhard, M. (1993), Calcite twins, their geometry, appearance and significance as stress-strain markers and indicators of tectonic regime: a review, *J. Struct. Geol.*, *15*(3–5), 351–368, doi:10.1016/0191-8141(93)90132-T.

Buschkuehle, B. E., F. J. Hein, and M. Grobe (2007), An Overview of the Geology of the Upper Devonian Grosmont Carbonate Bitumen Deposit, Northern Alberta, Canada, *Nat. Resour. Res.*, *16*(1), 3–15, doi:10.1007/s11053-007-9032-y.

Butler, R. M. (1994), Steam-Assisted Gravity Drainage: Concept, Development, Performance And Future, *J. Can. Pet. Technol.*, *33*(2), 44–50, doi:10.2118/94-02-05.

Byerlee, J. D. (1968), Brittle-ductile transition in rocks, *J. Geophys. Res.*, *73*(14), 4741–4750, doi:10.1029/JB073i014p04741.

Cargill, J. S., and A. Shakoor (1990), Evaluation of empirical methods for measuring the uniaxial compressive strength of rock, *Int. J. Rock Mech. Min. Sci. Geomech. Abstr.*, *27*(6), 495–503, doi:10.1016/0148-9062(90)91001-N.

Chalaturnyk, R. J., and P. Li (2004), When Is It Important to Consider Geomechanics in SAGD Operations?, *J. Can. Pet. Technol.*, *43*(4), 53–61, doi:10.2118/04-08-discussion.

Cleven, N. R. (2008), The Role of Dolomite Content on the Mechanical Strength and Failure Mechanisms in Dolomite-Limestone Composites.

Colback, P. S. B. (1966), An analysis of brittle fracture initiation and propagation in the Brazilian test, in *1st ISRM Congress*, International Society for Rock Mechanics.

Collins, P. M. (2005), Geomechanical effects on the SAGD process, in *SPE International Thermal Operations and Heavy Oil Symposium*, Society of Petroleum Engineers.

Colmenares, L. ., and M. . Zoback (2002), A statistical evaluation of intact rock failure criteria constrained by polyaxial test data for five different rocks, *Int. J. Rock Mech. Min. Sci.*, *39*, 695–729, doi:10.1016/S1365-1609(02)00048-5.

Cox, J. W. (1970), The high resolution dipmeter reveals dip-related borehole and formation characteristics, in *SPWLA 11th Annual Logging Symposium*, Society of Petrophysicists and Well-Log Analysts.

Cutler, W. G. (1983), Frasnian Stage carbonates of the western Canadian sedi- mentary basin constitute one of the best-documented car- bonate provinces in the world . Extensive subsurface exploration for oil-bearing reefs in the Interior Plains of Alberta , coupled with numero, , *31*(4), 282–325.

Dembicki, E. A., and H. G. Machel (1996), Recognition and Delineation of Paleokarst Zones by the Use of Wireline Logs in the Bitumen-Saturated Upper Devonian Grosmont Formation of Northeastern Alberta, Canada, *Am. Assoc. Pet. Geol. Bull.*, *80*(5), 695–712, doi:10.1306/64ED8886-1724-11D7-8645000102C1865D.

Dunham, R. J. (1962), Classification of Carbonate Rocks According To Depositional Texture, *Classif. Carbonate Rocks - A Symp.*, 108–121, doi:10.1306/M1357.

Ewy, R. T., and N. G. W. Cook (1990a), Deformation and fracture around cylindrical openings in rock--I. Observations and analysis of deformations, *Int. J. Rock Mech. Min. Sci. Geomech. Abstr.*, *27*(5), 387–407, doi:10.1016/0148-9062(90)92713-o.

Ewy, R. T., and N. G. W. Cook (1990b), Deformation and fracture around cylindrical openings in rock-II. Initiation, growth and interaction of fractures, *Int. J. Rock Mech. Min. Sci.*, *27*(5), 409–427, doi:10.1016/0148-9062(90)92714-P.

Fairhurst, C. (1964), On the validity of the “Brazilian” test for brittle materials, *Int. J. Rock Mech. Min. Sci. Geomech. Abstr.*, *1*(4), 535–546, doi:10.1016/0148-9062(64)90060-9.

Fjaer, E., R. M. Holt, A. M. Raaen, R. Risnes, and P. Horsrud (2008), *Petroleum related rock mechanics*, Elsevier.

Friedman, M. (1975), Fracture in rock, *Rev. Geophys.*, *13*(3), 352–358, doi:10.1029/RG013i003p00352.

Friedman, M., and H. C. Heard (1974), Principal stress ratios in cretaceous limestones from Texas Gulf Coast, *Am. Assoc. Pet. Geol. Bull.*, *58*(1), 71–78.

Friedman, M., J. Handin, J. M. Logan, K. D. Min, and D. W. Stearns (1976), Experimental folding of rocks under confining pressure: Part III. Faulted drape folds in multilithologic layered specimens, *GSA Bull.*, *87*(7), 1049–1066.

Gough, D. I., and J. S. Bell (1981), Stress orientations from oil-well fractures in Alberta and Texas, *Can. J. Earth Sci.*, *18*(3), 638–645, doi:10.1139/e81-056.

Groshong Jr., R. H. (1974), Experimental Test of Least-Squares Strain Gage Calculation Using Twinnen

Calcite, *Geol. Soc. Am. Bull.*, *85*(December), 1855–1864.

Haimson, B., and C. Chang (2000), A new true triaxial cell for testing mechanical properties of rock, and its use to determine rock strength and deformability of Westerly granite, *Int. J. Rock Mech. Min. Sci.*, *37*(1–2), 285–296, doi:10.1016/S1365-1609(99)00106-9.

Haimson, B. C., and C. Herrick (1986), Borehole Breakouts-a New Tool For Estimating In Situ Stress?, *ISRM Int. Symp.*, 10.

Han, D., J. Liu, and M. Baztle (2008), Seismic properties of heavy oils—measured data, *Lead. Edge*, *27*(9), 1108–1115, doi:10.1190/1.2978972.

Handin, J., H. C. Heard, and J. N. Magouirk (1967), Effects of the intermediate principal stress on the failure of limestone, dolomite, and glass at different temperatures and strain rates, *J. Geophys. Res.*, *72*(2), 611–640, doi:10.1029/JZ072i002p00611.

Harrison, R. S. (1982), Geology and production history of the Grosmont carbonate pilot project, Alberta, Canada, in *The future of heavy crude and tar sands: Second International Conference on Heavy Crude and Tar Sands*, vol. 1, pp. 199–204.

Heard, H. C. (1960), Chapter 7: Transition from Brittle Fracture to Ductile Flow in Solenhofen Limestone as a Function of Temperature, Confining Pressure, and Interstitial Fluid Pressure, *Geol. Soc. Am. Mem.*, *79*, 193–226, doi:10.1130/MEM79-p193.

Heard, H. C., A. E. Abey, and B. P. Bonner (1974), *High pressure mechanical properties of Indiana limestone*, United States.

Hein, F., and B. Fairgrieve (2013), *Joslyn Creek Steam-assisted Gravity Drainage: Considerations Related to a Surface Steam Release Incident, Athabasca Oil Sands Area, Northeastern Alberta, Canada*.

Herbert, E. G., G. M. Pharr, W. C. Oliver, B. N. Lucas, and J. L. Hay (2001), On the measurements of stress-strain curves by spherical indentation., *Thin Solid Films*, *398–399*, 331–335.

Hoagland, R. G., G. T. Hahn, and a. R. Rosenfield (1973), Influence of microstructure on fracture propagation in rock, *Rock Mech.*, *5*(2), 77–106, doi:10.1007/BF01240160.

Hoek, E., and E. . Brown (1997), Practical estimates of rock mass strength, *Int. J. Rock Mech. Min. Sci.*, *34*(8), 1165–1186, doi:10.1016/S1365-1609(97)80069-X.

Hoek, E., and E. T. Brown (1980), Empirical strength criterion for rock masses, *J. Geotech. Geoenvironmental Eng.*, *106*(ASCE 15715).

Hondros, G. (1959), The evaluation of Poisson's ratio and the modulus of materials of a low tensile resistance by the Brazilian (indirect tensile) test with particular reference to concrete, *Aust. J. Appl. Sci.*, *10*(3), 243–268.

Hopkins, J., K. Wilde, S. Christiensen, and K. Barrett (2010), Regional stratigraphy and reservoir units of the Grosmont Formation: Laricina's Saleski and Burnt Lakes leases, in *GeoCanada 2010 Core Conference*, pp. 57–62.

Hudson, J. A., S. L. Crouch, and C. Fairhurst (1972), Soft, stiff and servo-controlled testing machines: a review with reference to rock failure, *Eng. Geol.*, *6*(3), 155–189, doi:10.1016/0013-7952(72)90001-4.

Hugman, R. H. H. et al. (1979), Effects of Texture and Composition on Mechanical Behavior of Experimentaily Deformed Carbonate Rocks, , *9*(9), 1478–1489.

ILI (2007), *Indiana Limestone Handbook*, 22nd Editi., Indiana Limestone Institute of America, Bedford, IN.

Ingraffea, A. R. (1981), Mixed-mode fracture initiation in Indiana limestone and Westerly granite, in *The 22nd US Symposium on Rock Mechanics (USRMS)*, American Rock Mechanics Association.

Jaeger, J. C., N. G. W. Cook, and R. Zimmerman (2007), *Fundamentals of rock mechanics*, John Wiley & Sons.

Jamison, W. R., and J. H. Spang (1976), Use of calcite twin lamellae to infer differential stress, *Bull. Geol. Soc. Am.*, *87*(6), 868–872, doi:10.1130/0016-7606(1976)87<868:UOCTLT>2.0.CO;2.

Jansen, K. M. B. (1997), Effect of pressure on electrical resistance strain gages, *Exp. Mech.*, *37*(3), 245–249, doi:10.1007/BF02317414.

Jeffreys, H., and S. F. Singer (1959), The Earth: its origin, history and physical constitution, *Phys. Today*, *12*, 61.

Ji, Y., P. Baud, V. Vajdova, and T. -f. Wong (2012), Characterization of Pore Geometry of Indiana Limestone in Relation to Mechanical Compaction, *Oil Gas Sci. Technol. – Rev. d'IFP Energies Nouv.*, *67*(5), 753–775, doi:10.2516/ogst/2012051.

Kaufmann, J., R. Loser, and A. Leemann (2009), Analysis of cement-bonded materials by multi-cycle mercury intrusion and nitrogen sorption, *J. Colloid Interface Sci.*, *336*(2), 730–737, doi:10.1016/j.jcis.2009.05.029.

Kemball, C. (1946), On the surface tension of mercury, *Trans. Faraday Soc.*, *42*, 526–537.

Klein, C., and B. Dutrow (2008), *The 23rd Edition of the Manual of Mineral Science: (after James D. Dana)*, The 23rd Edition of the Manual of Mineral Science:, J. Wiley.

Kushnir, A. R. L., L. A. Kennedy, S. Misra, P. Benson, and J. C. White (2015), The mechanical and microstructural behaviour of calcite-dolomite composites: An experimental investigation, *J. Struct. Geol.*, *70*, 200–216, doi:10.1016/j.jsg.2014.12.006.

Li, D., and L. N. Y. Wong (2013), The brazilian disc test for rock mechanics applications: Review and new insights, *Rock Mech. Rock Eng.*, *46*(2), 269–287, doi:10.1007/s00603-012-0257-7.

Lisabeth, H. P., and W. Zhu (2015), Effect of temperature and pore fluid on the strength of porous limestone, *J. Geophys. Res. B Solid Earth*, *120*(9), 6191–6208, doi:10.1002/2015JB012152.

Machel, H. G., M. Luz Borrero, E. Dembicki, H. Huebscher, L. Ping, and Y. Zhao (2012a), The Grosmont : a complex dolomitized, fractured and karstified heavy oil reservoir in a Devonian carbonate-evaporite platform, *GeoConvention 2012 Vis.*, *10576*, 1–24.

Machel, H. G., M. L. Borrero, E. Dembicki, H. Huebscher, L. Ping, and Y. Zhao (2012b), The Grosmont: the world's largest unconventional oil reservoir hosted in carbonate rocks, *Geol. Soc. London, Spec. Publ.*, *370*(1), 49–81, doi:10.1144/SP370.11.

MacNeil, A. J. (2015), Petrophysical Characterization of Bitumen-Saturated Karsted Carbonates: Case Study of the Multibillion Barrel Upper Devonian Grosmont Formation, Northern Alberta, Canada, *Petrophysics*, *56*(6), 592–614.

Mancktelow, N. (1988), *The rheology of paraffin wax and its usefulness as an analogue for rocks*.

Meléndez-Martínez, J., and D. R. Schmitt (2016), A comparative study of the anisotropic dynamic and static elastic moduli of unconventional reservoir shales: Implication for geomechanical investigations, *Geophysics*, *81*(3), D245–D261, doi:10.1190/geo2015-0427.1.

Mellor, M., and I. Hawkes (1971), Measurement of tensile strength by diametral compression of discs and annuli, *Eng. Geol.*, *5*(3), 173–225, doi:10.1016/0013-7952(71)90001-9.

Mogi, K. (1966), Pressure Dependence of Rock Strength and Transition from Brittle Fracture to Ductile Flow.,

Mogi, K. (1971a), Effect of the triaxial stress system on the failure of dolomite and limestone, *Tectonophysics*, *11*(2), 111–127, doi:10.1016/0040-1951(71)90059-X.

Mogi, K. (1971b), Fracture and flow of rocks under high triaxial compression, *J. Geophys. Res.*, *76*(5), 1255–1269.

Mohebati, M. H., D. Yang, and J. MacDonald (2014), Thermal recovery of bitumen from the grosmont carbonate formation - Part 1: The Saleski Pilot, *J. Can. Pet. Technol.*, *53*(4), 200–211, doi:10.2118/171561-PA.

Morin, M. L. (2017), Natural and Drilling Induced Fractures in the Grosmont Formation, Alberta: Implications for the State of Stress.

Olsson, W. A., and S. S. Peng (1976), Microcrack nucleation in marble, *Int. J. Rock Mech. Min. Sci. Geomech.*, *13*(2), 53–59, doi:10.1016/0148-9062(76)90704-X.

Ong, O., A. Rabbani, X. Chen, D. Schmitt, J. Nycz, and K. Gray (2016), Rock physics laboratory experiments on bitumen-saturated carbonates from the Grosmont Formation, Alberta, in *SEG Technical Program Expanded Abstracts 2016*, pp. 3464–3467, Society of Exploration Geophysicists.

Paterson, M. . (1978), *Experimental Rock Deformation - The Brittle Field*, Springer-Verlag, Berlin and New York.

Paterson, M. S. (1958), Experimental deformation and faulting in wombeyan marble, *Bull. Geol. Soc. Am.*, *69*(4), 465–476, doi:10.1130/0016-7606(1958)69[465:EDAFIW]2.0.CO;2.

Peck, L., C. C. Barton, and R. B. Gordon (1985), Microstructure and the resistance of rock to tensile fracture, *J. Geophys. Res. Solid Earth*, *90*(B13), 11533–11546, doi:10.1029/JB090iB13p11533.

Perras, M. A., and M. S. Diederichs (2014), A Review of the Tensile Strength of Rock: Concepts and Testing, *Geotech. Geol. Eng.*, *32*(2), 525–546, doi:10.1007/s10706-014-9732-0.

Ping Luo, H. G. Machel, and J. Shaw (1994), Petrophysical properties of matrix blocks of a heterogeneous dolostone reservoir - the Upper Devonian Grosmont Formation, Alberta, Canada, *Bull. Can. Pet. Geol.*, *42*(4), 465–481.

Putnam, P., J. Russel-Houston, S. Christensen, and C. Seibel (2016), Comparison of McMurray Formation (Lower Cretaceous) and Grosmont Formation (Upper Devonian) bitumen reservoirs with some speculations, from a geological perspective, on the future of Canadian thermal recovery, *Bull. Can. Pet. Geol.*, *64*(2), 324–353, doi:10.2113/gscpgbull.64.2.324.

Rabbani, A., D. R. Schmitt, J. Nycz, and K. Gray (2017), Pressure and temperature dependence of acoustic wave speeds in bitumen-saturated carbonates: Implications for seismic monitoring of the Grosmont Formation, *Geophysics*, *82*(5), MR133-MR151, doi:10.1190/geo2016-0667.1.

Rigby, S. P., and K. J. Edler (2002), The Influence of Mercury Contact Angle, Surface Tension, and Retraction Mechanism on the Interpretation of Mercury Porosimetry Data, *J. Colloid Interface Sci.*, *250*(1), 175–190, doi:10.1006/jcis.2002.8286.

Rinehart, A. J., J. E. Bishop, and T. Dewers (2015), Journal of Geophysical Research : Solid Earth, , 1–17, doi:10.1002/2014JB011624.Received.

Ritter, H. L., and L. C. Drake (1945), Pressure porosimeter and determination of complete macropore-size distributions. Pressure porosimeter and determination of complete macropore-size distributions, *Ind. Eng. Chem. Anal. Ed.*, *17*(12), 782–786.

Robinson, L. H. J. (1959), Effects of Pore and Confining Pressures on Failure Characteristics of Sedimentary Rocks, *Pet. Trans. AIME*, *216*, 26–32, doi:10.2118/1096-G.

Rossetti, F., G. Ranalli, and C. Faccenna (1999), Rheological properties of paraffin as an analogue material for viscous crustal deformation, *J. Struct. Geol.*, *21*(4), 413–417, doi:10.1016/S0191-8141(99)00040-1.

Russel-Houston, J., and K. Gray (2014), Paleokarst in the Grosmont Formation and reservoir implications, Saleski, Alberta, Canada, *Interpretation*, *2*(3), 29–50, doi:10.1190/INT-2013-0187.1.

Schei, G., E. Fjaer, E. Detournay, C. J. Kenter, G. F. Fuh, and F. Zausa (2000), The Scratch Test: An Attractive Technique for Determining Strength and Elastic Properties of Sedimentary Rocks, *SPE Annu. Tech. Conf. Exhib.*, (SPE 63255), 1–7, doi:10.2118/63255-MS.

Schmidt, R. a. (1976), Fracture-toughness testing of limestone, *Exp. Mech.*, *16*(5), 161–167, doi:10.1007/BF02327993.

Schmidt, R. a., and C. W. Huddle (1977), Effect of confining pressure on fracture toughness of Indiana limestone, *Int. J. Rock Mech. Min. Sci.*, *14*(5–6), 289–293, doi:10.1016/0148-9062(77)90740-9.

Schmitt, D. R., C. a. Currie, and L. Zhang (2012), Crustal stress determination from boreholes and rock cores: Fundamental principles, *Tectonophysics*, *580*, 1–26, doi:10.1016/j.tecto.2012.08.029.

Schultz, R. A. (2016), Causes and mitigation strategies of surface hydrocarbon leaks at heavy-oil fields: examples from Alberta and California, *Pet. Geosci.*, *23*(2), 231–237.

Schwartz, A. E. (1964), Failure Of Rock In The Triaxial Shear Test, in *The 6th US Symposium on Rock Mechanics (USRMS)*, pp. 109–151, American Rock Mechanics Association.

Selucky, M. L., Y. Chu, and O. P. Strausz (1977), Chemical bitumen of Athabasca, , *56*, 369–381.

Smith, N. M. (1966), Sedimentology of the Salem Limestone in Indiana, *Ohio J. Sci.*, *66*(2), 168–179.

Terzaghi, K. von (1936), The shearing resistance of saturated soils and the angle between the planes of shear, in *Proceedings of the 1st international conference on soil mechanics and foundation engineering*, vol. 1, pp. 54–56, Harvard University Press Cambridge, MA.

Theriault, F. (1988), Lithofacies, diagenesis and related reservoir properties of the Upper Devonian Grosmont Formation, northern Alberta (Canada)., *Bull. Can. Pet. Geol.*, *36*(1), 52–69.

Topping, A. D. (1955), The Use of Experimental Constants In the Application of Theories of Strength to Rock, in *Proceedings of the... Midwestern Conference on Solid Mechanics*, vol. 2, p. 178, University of Texas.

Turner, F. J., D. T. Griggs, and H. Heard (1954), Experimental deformation of calcite crystals, *GSA Bull.*, *65*(9), 883–934.

Vajdova, V., P. Baud, and T. F. Wong (2004), Compaction, dilatancy, and failure in porous carbonate rocks, *J. Geophys. Res. Solid Earth*, *109*(5), 1–16, doi:10.1029/2003JB002508.

Vajdova, V., P. Baud, L. Wu, and T. fong Wong (2012), Micromechanics of inelastic compaction in two allochemical limestones, *J. Struct. Geol.*, *43*, 100–117, doi:10.1016/j.jsg.2012.07.006.

Vutukuri, V. S. (1974), The effect of liquids on the tensile strength of limestone, *Int. J. Rock Mech. Min. Sci.*, *11*(1), 27–29, doi:10.1016/0148-9062(74)92202-5.

Walton, G., J. Arzúa, L. R. Alejano, and M. S. Diederichs (2015), A Laboratory-Testing-Based Study on the Strength, Deformability, and Dilatancy of Carbonate Rocks at Low Confinement, *Rock Mech. Rock Eng.*, *48*(3), 941–958, doi:10.1007/s00603-014-0631-8.

Washburn, E. W. (1921), The dynamics of capillary flow, *Phys. Rev.*, *17*(3), 273–283, doi:10.1103/PhysRev.17.273.

Yang, D., M. Hosseininejad Mohebati, and J. MacDonald (2014), Thermal Recovery of Bitumen From the Grosmont Carbonate Formation—Part 2: Pilot Interpretation and Development Strategy, *J. Can. Pet. Technol.*, *53*(4), 212–223, doi:10.2118/171561-PA.

Yuan, Y., B. Xu, B. Yang, and G. Bitcan (2011), Geomechanics for the Thermal Stimulation of Heavy Oil Reservoirs – Canadian Experience, *Soc. Pet. Eng.*, doi:10.2118/150293-MS.

Zhang, L., P. Cao, and K. C. Radha (2010), Evaluation of rock strength criteria for wellbore stability analysis, *Int. J. Rock Mech. Min. Sci.*, *47*(8), 1304–1316, doi:10.1016/j.ijrmms.2010.09.001.

Zheng, Z., N. Cook, and L. Myer (1989), Stress induced microcrack geometry at failure in unconfined and confined axial compressive tests, *30th US Symp. Rock …*, 749–756.

Zoback, M. D. (2007), *Reservoir geomechanics*, Cambridge University Press.

Appendix A

Sample specifications

Sample	Mass (g)	Length (mm)	Diameter (mm)	L:D ratio	Porosity	Saturation
S49	155.80	69.52	35.64	1.95	-	dry
S52	159.20	70.77	35.53	1.99	-	dry
S53	157.20	70.05	35.55	1.97	-	dry
S59	156.40	70.02	35.57	1.97	-	dry
S7	197.54	77.16	37.88	2.04	-	dry
S16	185.96	73.95	37.45	1.97	-	dry
S8	182.73	73.30	37.38	1.96	-	dry
S60	156.10	70.57	35.36	2.00	-	dry
S54	158.90	70.67	35.57	1.99	-	dry
S10	189.14	75.71	37.45	2.02	-	dry
S25	193.88	75.48	37.82	2.00	-	dry
S11	194.30	77.00	37.48	2.05	-	dry
S13	193.38	76.41	37.62	2.03	-	dry
S22	186.95	74.61	37.44	1.99	-	dry
S56	158.70	70.90	35.55	1.99	-	dry
S14	186.39	74.18	37.47	1.98	-	dry
S17	190.09	75.98	37.44	2.03	-	dry
S23	193.33	75.45	37.86	1.99	-	dry
S12	199.32	78.19	37.73	2.07	-	dry
S15	179.31	71.75	37.41	1.92	-	dry
S24	184.58	73.56	37.44	1.96	14.82	91.7
S37	157.50	70.66	35.33	2.00	15.28	89.2
S39	153.30	68.48	35.52	1.93	15.73	91.6
S40	158.80	70.77	35.58	1.99	15.66	89.7
S18	182.42	73.01	37.42	1.95	15.23	94.5
S36	153.10	69.26	35.32	1.96	15.99	90.1
S20	187.26	74.95	37.36	2.01	15.12	93.2
S35	150.70	68.21	35.28	1.93	15.84	90.4
S21	184.62	74.03	37.43	1.98	15.50	92.0
S34	154.30	69.83	35.31	1.98	15.80	89.5
S26	149.50	67.58	35.31	1.91	15.77	91.6
S19	181.31	72.62	37.44	1.94	15.36	92.9
S33	151.90	68.37	35.33	1.94	15.55	89.5
S27	152.90	69.50	35.33	1.97	16.39	90.5
S28	154.30	69.71	35.32	1.97	15.74	90.9
S32	153.80	69.78	35.32	1.98	16.02	90.2
S29	157.10	70.92	35.36	2.01	15.87	91.4
S30	154.20	69.95	35.31	1.98	16.01	91.1
S31	152.50	68.55	35.34	1.94	15.39	91.3
Average	170.48	72.09	36.39	1.98	15.63	91.1